Università degli Studi di Padova

SCUOLA DI SCIENZE
DIPARTIMENTO DI FISICA E ASTRONOMIA
"GALILEO GALILEI"

LAUREA MAGISTRALE IN ASTRONOMIA

CMB-GALAXY CROSS-CORRELATION AS A COSMOLOGICAL TEST OF MODIFIED GRAVITY

Relatore: Dott. Michele Liguori
Correlatore: Prof. Nicola Bartolo

Laureando:
Giampaolo Benevento

Anno Accademico 2015 - 2016

Ai miei genitori

Contents

Chapter 1

Introduction

Cosmological observations carried out in the last two decades imply the existence of an unknown energetic component that heavily influences the current dynamics of the Universe, the so called Dark Energy.
Analysis of Cosmic Microwave Background (CMB) anisotropies, recently measured by the Planck satellite [68], and of the Hubble diagram of type Ia Supernova [24], indicate that the Universe is almost spatially flat and that the rate of its expansion actually grows with time. On the other hand the data from the Large Scale Structure surveys, that map the distribution of galaxies in different redshift and different angular scales, confirm this picture.
The ΛCDM model, developed in the theoretical framework of General Relativity, and based on the Cosmological Principle, postulates the existence of a cosmological constant Λ, which is expected to drive the measured cosmic acceleration and constitute almost 70% of the energy content of the Universe.
However, other possible explanations are not ruled out from both a theoretical and observational point of view. In this contest scenarios beyond the ΛCDM can be distinguished in: dark energy (DE) models, in which the current dynamics of the Universe is driven by a time-evolving scalar-field, and modified gravity models (MG), which suppose some modification of General Relativity acting on large scale.
We present in this thesis a method able to discriminate between different scenarios. In a Universe with accelerating expansion, the gravitational potentials associated to large scale structures decay. A photon of the traveling through a decaying potential will experience a net change in energy. This leads to a sencondary anisotropy in the CMB temperature distribution. Such particular gravitational redshift effect is called Integrated Sachs Wolfe (ISW), as it has to be integrated along the line of site and due to its similarity with the (pre-recombination) Sachs-Woolfe effect which is also generated by gravitational potential and arises on the same large angular scales. The ISW signal is not detectable using only data of CMB temperature, due to the noise arising from other sources of anisotropies on large angular scales and from the cosmic variance.
Cross-correlation between the CMB and a tracer of the gravitational potential, like the projected galaxy number counts, can extract the ISW signal, making it detectable with high significance using the upcoming galaxy surveys. This constitutes a cosmological probe sensitive to the growth rate of matter perturbations at the linear level, which depends on the adopted model of dark energy or modified gravity.

In this thesis we consider a particular class of modified gravity models, called K-mouflage, which predict a considerable deviation from ΛCDM in the growth rate of cosmic structures, even at high redshift. Such kind of models are therefore suitable to be tested through cross-correlation between CMB and galaxies. We thus perform a cross-correlation analysis of three different K-mouflage models, with the aim of forecasting their detectability using two upcoming cosmological survey: Euclid and LSST.
In Chapter 2 we provide a general introduction about the standard cosmological model and about the observational evidences for some form of dark energy. We discuss the hypothesis of a cosmological constant and then we briefly review possible alternative explanations to the current accelerated expansion of the Universe.
In Chapter 3 we develop the theory about the ISW effect. We start by deriving the growth of matter perturbations at the linear perturbative order, then we describe the CMB anisotropies and the statistical approach to their study. In the second part of the Chapter we describe in detail the ISW effect and we outline the theory about CMB-galaxy cross-correlation.
In Chapter 4 we outline the theoretical background about the K-mouflage theory, also showing how this mechanism reproduces the General Relativity on small scales.
In Chapter 5 we show our numerical solution of the dynamics equations for three different models of K-mouflage and we compute the growth factor of matter perturbation (and other important quantities) for these scenarios.
In Chapter 6 we compute the cross-correlation power spectra for the cosmological models that we analysed, in several redshift bins, simulating the results of the upcoming Euclid and LSST surveys. In the final part we forecast the level of significance at which each K-mouflage model would be distinguished from ΛCDM.
Chapter 7 is dedicated to our conclusions.

Chapter 2

Standard cosmological model

The Λ-Cold Dark Matter (ΛCDM) standard model of cosmology is one of the most successful theory in physics, as it accounts for a host of cosmological observations. Assuming General Relativity as the theory to describe gravity on all scales and basing on the Cosmological Principle, it outlines a Universe evolving from an initial state of infinite density and temperature, the so called "Big Bang". The fundamental discoveries of Hubble expansion and of the cosmic microwave microwave background confirmed this picture and provided powerful instruments to investigate the composition of the Universe.
In 1998, astronomers made another astonishing discovery, namely that the expansion of the Universe is accelerating, not slowing down .
The ΛCDM model can account for all the present cosmological observations by invoking the existence of two unknown components: the *dark matter* and the *dark energy*. According with the Planck mission results, the ΛCDM model predict the present energy content of the Universe to be:
Baryonic Matter: $\sim 4.9\%$ Ordinary matter, mainly composed by light elements (hydrogen, helium, lithium) that are supposed to form during a primordial phase, the so called "Big Bang Nucleosynthesis". The observed abundances of these nuclei is in completely agreement with the prediction of statistical mechanics.
Dark Matter: $\sim 27\%$ It consists in non-interacting massive particles of non-baryonic nature with a dust like equation of state. Its existence has been postulated to explain the formation of large scale structure. Despite we have significant indirect evidences for the existence of dark matter in galaxies and in clusters of galaxies, like the flat rotational curve of galaxies or the gravitational lensing observations, this component has not been detected yet nether in the laboratories nor in space and its nature remains unknown.
Dark Energy: $\sim 68.3\%$ It consists in a form of energy that dynamically acts as a repulsive force on large scales, necessary to explain the accelerating expansion of the Universe. Within the framework of GR, the simplest option is the cosmological constant (Λ), first introduced by Einstein. However, in order to explain the current acceleration of the Universe, the required value of the energy density associated with Λ must be incredibly small. Alternatively, there could be no dark energy if GR itself is in error on cosmological scales.
The standard model of cosmology is based on a huge extrapolation of our limited knowledge of gravity. GR has not been tested independently on galactic and cosmological scales. The discovery of the late time acceleration of the Universe may require us to revise the theory of gravity on cosmological scales and the

standard model of cosmology based on GR.

2.1 Friedmann Lemaitre Robertson Walker model

2.1.1 Cosmological Principle and metric

The Cosmological Principle represents the foundational hypothesis of cosmology. It was first formulated by Einstein and consists in the following assertion: *"On sufficiently large scales the Universe is both homogeneous and isotropic"*. Homogeneity is the property of being identical everywhere in space, while isotropy is the property of looking the same in every direction.
Observations of the Large Scale Structure of the Universe show that the property of homogeneity is valid, if taken in a statistical sense; indeed the Universe can be considered identical (on average) in different places when one looks at sufficiently large patches, larger than about 200 Mpc. The strongest evidence for isotropy is given by observation of the Cosmic Microwave Background Radiation, as we will discuss.
It's interesting to notice that the Cosmological Principle was introduced before any observational evidence; this tells a lot about how much essential it is, in fact it was present in various form in all the cosmological theories born in the last century, from the Big Bang to the Steady State Model.
Its importance for relativistic cosmology lies in the fact that it provides symmetries allowing to simplify a lot the Einstein equations, which are in general complicated non-linear equations. Since a symmetry corresponds to a conservation rule, any three-dimensional spacial slice of the space-time has to be invariant under both translation and rotations to satisfy the Cosmological Principle.
In General Relativity the geometric properties of space-time are described by the metric tensor $g_{\mu\nu}$, that gives the rule to measure physical distances in curved manifolds. The most general metric for a space-time characterized by maximally symmetric spacelike hypersurfaces, is described by the Friedmann-Lemaître-Robertson-Walker (FLRW from now) line element:

$$\mathrm{d}s^2 = -\mathrm{d}t^2 + a^2(t)\left[\frac{\mathrm{d}r^2}{1-Kr^2} + r^2(\mathrm{d}\theta^2 + \sin^2\theta\mathrm{d}\phi^2)\right] \tag{2.1}$$

where we adopt, from now on, the signature (-,+,+,+). The coordinates r, θ and ϕ are known as comoving coordinates.
We can figure the Universe as a fluid in which the fundamental particles are galaxies, and a fluid element has a volume that contains many galaxies, yet is small compared to the whole Universe. A freely moving fluid element is at rest in the comoving coordinates system, we call fundamental observers all observers who are at rest with the local freely moving fluid element.
The function $a(t)$ is called the scale factor, it relates the comoving coordinates to physical distances and it is normalized to unity today. The scale factor varies in time, changing the overall size of the observable Universe while preserving isotropy and homogeneity. Based on the cosmological principle, a fundamental observer sees the same picture of the Universe in every direction, but this picture can change in time according to the evolution of $a(t)$.
The constant K describes the curvature of the space-like hypersurfaces: the case $K = 0$ corresponds to a flat three-dimensional space with no curvature; $K > 0$

corresponds to a positive curvature, or to an closed space; $K < 0$ corresponds to a negative curvature and to a open space. The curvature is related to the energetic content of the Universe, as we are going to show in the next Section. Cosmologists often adopt a rescaling of the coordinates that leads to a form of the metric in which the curvature can assume only the three values $k = 1, 0, -1$, in which however the scale factor differs from unity today, for further details see [Longair].

2.1.2 Evolution Equations

The dynamics of the Universe is fully determined by the temporal evolution of the scale factor. To obtain $a(t)$ we have to write the Einstein equations in the particular case of the FLRW metric.
The Einstein equations describe gravitation as a result of the relation between the energy content and the geometry of space-time, they read as:

$$G^{\mu}_{\nu} = R^{\mu}_{\nu} - \frac{1}{2} R g^{\mu}_{\nu} = 8\pi G T^{\mu}_{\nu}. \tag{2.2}$$

The Ricci tensor R^{μ}_{ν} and the Ricci scalar R describe the geometric properties of the space-time and depends on the metric and its derivatives, whereas T^{μ}_{ν} is the energy momentum tensor describing the energy content of the Universe.
By virtue of the cosmological principle the Universe is assumed to be filled by perfect fluids, for which the energy momentum tensor assumes the following form in any reference system:

$$T^{\mu}_{\nu} = (p + \rho) u^{\mu} u_{\nu} + p g^{\mu}_{\nu}, \tag{2.3}$$

where u_{μ} is the four-velocity of the fluid, ρ and p are the energy density and the pressure density of the fluid, respectively. In the comoving coordinate system, in which the fluid is at rest the four velocity is $u_{\mu} = (1, 0, 0, 0)$, thus T^{μ}_{ν} reads simply:

$$T^{\mu}_{\nu} = Diag(-\rho, p, p, p). \tag{2.4}$$

The Ricci tensor and Ricci scalar can be computed for a FLRW background, giving:

$$R^{0}_{0} = 3\frac{\ddot{a}}{a}, \tag{2.5}$$

$$R^{i}_{j} = \left(3\frac{\ddot{a}}{a} + 2\frac{\dot{a}^2}{a^2} + 2\frac{K}{a^2}\right)\delta^{i}_{j}, \tag{2.6}$$

$$R = 6\left(\frac{\ddot{a}}{a} + \frac{\dot{a}^2}{a^2} + \frac{K}{a^2}\right). \tag{2.7}$$

By substituting the value of g^{μ}_{ν}, R^{μ}_{ν}, R, T^{μ}_{ν}, as written above for an isotropic and homogeneous Universe, in the Einstein equations we obtain:

$$H^2 \equiv \left(\frac{\dot{a}}{a}\right)^2 = \frac{8\pi G}{3}\rho - \frac{K}{a^2}, \tag{2.8}$$

$$\frac{\ddot{a}}{a} = -\frac{4\pi G}{3}(\rho + 3p). \tag{2.9}$$

The Friedmann equations Eq. (2.8)-(2.9) are two differential equations governing the background dynamics of the Universe, they relate the evolution of the scale

factor $a(t)$ with $p(t)$ and $\rho(t)$. The factor $H(t) \equiv \frac{\dot{a}}{a}$, is called the *Hubble rate* and describes the rate of the cosmic expansion.
For a given rate of expansion, there is a critical density that yields a null spatial curvature $K = 0$:

$$\rho_c = \frac{3H^2}{8\pi G} \tag{2.10}$$

The Friedmann equations reveal the fact that there is a direct connection between the density of the Universe and its global geometry. One can rewrite Eq. (2.8) in the form:

$$\Omega - 1 = \frac{K}{(aH)^2} \tag{2.11}$$

where $\Omega \equiv \rho/\rho_c$ is the dimensionless density parameter. From Eq. (2.11) we see that:

$$\begin{aligned} &\Omega > 1 \ or \ \ \rho > \rho_c \rightarrow \ \ K > 0 \\ &\Omega = 1 \ or \ \ \rho = \rho_c \rightarrow \ \ K = 0 \\ &\Omega < 1 \ or \ \ \rho < \rho_c \rightarrow \ \ K < 0. \end{aligned}$$

Observations have shown that Ω_{tot} is very close to 1, implying a spatially flat geometry. This is actually a natural result of an inflationary phase in the early Universe [59].
From the Bianchi identity $\nabla_\mu T^\mu_\nu = 0$, we get the continuity equation, that express the conservation of energy for fluids in FLRW space-time:

$$\dot{\rho} = -3H(\rho + p). \tag{2.12}$$

It is important to note that the continuity equation can also be obtained from the Friedmann equations by eliminating the scale factor. Indeed, the continuity equation together with the Friedmann, form a set of three mutual-dependent equations in the variables: $a(t),\ p(t),\ \rho(t)$.
To obtain the solution it is needed to specify a relation between the density and the pressure, that is an equation of state. In many cases of physical interest, the equation of state is a simple linear law:

$$p = \omega\rho, \tag{2.13}$$

ω is the proportionality constant.
According to the current picture, the Universe is filled by a mixture of different energetic components, each one has is own EoS. The case with $\omega = 0$ represents pressure-less material, called dust. All non relativistic particles, like nuclei and electrons of ordinary matter or the cold, non-baryonic dark matter particles, exert a pressure (of order $K_B T$) which is negligible with respect to their energy (of order mc^2). Therefore the *dust* equation of state is a good assumption for this kind of fluids.
On the other hand, a fluid of non-degenerate and ultrarelativistic particles, like photons or neutrinos exert non-negligible pressure. In thermal equilibrium its equation of state is $\omega = \frac{1}{3}$.
We consider also the case of a fluid with $\omega = -1$, this condition refers to a so called *cosmological constant* Λ. As we will see in the next Sections, a fluid with EoS close to -1 is supposed to dominate the current dynamics of the Universe and to drive the cosmic accelerated expansion, cosmologists call it *Dark Energy*. In the framework of ΛCDM, the dark energy component is identified with an exact

cosmological constant.
For a single perfect fluid with EoS ω the solution to the continuity equation gives:

$$\rho \propto a^{-3(\omega+1)}. \tag{2.14}$$

The total energy density on the right and side of Eq. (2.8), receives contributions from all the components present in the Universe, each component evolving differently with time. The main energetic components consist in: non-relativistic particles, like baryonic matter and dark matter (with density ρ_m); relativistic particles, like photons and neutrinos (with density ρ_{rad}), and dark energy (with density ρ_{DE}).
According to the ΛCDM model the Universe undergoes different phases, during which different dominant components influence the dynamical evolution of the scale factor. Considering a null spatial curvature ($K = 0$), we can synthesize the solution of Eq. (2.8) and Eq. (2.12) during this phases as follows:

$$\textit{Radiation domination} \;:\; a(t) \propto t^{\frac{1}{2}}, \;\; \rho(a) \simeq \rho_{rad}(a) \propto a^{-4} \tag{2.15}$$

$$\textit{Matter domination} \;:\; a(t) \propto t^{\frac{2}{3}}, \;\; \rho(a) \simeq \rho_m(a) \propto a^{-3} \tag{2.16}$$

$$\Lambda \textit{ domination} \;:\; a(t) \propto e^{Ht}, \;\; \rho \simeq \rho_\Lambda = const. \tag{2.17}$$

Finally, considering the above results, we can write a useful expression for the Hubble parameter in the case of ΛCDM model:

$$H^2 = H_0^2(\Omega_{rad}^{(0)} a^{-4} + \Omega_m^{(0)} a^{-3} + (1 - \Omega^{(0)}) a^{-2} + \Omega_\Lambda^{(0)}), \tag{2.18}$$
$$\Omega^{(0)} = \Omega_{rad}^{(0)} + \Omega_m^{(0)} + \Omega_\Lambda^{(0)}$$

where the Ω-parameters are the dimensionless density parameters of the various energetic component, defined as $\Omega_i = \rho_i/\rho_c$, the superscript indicates that quantities have to be evaluated at the present epoch.

2.1.3 Hubble expansion and distance measurements

One of the fundamental pieces of evidence supporting the validity of the FRLW model is that light coming from objects in deep space shows a Doppler shift interpretable as relative velocity away from Earth.

In 1929 Hubble conducted observations[1] on nearby galaxies and found the existence of a linear relation between the shift of spectral lines $z = \frac{\Delta\lambda}{\lambda}$ emitted by a source and its distance d on scales of order $\gtrsim 10$ megaparsecs (Mpc):

$$cz \simeq v = H_0 d \tag{2.19}$$

where H_0 is the so called *Hubble constant*, to be identified with the Hubble parameter evaluated at the present epoch.
The term v indicates the recession velocity of a cosmological source, inferred from the redshift z via the relation:

$$z = \frac{\lambda_o}{\lambda_e} - 1 = \sqrt{\frac{1 + v/c}{1 - v/c}} - 1 \simeq \frac{v}{c} \tag{2.20}$$

Here, λ_o and λ_e are the observed and emitted wavelengths respectively. However the last equality is valid only in the limit $v << c$ (small distances). The correct

[1] The law was first deduced by Lemaitre in 1927 on purely theoretical basis

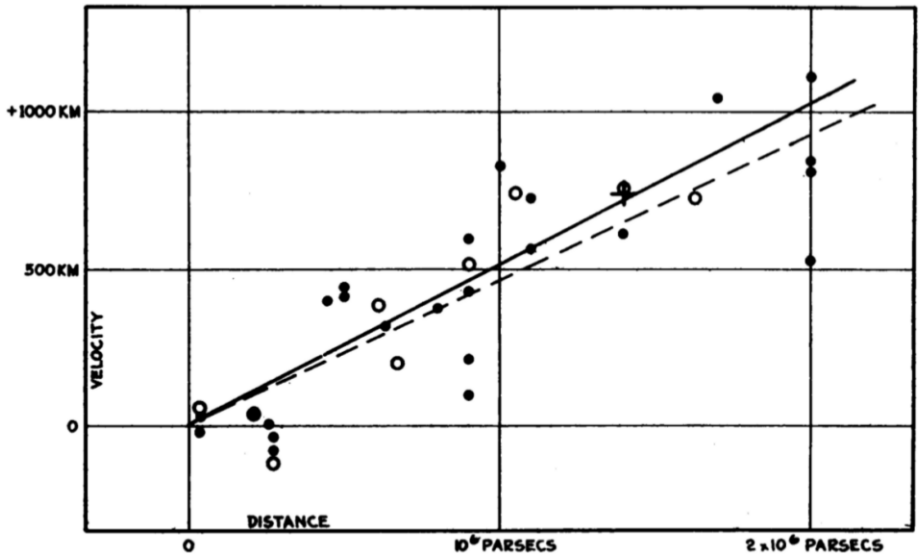

Figure 2.1: **Left**: The original Hubble diagram [51]

interpretation of redshift for sources at large distances is to relate this effect to a relativistic temporal dilation, which acts on the frequencies of photons travelling through an expanding space-time. In particular, it can be shown that the observed frequency of a photon, changes proportionally to the scale factor, thus it is possible to relate the redshift to the scale factor:

$$1 + z = \frac{1}{a}. \tag{2.21}$$

The above equation tell us that redshift is a measure of the scale factor of the Universe at the time radiation was emitted by the source.
The evidence for an expanding Universe confirms the world model depicted by Friedmann, leading physicists to refuse the idea of a static Universe carried out by the Steady State model.
A special attention should be paid to the distance appearing on the right hand side of Eq. (2.19) as in expanding space-time the notion of distance is not univocal and differs from the euclidean case.
From the FRLW line element we can define the proper distance as [Coles Lucchin]:

$$d_p = a(t) \int_0^r \frac{\mathrm{d}r}{\sqrt{1 - Kr^2}} = a(t)\chi. \tag{2.22}$$

where χ is the comoving distance i.e. the distance between two points measured along a path defined at the present cosmological time ($a = 1$). The comoving distance between two astronomical objects whose motion is due solely to cosmic expansion, does not change in time. The proper distance is the sum of physical distances measured by a chain of comoving observers in a straight line between the two objects, at the same time. To relate the comoving (and proper) distance to the redshift of a light source, we use the fact that the observer (at the present time t_0) and emitter (at time t) are connected by a light ray along a radial path ($\mathrm{d}s^2 = -\mathrm{d}t^2 + a^2(t)\frac{\mathrm{d}r^2}{1-Kr^2} = 0$), thus obtaining the following equalities:

$$\chi = \int_0^r \frac{\mathrm{d}r}{\sqrt{1 - Kr^2}} = \int_t^{t_0} \frac{c\mathrm{d}t'}{a(t')} = \int_a^1 \frac{c\mathrm{d}a'}{a'^2 H(a')} = \int_t^{t_0} \frac{c\mathrm{d}t'}{a(t')} = \int_0^z \frac{c\mathrm{d}z'}{H(z')}, \tag{2.23}$$

where we made use of Eq. (2.21) and of the definition of the Hubble parameter. We see that the Hubble law Eq. (2.19) can be obtained in terms of the proper distance, by differentiating Eq. (2.22) with respect to time, for objects at rest in the comoving coordinate system.

The proper distance is of little operational significance because the light emitted by distant objects takes a finite time to travel to us; we cannot therefore make measurements along a surface of constant proper time, but only along our past light cone. One can, however, define operationally other kinds of distance which are, in principle, directly measurable.
For an object of intrinsic luminosity L, the measured energy flux F defines the luminosity distance d_L to the object:

$$d_L \equiv \sqrt{\frac{L}{4\pi F}} \tag{2.24}$$

The luminosity distance generalizes to an expanding Universe the inverse square law valid for a Minkowsky space-time : $F = L/(4\pi d^2)$. In an expanding space-time this observed flux, being proportional to energy transfer per unit time, is reduced by a factor of $(1+z)^2$: one power of $(1+z)$ comes from energy reduction due to wavelength lengthening of the emitted light, and another power due to the increasing time interval, thus in terms of the comoving distance we have:

$$\begin{aligned} &F = \frac{L}{4\pi\chi^2(1+z)^2} \;\Rightarrow \\ &\Rightarrow d_L = (1+z)\chi = (1+z)\int_0^z \frac{cdz'}{H(z')} = \int_0^z \frac{\mathrm{d}z'}{\sqrt{\Omega_m(1+z')^3 + \Omega_{DE}(1+z')^{3(1+\omega)}}}. \end{aligned} \tag{2.25}$$

In the last equality we made use of Eq. (2.21), we have assumed null spatial curvature and we have neglected the contribution of radiation as we are interested in low redshifts, when the dark energy contribution starts to be important. The above equation is crucial for observational cosmology. Different cosmological models having a Hubble parameter with different z dependence would yield a different distance-redshift relation, thus this relation can be used to distinguish between different cosmological scenarios. Practically, one measures the luminosity distance for a class of sources at different redshifts, and then fit the data with a theoretical curve in a redshift-distance diagram, called the *Hubble diagram*.
Eventually we note that, taking the limit of Eq. (2.25) for $z << 1$, we recover the Hubble law $cz = H_0 d_L$.
The functional dependence of distance on the redshift is, of course, the Hubble relation. Different cosmological models having a Hubble constant with different z dependence would yield a different distance-redshift relation. Thus the Hubble curve can be used to distinguish between different cosmological scenarios.
As we shall discuss in the next section, basing on this method, our Universe has been discovered to be in an accelerating expansion phase. In Fig (2.2) right pannel, we can see different theoretical Hubble diagrams, based on Eq. (2.25) in the assumption of a spatially flat Universe with two main component: matter and cosmological constant.
In conclusion, we mention an other distance measure, useful for cosmological

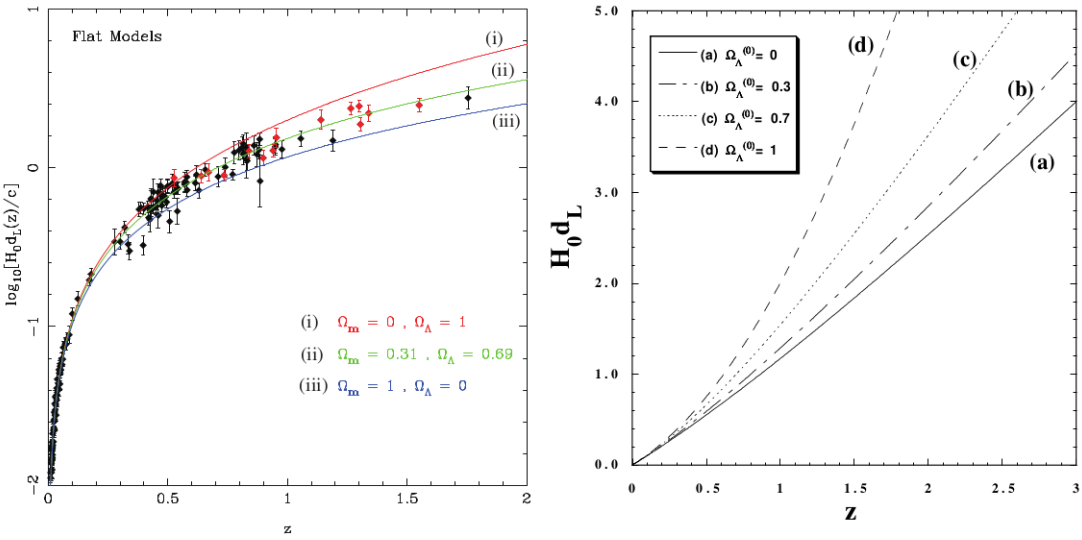

Figure 2.2: **Left** :The luminosity distance $H_0 d_L$ (log plot) versus the redshift z for a flat cosmological model. The black points come from the "Gold" data sets, whereas the red points show the data from HST. Three curves show the theoretical values of $H_0 d_L$ for (i) $Omega_m = 0$, $\Omega_{DE} = 1$, (ii) $Omega_m = 0.31$, Ω_{DE} and (iii) $Omega_m = 1$, $\Omega_{DE} = 0$
Right: Luminosity distance $H_0 d_L$ for a two component flat universe with a non-relativistic fluid ($\omega_m = 0$) and a cosmological constant ($\omega_\Lambda = -1$). We plot $H_0 d_L$ for various values of Ω_Λ [24]

applications: the so called angular diameter distance. The angular diameter distance is defined in terms of the object's proper size l, and the apparent angular θ size of the object as viewed from earth:

$$d_A \equiv \frac{l}{\theta}, \tag{2.26}$$
$$d_A = \frac{d_p}{1+z} = \frac{d_L}{(1+z)^2},$$

where the second line of Eq. (2.26) expresses the link between d_A and the others cosmological distance. The angular diameter distance- redshift relation can be used to test cosmology, analogously to the luminosity distance-redshift relation.

2.2 The accelerated expansion of the Universe

Let us consider the Friedmann equation and impose an accelerated expansion rate:

$$\ddot{a} = -\frac{4}{3}\pi G(\rho + 3p)a > 0 \;\Leftrightarrow\; p < -\frac{1}{3}\rho \;\Leftrightarrow\; \omega \equiv \frac{p}{\rho} < -\frac{1}{3}. \tag{2.27}$$

From the last equation we define "dark energy" a perfect fluid with EoS satisfying the condition: $\omega < -\frac{1}{3}$, which originates a negative pressure term in the Friedmann equation, leading to $\ddot{a} > 0$.
In this section we review the most important observational evidence for Dark Energy and introduce the standard model interpretation in terms of a cosmological constant Λ, characterized by the EoS $\omega = -1$. The cosmological constant so far fits all the data very well and is the simplest solution to the cosmic acceleration puzzle. The Λ CDM model has just one additional parameter that arises naturally in our theory of gravity and matter anyway. In fact, we expect it must be there

because of the vacuum energy. The problem is that an incredible fine-tuning is necessary in order for the energy associated to the cosmological constant to have the observed size.

2.2.1 Supernovae Ia

To plot Hubble diagrams, one needs to observe objects with known intrinsic luminosity (or absolute magnitude in astronomy), that can be used to determine the luminosity distance from measurements of the received flux, these sources are called *standard candles*. In the late nineties astronomers found a class of sources particularly suitable for this task: Type Ia Supernovae.
Type Ia supernovae (SN Ia) can be observed when white dwarf stars exceed the mass of the Chandrasekhar limit (1.44 solar masses) and explode. White dwarfs are compact stars made of Carbon and Oxigen, supported by electron degeneracy pressure. This stars are often found in binary systems, so that they can accrete mass from their companion.
The belief is that the mass accreted onto the surface of the white dwarf raises the temperature of the surface layers to such an high value that nuclear burning is initiated and a deflagration front propagates into the interior layers: the entire star undergoes a process of thermal runaway and explodes.
The formation process of SN Ia would be the same irrespective of the cosmic epoch and of their location in the Universe; this explain why this phenomena have a common absolute magnitude independent of the redshift z.
Type Ia Supernovae present a number of features that make them easy to identify and very precise standard candles for cosmological investigations:

- they present peculiar light curves with a maximum luminosity correspondent to an absolute magnitude $M \simeq 19.4$, which makes them as luminous as a little galaxy;
- they are point sources, this allows precise photometric analysis;
- they are rapidly variable sources, with a time scale of order ten days, this allows to distinguish them in a wide field full of stars.

Thank to this features Type Ia Supernovae had been revealed and their redshift measured with good precision until $z \sim 1.5$, providing a direct evidence for the current accelerated expansion of the Universe.
A number of authors have analysed the luminosity distance-redshift relation for Sn Ia, the pioneers in this field were Perlmutter, Riess and Schimdt, who won the Nobel Prize in 2011. Their observations showed substantial deviation from the condition of a matter dominated Universe, as indicated by the fact that the measured luminosities were on the average considerably less than expected, and the Hubble curve bent upward (Fig 2.2). Based on a set of 42 SN Ia in the redshift range $z = 0.18 - 0.83$ and considering a spatially flat Universe with two main component ($\Omega_m^{(0)} + \Omega_\Lambda^{(0)} = 1$) Perlmutter et al. found in 1998 $\Omega_m = 0.28^{+0.09}_{-0.08}$ (1σ statistical) thus showing that about 70% of the energy density of the present universe consists of dark energy.
In 2004 Riess et al. [24] reported the measurement of 16 high-redshift SN Ia with redshift $z > 1.25$ with the Hubble Space Telescope (HST). By including 170 previously known SN Ia data points, they showed that the Universe exhibited a

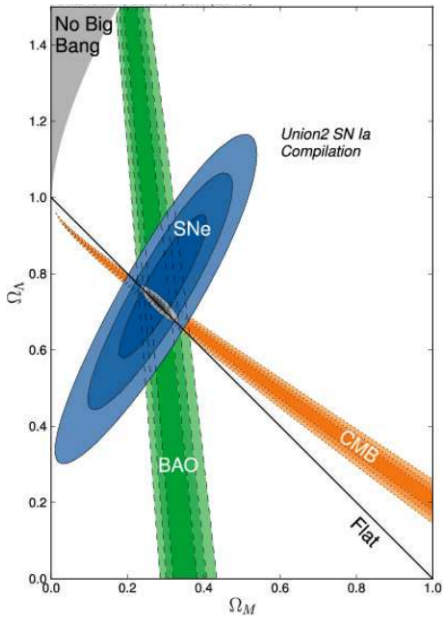

Figure 2.3: The $\Omega_m - \Omega_{DE}$ confidence regions constrained by SN Ia, CMB and galaxy clustering [31

transition from deceleration to acceleration at $> 99\%$ confidence level, in Fig (2.2) left pannel we report the Hubble diagram establish on this dataset.

2.2.2 Cosmic Microwave Background

The Cosmic Microwave Background (CMB) is currently the strongest probe of precision cosmology: even by itself, it places $1-10\%$ level constraints on a large number of cosmological parameters, including the baryon and cold dark matter densities and the amplitude and tilt of the spectrum of primordial fluctuations.
It was first detected in 1965 by Penzias and Wilson during an investigation about the sources of atmospheric noise in telecommunication: a perfect example of serendipity. Despite the lucky circumstances that brought to this discovery, the existence of such a radiation was already predicted by Gamow and other authors in the 40's, as a consequence of the Big Bang model.
The Cosmic Microwave Background consists of photons that last interacted with matter at $z \simeq 1090$ (see Table 2.1), leading informations about the hot primordial Universe and its subsequent evolution.
The FIRAS spectrophotometer of the COBE spacecraft measured the CMB spectrum in the millimetre wavelength range, detecting an almost perfect black-body emission, the energy distribution of which is described by the Planck law:

$$I_\nu = \frac{2h\nu^3}{c^2}\left(\exp\frac{-h\nu}{k_B T} - 1\right)^{-1}. \tag{2.28}$$

The peak of this distribution at $\lambda \approx 2mm$, according to the Wienn law, indicates a radiation temperature $T = 2.728 \pm 0.002K$, see Fig. (2.3).

Following the theory developed so far, we expect the Universe to be hotter and denser in the past, as it is constantly expanding and cooling. Since the energy density of a black body radiation is related to the temperature by the

Stefan-Boltzmann law:

$$\rho_{rad} \propto T^4, \tag{2.29}$$

and we know from the continuity equation (2.12) that $\rho_{rad} \propto a^{-4}$, we get the following scaling of the temperature with redshift:

$$T(a) = \frac{1}{a}T(a_0), \quad T(z) = (1+z)T(z=0). \tag{2.30}$$

Theory and observations of the CMB agree with the existence of a primordial phase in which ordinary matter in the Universe was completely ionized due to the high temperature. The space was filled by an hot plasma and the Compton-scattering led photons and electrons to strong interact until the temperature dropped enough to allow the formation of hydrogen atoms ($T \sim 3000K$). At that epoch, called the *recombination epoch*, the Universe became nearly transparent to radiation because light was no longer being scattered off free electrons.
Until the recombination epoch, the strong coupling between photons and matter determined a condition of thermal equilibrium and thus the emission of a black body radiation. During its propagation toward the observer, the CMB radiation is affected by the cosmic expansion and the cosmological redshift effect determines a change of its temperature, according to Eq. (2.29).
Apart from its near-perfect black-body spectrum, another remarkable feature of this radiation consists in its high isotropy. In the next Chapter we will go into detail on this aspect, for our present purpose we anticipate that the angular distribution of the CMB temperature shows fluctuations of order 10^{-5}. This anisotropes can be statistically analysed in order to constrain all cosmological parameters, the fundamental tool in this kind of study is the angular power spectrum of the CMB.
The study of particular features of the angular power spectrum the so called the acoustic peacks, can constraint the curvature parameter: $\Omega_K \equiv 1 - \Omega_m - \Omega_{DE}$, thus providing the strongest evidence for a spatially flat Universe. The latest measures show $\Omega_K h^2 = 0.1199 \pm 0.0027 \ll 1$ (Planck results 2013), however CMB data alone are not sufficient to distinguish between the contribution of matter and dark energy to the density of the Universe. In Fig (2.4) confidence regions for Ω_m and Ω_Λ (the ΛCDM model is here assumed) are shown, as constrained from different cosmological observable. We see that an efficient way to break the degeneracy and to well distinguish between Ω_m and Ω_Λ, is to match the CMB data with other cosmological observables, in particular SN Ia show confidence contours perpendicular to those coming from CMB.
The state of the art for CMB observations consists in data from the *Planck Surveryor*. Planck was a space observatory operated by the European Space Agency (ESA) from 2009 to 2013. It consisted in a satellite orbiting around the second Lagrangian point of the Sun-Earth system. The Planck Surveryor mapped the full sky in 9 different channels from the radio to the sub-mm, providing excellent angular resolution (5 arcmin). The results for cosmological parameters as measured with Planck CMB data and other complementary observations, are reported in Table 2.1.

Table 2.1. Cosmological parameter values for the ΛCDM model at 68% confidence limits. Column 2 give results from Planck temperature power spectrum data combined with Planck lensing data and WMAP polarization, see Table 2 of

[69]. Column 3 combine the Planck temperature data with polarization, CMB lensing and other external data not collected by Planck, taken from Table 4 of [68]

68% limits cosmological parameters

Parameter	Planck 2013	Planck 2015
$\Omega_b h^2$	0.02205 ± 0.00028	0.02230 ± 0.00014
Ω_m	$0.315^{+0.018}_{-0.016}$	0.3089 ± 0.0062
Ω_Λ	$0.685^{+0.018}_{-0.016}$	0.6911 ± 0.0062
H_0	67.3 ± 1.2	67.74 ± 0.46
n_s	0.9603 ± 0.0073	0.9667 ± 0.0040
σ_8	0.829 ± 0.012	0.8159 ± 0.0086
z_*	1090.43 ± 0.54	1089.90 ± 0.23
Age/Gyr	13.817 ± 0.048	13.799 ± 0.23

2.2.3 Cosmological Constant

The most famous candidate to explain the dynamics of the Universe is a cosmological constant Λ. The cosmological constant is a spatially uniform, time-independent component with equation of state $\omega = -1$. It was introduced by Einstein, as an additional contribution $\Lambda g_{\mu\nu}$ to his equation:

$$R_{\mu\nu} - \frac{1}{2} R g_{\mu\nu} + \Lambda g_{\mu\nu} = 8\pi G T_{\mu\nu}. \tag{2.31}$$

The above represents the most general form for Einstein's field equations, consistently with the principle of general covariance, thus Λ can be simply interpreted as an additional freedom allowed by the theory of General Relativity.
The cosmological constant can be also interpreted as a contribution to the stress-energy tensor coming from the vacuum energy, that is the energy associated with the ground state of quantum fields. Lorentz invariance requires that in any locally inertial reference frame the energy-momentum tensor $T^{(vac)}_{\mu\nu}$ of the vacuum must be proportional to the Minkowski metric $\eta_{\mu\nu}$ (for which $\eta_{ij} = \eta_{j\}} = \delta_{ij}$, $\eta_{00} = -1$), and so in general reference frames $T^{(vac)}_{\mu\nu}$ must be proportional to $g_{\mu\nu}$, thus:

$$T^{(vac)}_{\mu\nu} = -\rho_{vac} g_{\mu\nu} \;\Rightarrow\; p_{vac} = -\rho_{vac}, \quad \omega_{vac} = -1. \tag{2.32}$$

The equation of state for vacuum energy is deduced comparing the above stress-energy tensor with that of a perfect fluid Eq. (2.3). The identification between the vacuum energy and a cosmological constant contribution can be now obtained straightforwardly:

$$\Lambda g_{\mu\nu} = 8\pi G T^{(vac)}_{\mu\nu} \;\Rightarrow\; \rho_{vac} = \frac{\Lambda}{8\pi G} = \rho_\Lambda. \tag{2.33}$$

Inserting the FRLW metric in the extended Einstein equation (2.30), we obtain the following Friedmann equations:

$$H^2 \equiv \left(\frac{\dot{a}}{a}\right)^2 = \frac{8\pi G}{3}\rho - \frac{K}{a^2} + \frac{\Lambda}{3}, \tag{2.34}$$

$$\frac{\ddot{a}}{a} = -\frac{4\pi G}{3}(\rho + 3p) + \frac{\Lambda}{3}. \tag{2.35}$$

This clearly shows that the cosmological constant contributes negatively to the pressure term and hence exhibits a repulsive effect. The dynamics in the limit of

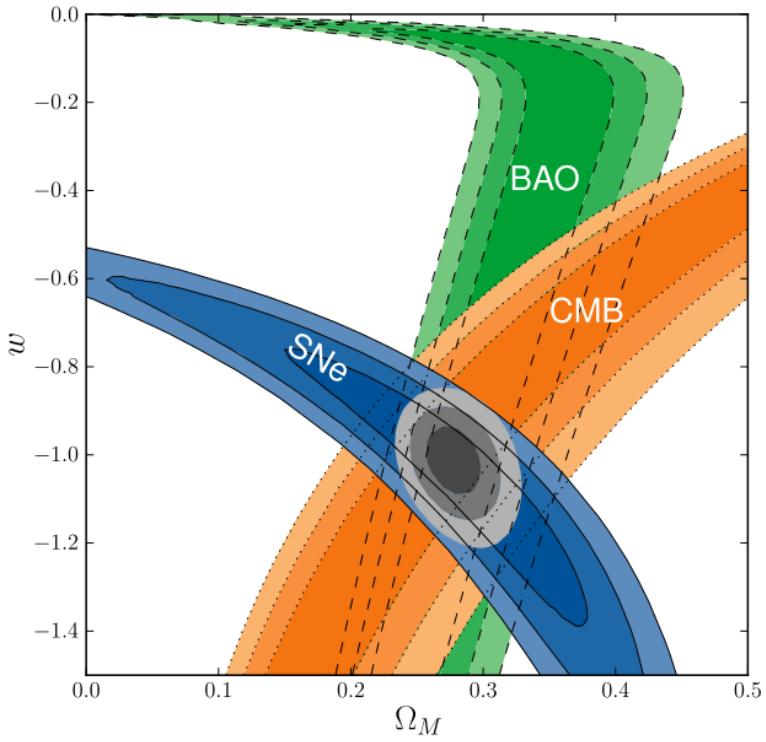

Figure 2.4: The $\omega - \Omega_m$ confidence regions constrained by SN Ia, CMB and galaxy clustering [31]

pure Λ domination ($H^2 \approx \frac{\Lambda}{3}$, $\frac{\ddot{a}}{a} \approx \frac{\Lambda}{3}$) is given by the de Sitter solution that we have already introduced:

$$a(t) \propto \exp(Ht) \tag{2.36}$$

$$H = \sqrt{\frac{\Lambda}{3}} = \sqrt{\frac{8\pi G \rho_\Lambda}{3}} = const. \tag{2.37}$$

2.2.4 Cosmological constant problems

Basing on Friedmann equations Eq. (2.33) and on observational data, we know that Λ is of order the present value of the Hubble parameter H_0:

$$\Lambda \approx H_0^2 \sim (10^{-42} GeV)^2 \;\Rightarrow\; \rho_\Lambda \sim 10^{-47} GeV^4. \tag{2.38}$$

This result give rise to a severe problem of fine tuning when addressing the problem from the point of view of quantum field theory. This can be seen considering the contribution to the vacuum energy of a quantum field with mass m. In quantum field theory each Fourier mode with wave vector k essentially behaves like an harmonic oscillator with frequency $\omega = \sqrt{k^2 + m^2}$ (we use natural units c $= \hbar =$ 1) so that the contribution to the vacuum energy is a sum over all modes of the harmonic oscillator's zero point energy $E_0 = \frac{1}{2}\omega$:

$$\rho_{vac} = \frac{1}{4\pi^2} \int_0^\infty \mathrm{d}k k^2 \sqrt{k^2 + m^2}. \tag{2.39}$$

The energy density above calculated exhibits an ultraviolet divergence: $\rho_{vac} =\propto k^4$. However we expect our current model of particle physics to be only an effective

theory, valid up to a certain cutoff scale E_c, in which case the integral Eq. (2.38) is finite. The Planck scale sets the limit at which GR and the Standard Model of quantum field theory are no longer reconcilable, thus assuming this cutoff to be the Planck energy $E_c = E_{Pl} \sim 10^{19}$, the integral Eq. (2.38) gives:

$$\rho_{vac} = \frac{E_{Pl}^4}{16\pi^2} \sim 10^{74} GeV^4 \tag{2.40}$$

which is about 10^{121} orders of magnitude larger than the observed value given by Eq. This famous discrepancy is called the *cosmological constant problem*. Since the procedure to "rescale" the zero point energy is ad hoc, one can try to properly cancel it introducing counter terms. This requires an enormous fine-tuning to adjust ρ_Λ to the tiny, specific, observed value.
The problem can be slightly ameliorated by assuming that the cutoff scale is lower than the Planck scale. For example, in supersymmetry (SUSY), the contributions to the vacuum energy of fermions and bosons exactly cancel each other out. If supersymmetry is indeed realized in nature, this means that we only have to integrate up to the scale of SUSY breaking $E_c = E_{SUSY}$. Taking $E_{SUSY} \sim 1TeV$, as is commonly expected, this would give $\rho_{vac} \sim 10^{12} GeV^4$, which still gives a discrepancy of 59 orders of magnitude. In order for the fine-tuning problem to disappear, one would need a cutoff scale of order $10^{-2} eV$. However, the standard model has been tested in accelerators up to energies of the TeV scale so we truly cannot get around this huge fine-tuning problem.
Another theoretical problem, although less critical than the one discussed so far, arises from the consideration that the observed values of $\Omega_m \approx 0.3$ and $\Omega_\Lambda \approx 0.7$ indicate that we are in a phase of transition between a pure matter dominated phase and a pure dark energy dominated phase. Indeed we expect this phase to be very short by cosmological standards, in fact: $\frac{\rho_\Lambda}{\rho_m} \propto a^3$.
The problem of why the matter density and the dark energy density should be of the same order exactly now in the long history of the Universe is called the "coincidence problem".

2.3 Beyond standard model

The observations constrain the value of the equation of state today, to be close to that of the cosmological constant $\omega_{DE} = -1.006 \pm 0.045$ [69]. Nevertheless observations actually say relatively little about the time evolution of ω, and so we can consider a situation in which the equation of state of dark energy changes with time.
Evolving scalar fields could mimic the action of a cosmological constant, and they are not ruled out by observations.

2.3.1 Dynamical dark energy

It is generally accepted that the Universe has already experienced a phase of accelerated expansion known as "inflation", at the beginning of its existence.
Inflationary theory provides the correct initial conditions for the standard model of cosmology, solves the flatness and horizon problems as well and explains the origin of density perturbations necessary for subsequent structure formation. Looking

at inflationary theories it is quite natural to think that also in the present epoch the accelerated expansion could be driven by a scalar field.
Scalar fields naturally arise in particle physics including string theory and these can act as candidates for dark energy. So far a wide variety of scalar-field dark energy models have been proposed, the interested reader can find an extended review in [24]. The archetype of such models are definitely Quintessence theories, characterized by the action:

$$S = \int \mathrm{d}^4x\sqrt{-g}\left[\frac{R}{16\pi G} - \frac{1}{2}g_{\mu\nu}\partial^\mu\phi\partial^\nu\phi - V(\phi)\right], \tag{2.41}$$

where g is the determinant of the metric tensor $g_{\mu\nu}$, $V(\phi)$ is the potential of the field. The equation of motion of the scalar field in a flat FRLW space-time is obtained by varying the action with respect of ϕ:

$$\ddot{\phi} + 3H\dot{\phi} + \frac{\mathrm{d}V}{\mathrm{d}\phi}. \tag{2.42}$$

By varying the action with respect of the metric, we obtain the energy momentum tensor:

$$T_{\mu\nu} = \frac{-2}{\sqrt{-g}}\frac{\delta S}{\delta g} = \partial^\mu\phi\partial^\nu\phi - g_{\mu\nu}\left[g^{\alpha\beta}\partial_\alpha\phi\partial_\beta\phi + V(\phi)\right]. \tag{2.43}$$

At the background level the scalar field is homogeneous $\phi = \bar{\phi}(t)$, it doesn't depend on spatial coordinates, and the energy momentum tensor can be substantially simplified:

$$\bar{T}_{\mu\nu} = \begin{pmatrix} -(\frac{1}{2}\dot{\phi}^2 + V(\phi)) & 0 \\ 0 & (\frac{1}{2}\dot{\phi}^2 - V(\phi))\delta_{ij} \end{pmatrix}. \tag{2.44}$$

We see that at the background level the scalar field behaves like a perfect fluid with:

$$\rho_\phi = \left(\frac{1}{2}\dot{\phi}^2 + V(\phi)\right), \quad p_\phi = \left(\frac{1}{2}\dot{\phi}^2 - V(\phi)\right), \quad \omega_\phi = \frac{\frac{1}{2}\dot{\phi}^2 - V(\phi)}{\frac{1}{2}\dot{\phi}^2 + V(\phi)}. \tag{2.45}$$

Inserting the above pressure and density in the Friedmann equations we obtain:

$$H^2 = \frac{8\pi G}{3}\left[\frac{1}{2}\dot{\bar{\phi}}^2 + V(\bar{\phi})\right] \tag{2.46}$$

$$\frac{\ddot{a}}{a} = -\frac{8\pi G}{3}\left[\dot{\bar{\phi}}^2 - V(\bar{\phi})\right]. \tag{2.47}$$

From the last equation we find that the scalar field dynamics produce an accelerated expansion and in particular a nearly de Sitter dynamics with $\omega_\phi \approx -1$ for: $\dot{\bar{\phi}}^2 \ll V(\bar{\phi})$. This condition is verified when the potential is sufficiently flat to determine a slow-roll phase of the scalar field, thus producing a late-time inflationary phase. What we have discussed so far is the "single field slow-roll scenario", representing the basic picture also in the context of primordial inflation. The slow roll condition allows to give a roughly estimate of the mass of the scalar field in quintessence models, which results to be very small:

$$m_\phi = \sqrt{\frac{\mathrm{d}^2V_\phi}{\mathrm{d}\phi^2}} \lesssim H_0 \sim 10^{-33}eV. \tag{2.48}$$

From the action Eq. (2.40) we see that in quintessence the scalar field is minimally coupled to gravity i.e. to the Einstein Hilbert term ($\sqrt{-g}\frac{R}{16\pi G}$) that leads to Einstein's equation, and it is not explicitly coupled to matter. Even if at classical level there is none, a coupling between scalar field and matter arises due to quantum corrections. This coupling would produce, due to the small mass of the field expected in these theories, long range forces that would be in principle observable. Unless there is an underlying symmetry that suppresses these couplings, their values shall be very small, in order to satisfy tests of gravity; this leads to another fine-tuning requirement apart from that necessary to make the cosmological constant itself small.

2.3.2 Modified Gravity

Modified gravity (MG) models are based on the idea of extending General Relativity through the addition of new degrees of freedom and they play an increasingly important role in cosmology as valid alternatives to ΛCDM. There are two main reasons for investigating this field from an observational and a theoretical point of view. The first one is that GR has poorly been tested on scales larger than the solar system. This means that one makes a huge extrapolation of the regime of validity of the theory when using it in cosmological studies. We need to test gravity on large scales, thus it is important to understand the typical observational imprints that would allow to distinguish between alternative models of gravity on such scales.
Secondly this kind of theories can explain the accelerated expansion of the Universe without an explicit Λ term, this allows to avoid the fine tuning problem. The idea is to assume that, for some unknown reason (e.g. some symmetry principle), the cosmological constant is exactly zero and the accelerated expansion is due to a modification of gravity that occurs on large scales. Our ignorance remains, but the problem is moved to an easier one to deal with.
Several mechanisms that allow to construct alternatives models of gravity have been hypothesized by theorists, that usually involve the action of scalar fields, vectors or tensors, for a review we demand to [Modified Gravity and Cosmology]. As a prototype, we consider the so called "scalar-tensor theories" of gravity, that are some of the most established and well studied alternative theories of gravity existing in the literature. They are described by the following action:

$$S = \int \mathrm{d}^4x\sqrt{-g}\left[\frac{R}{16\pi G} - \frac{1}{2}g_{\mu\nu}\partial^\mu\phi\partial^\nu\phi - V(\phi) + \mathcal{L}_M(\psi^i_M, A^2(\phi)g_{\mu\nu})\right]. \quad (2.49)$$

where ϕ is a scalar field with potential $V(\phi)$ and $A(\phi)$ is a coupling function between ϕ and the matter fields ψ^i_M. This action describes a class of theories which generalize Quintessence by allowing the scalar field to conformally couple to matter. By varying the action, we obtain the modified field equation [81]:

$$G_{\mu\nu} = 8\pi G\left[T_{\mu\nu} + \partial_\mu\phi\partial_\nu\phi - g_{\mu\nu}\left(g^{\alpha\beta}\partial_\alpha\phi\partial_\beta\phi + V(\phi)\right)\right]. \quad (2.50)$$

Comparing the above with Eq.(2.2) and Eq. (2.42), we note that in this context the field equations take the same form of the Einstein equation, with the additional contribution of an ordinary scalar field, analogously to Quintessence. The difference lies on the fact that the new scalar field, which will drive the Universe expansion,

mediates also a new fifth force. This fifth force arises from the explicit coupling between the scalar and the matter fields, which modify the geodesics trajectories of particles. By taking the "newtonian" limit of the geodesics equation, i.e. considering a weak and static gravitational field, one ends up with the following result for the acceleration of a test particle in free fall:

$$\ddot{x} = - \bigtriangledown (\Psi_N + \log(A(\phi))). \tag{2.51}$$

The second term produces a fifth force, i.e. a long range force different from newtonian gravity, which depends on the choice of the potential $V(\phi)$ and coupling function $A(\phi)$. The formalism introduced so far, comes from a particular choice of conformal frame, the so called "Einstein frame"
An equivalent description of scalar-tensor theories is given in terms of the action:

$$S = \int \mathrm{d}^4x\sqrt{-\tilde{g}}\frac{1}{16\pi G}\left[\varphi R - \frac{\omega(\varphi)}{\varphi}\tilde{g}_{\mu\nu}\partial^\mu\varphi\partial_\nu\varphi - 2\Lambda(\varphi) + \mathcal{L}_M(\psi^i_M, \tilde{g}_{\mu\nu})\right], \tag{2.52}$$

where $\tilde{g}_{\mu\nu}$ indicates the "Jordan frame" metric tensor, $\omega(\varphi)$ is an arbitrary function Λ is a φ-dependent generalisation of the cosmological constant whereas $\mathcal{L}$ is the lagrangian density that describes the various matter fields ψ^i_M. In this formulation of the theory there is no direct interaction between the scalar field and matter fields, the conformal frame picked out by this choice is usually referred to as the Jordan frame. The modified field equation obtained by varying the action Eq.(2.51) appears somewhat different from the usual Einstein equation, but test-particles in this conformal frame follow geodesics of the metric to which they are coupled, and no such a fifth force appears.
One can switch between the Einstein frame and the Jordan frame via the conformal rescaling of the metrics:

$$\tilde{g}_{\mu\nu} = A^2(\phi)g_{\mu\nu}. \tag{2.53}$$

Nevertheless the trajectories of matter particles end up being the same regardless of which frame one works in.
Thus, models in which scalar fields are conformally coupled to matter predict deviations from GR in principle on all scales. This theories are suited to explain the cosmic acceleration in a natural way but, they also need to pass observational tests.
First of all, the theories needs to satisfy the stringent Solar System constraints, that we here summarize. The deflection angle of stars due to the Sun is observed to be [54 $\theta = (0.99992 \pm 0.00023) \times 1.7500$, where 1.7500 is the prediction of GR. Another relativistic effect is time delay due to the effect of the Sun's gravitational field. This was measured very accurately using the Cassini satellite as: $\Delta t = (1.00001 \pm 0.00001)\Delta t_{GR}$.
Any modified theory of gravity needs to satisfy these stringent constraints on deviations from GR in the Solar System, for this reason scalar field models provide for mechanisms to suppress the modification of gravity (the appearance of fifth force) on small scales. These *screening mechanisms* are realised exploiting the fact that the additional scalar field obeys a non-linear equation of motion driven by the density. The density varies over many orders of magnitude in our Universe. If we expand the density around the cosmological background, the density contrast in the environments where we perform conventional tests of gravity is much larger than one. The screening mechanisms utilise the non-linearity of the scalar field,

driven by the non-linear density contrast, to change the behaviour of the scalar field from cosmological scales to the Solar System.
Currently there is a variety of MG theories providing such screening mechanisms, in this thesis we will analyse the class of K-mouflage models, we refer to Chapter 4 for further details on these models.

Chapter 3

ISW effect

Sky surveys in the various wavelength bands of electromagnetic radiation clearly show that the universe can no longer be considered homogeneous on scales under $\sim 200 Mpc$; in fact it exhibits a variety of structures with a hierarchical organization.
In a bottom up view we can summarize that: stars are organized into galaxies, which in turn form galaxy groups, galaxy clusters, superclusters, sheets, walls and filaments, which are separated by immense voids, creating a vast foam-like structure.
The observed fluctuations in the temperature of the Cosmic Microwave Background are originated from inhomogeneities in the primordial plasma that correspond to the seeds of structures we observe today.
The most important feature of these anisotropies is that they are small enough to consider their evolution in the linear regime. This entails that the correspondence between their sources and what we observe on the Last Scattering Surface (LSS). is easy to model and understand analytically using linear theory.
In this chapter, after introducing the theory of cosmological perturbations and CMB anisotropies, with the necessary formalism, we focus on a particular process generating them. This effect is named Integrated Sachs Woolfe (ISW) and generates sencondary anisotropies (i.e. anisotropies originated after the recombination epoch) in the CMB observed temperature distribution. We argue that the ISW effect arises at the linear level and is caused by time-evolving gravitational potentials. In particular the *late-time ISW* is strictly linked to the appearance of some form of cosmic acceleration at late time. We introduce CMB/galaxies cross-correlation as a way to extract the *late ISW*'s information and ultimately to probe Dark Energy.

3.1 Cosmological perturbations

The most general way to study the evolution of matter inhomogeneities and of CMB anisotropies is to study the system of coupled Einstein and Boltzmann equations. While the Einstein equation describes the evolution of metric perturbations in relation with the distribution of energy and matter, the Boltzmann equation accounts for all the interactions and collisions between different species of particles (photons, neutrinos, electrons, baryons, dark matter and dark energy), see Figure (3.1).
This section is only meant to summarize the main results of this complex theory,

that we will use elsewhere, for a full treatment we refer to [33] [46] [11].
We start from the metrics by defining the line element linearly perturbed, derived from a smooth, spatially flat, FLRW background. The metric perturbations are not uniquely defined, but depend on the so called *gauge choice*. The gauge choice is an identification between the points of the perturbed and the background spacetimes. In this thesis we choose the so called *Newtonian conformal Gauge*. The advantage of working in the Newtonian Gauge is that the metric tensor is diagonal, this simplifies the calculations and leads to simple geodesic equations. Another advantage is that, as we will verify, ϕ plays the role of the gravitational potential in the Newtonian limit and thus has a simple physical interpretation. Therefore, using the conformal Newtonian Gauge the perturbed metrics reads:

$$\begin{aligned} \mathrm{d}s^2 &= a^2(\eta)\left[-(1+2\Phi(\vec{x},\eta))\,\mathrm{d}\eta^2 + (1-2\Psi(\vec{x},\eta))\,\delta_{ij}\mathrm{d}x^i\mathrm{d}x^j\right] \\ \mathrm{d}\eta &\equiv \mathrm{d}t/a(t) \end{aligned} \tag{3.1}$$

where η is the conformal time. Throughout this Section we assume c=1 for simplicity and we use only co-moving coordinates and conformal time, which is related to the scale factor through:

$$\frac{1}{a}\frac{\mathrm{d}a}{\mathrm{d}\eta} = \frac{\mathrm{d}a}{\mathrm{d}t} = aH. \tag{3.2}$$

In the perturbed metric Eq. (3.1) we consider only scalar perturbations, in fact at the linear order, scalar, vector and tensor k-modes, evolve separately and independently; moreover vector modes are always negligible in the standard cosmological model.

3.1.1 Boltzmann equation

The Boltzmann equation describes the statistical behaviour of a thermodynamic system even out of thermodynamic equilibrium. In other words it tells us how the distribution in the phase space of every component of the Universe (photons, neutrinos, electrons, baryons, dark matter and dark energy) changes in consequence of their interactions, see Figure (3.1). It can be symbolically written as:

$$\hat{\mathbb{L}}[f] \equiv \frac{\mathrm{d}f}{\mathrm{d}t} = \hat{\mathbb{C}}[f] \tag{3.3}$$

The term on the left hand side is the Liouville operator, which represents the total derivative of $f(\vec{x},\vec{p},t)$ with respect to time, the term on the right hand side is the collisional term, which accounts for the interactions between particles of the various species.
The distribution function $f(\vec{x},\vec{p},t)$ counts the number of particles in a given region in phase space around position $\vec{x}$ and proper momentum $\vec{p}$. Using the geodesic equation, the Liouville operator can be expressed as the total derivative with respect to an affine parameter λ, in a general relativistic framework:

$$\hat{\mathbb{L}} = P^\mu\frac{\partial}{\partial x^\nu} - \Gamma^\mu_{\nu\gamma}P^\mu P^\nu\frac{\partial}{\partial P^\mu}. \tag{3.4}$$

In the last equality we have introduced the 4-momentum P^μ which we define together with other related quantities:

$$P^\mu \equiv \frac{\mathrm{d}x^\mu}{\mathrm{d}\lambda}, \quad P^2 \equiv g_{\mu\nu}P^\mu P^\nu, \quad p^2 \equiv g_{ij}P^iP^j, \quad \vec{p} = p^i \equiv p\frac{P^i}{|P|} \tag{3.5}$$

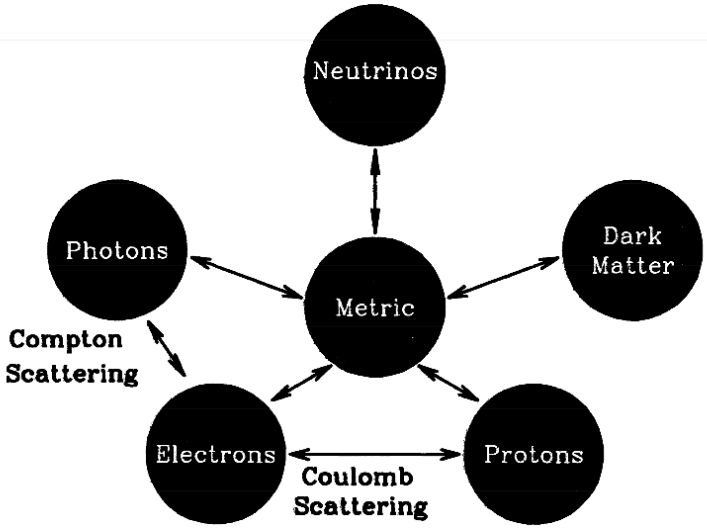

Figure 3.1: The ways in which the different components of the Universe interact with each other. These connections are encoded in the coupled Boltzmann-Einstein equations.[33]

note that in this definition p^i is the proper 3-momentum thus it depends on the scale factor, whereas P^μ (and its spatial part P^i) is a comoving quantity.
The Boltzmann equation is a nonlinear integro-differential equation, thus the only feasible approach to obtain the accuracy required by present and future observations in cosmology, is to find numerical solutions to this equation. To this aim public available codes have been developed, such as CMBfast and CAMB, which allow the computing of the CMB power spectrum and other useful quantities. Here we adopt a simplified perturbative approach and we study the linearised Boltzmann and Einstein equations for radiative and matter components of the Universe.
When working in perturbation theory, it is unnecessary to solve for the complete distribution function, indeed a good strategy consists in considering moments of the distribution. In particular, at the linear level the distribution functions of matter components (baryons and dark matter), can be expressed in terms of the density (zero order moment of the distribution function) and the bulk velocity (first order moment of the distribution function). This approximation works because baryons (indicated with the subscript b) and dark matter (indicated with the subscript dm) are non-relativistic particles, which behave like perfect fluids in a FLRW background.
We thus define the number density and the bulk velocity as integrals of f_m over the 3-momentum $p = g_{ij}P^iP^j$:

$$n_m \equiv \int \frac{\mathrm{d}^3p}{(2\pi)^3} f_m(\vec{x},\vec{p},\eta) \quad \vec{v} \equiv \frac{1}{n_m}\int \frac{\mathrm{d}^3p}{(2\pi)^3} f_m(\vec{x},\vec{p},\eta)\frac{\vec{p}}{P^0} \tag{3.6}$$

where the subscript m indicates the contribution of both the species of matter particles, in this definition the internal degrees of freedom are implicitly included in the distribution function.
For the non-relativistic components such as dark matter and baryons, we suppose

small inhomogeneities in the density:

$$\delta_m(\vec{x},\eta) \equiv \frac{\rho_m(\vec{x},\eta)-\bar{\rho}_m(\eta)}{\bar{\rho}_m(\eta)} = \frac{n_m(\vec{x},\eta)-\bar{n}_m(\eta)}{\bar{n}_m(\eta)}; \qquad (3.7)$$
$$\bar{\rho}_m(\eta) \equiv \langle \rho_m(\vec{x},\eta)\rangle_{\vec{x}}, \quad \bar{n}_m(\eta) \equiv \langle n_m(\vec{x},\eta)\rangle_{\vec{x}}.$$

Now we can write the linearised Boltzmann equations for baryons and dark matter in terms of δ and v, that are first order perturbations of the background averaged (zero-order) distribution. In Fourier space we have:

$$\dot{\delta} + ikv_{dm} = 3\dot{\psi} \qquad (3.8)$$
$$\dot{v}_{dm} + aHv_{dm} = -ik\phi \qquad (3.9)$$
$$\dot{\delta} + ikv_b = 3\dot{\psi} \qquad (3.10)$$
$$\dot{v}_b + aHv_b = -ik\phi + \dot{\tau}\frac{4\bar{\rho}_\gamma}{3\bar{\rho}_b}[v_b + 3i\Theta_1] \qquad (3.11)$$

In the case of dark matter the collisional term on the right hand side of the Boltzmann equation is null because dark matter particles are non-interacting, they only feel the effect of gravity. For this reason Eq. (3.8) and Eq. (3.9) take the same form of the linearised conservation equation for the energy-momentum tensor of a collisionless fluid in a FLRW geometry.
For baryons the situation is slightly different. In the primordial plasma that originated the CMB, electrons and protons interacted strongly via Coulomb scattering, thus we can assume that that effectively behave like a single fluid with the same bulk velocity v_b. Free electrons however, were coupled to photons through the Compton scattering, until the recombination of hydrogen occurred. Thus the collisional term for baryons must take into account this effects
This term contributes only to the velocity Eq. (3.11), i.e. the first moment of the baryon distribution f_b , since both Compton scattering (that couples electrons and photons) and Coulomb scattering (that couples electrons and protons) conserve the number of baryons.
Let us now define formally the anisotropies in the temperature field. We consider photons propagating with momentum $\vec{p}$, at the time η, toward an observer sitting in $\vec{x}_0$. Considering a Bose-Einstein statistic, the distribution of photons in phase-space can be expressed as following:

$$f(\vec{x},\vec{p},\eta) = \left[\exp\left\{\frac{|p|}{T(\eta)[1+\Theta(\vec{x},\hat{p},\eta)]}\right\} - 1\right]^{-1}. \qquad (3.12)$$

In Eq. (3.12) we can identify the mean temperature of the radiation field $T(\eta)$ and the perturbation $\Theta(\vec{x},\hat{p},\eta)$, which depends only on the direction of the photon, not on its energy. Having defined the anisotropies with Eq. (3.12) shows that we assume no spectral deviation from a black-body spectrum, to the first order. This is in completely agreement with COBE results, which observed a perfect black body emission with no spectral distortions.
It will be useful to describe the temperature perturbations' field applying a multipole expansion. We define the lth multipole moment of the temperature field, in Fourier space, as:

$$\Theta_l(\eta) \equiv \frac{1}{(-i)^l}\int_{-1}^{1}\frac{\mathrm{d}\mu}{2}\mathcal{P}_l(\mu)\Theta(k,\mu,\eta) \qquad (3.13)$$
$$\Theta(k,\mu,\eta) = \sum_{l=0}^{\infty}(-i)^l(2l+1)P_l(\mu)\Theta_l(k,\eta).$$

where the $\mathcal{P}_l(\mu)$ is the (orthogonal) Legendre polynomials of order ℓ.
The primordial plasma is optically thick, in fact we can define an optical depth:

$$\tau(\eta) \equiv \int_{\eta}^{\eta_0} \mathrm{d}\eta' a(\eta') n_e \sigma_T \quad \dot{\tau}(\eta) = a(\eta) n_e \sigma_T \tag{3.14}$$

which tells us about the Thomson-scattering rate between photons and electrons (read baryons).[1] The tight coupled limit corresponds to the scattering rate being much larger than the expansion rate: $\tau >> 1$. In this regime photons and baryons behave like a single fluid. It can be shown [33] that in the $\tau >> 1$ limit, the only non-negligible moments are the monopole (ℓ=0) and the dipole (ℓ=1), all others are suppressed by a factor $\sim k/\tau$. More precisely, for a given multipole order, we generally have:

$$\Theta_l \sim \frac{k\eta}{2\tau}\Theta_{l-1}. \tag{3.15}$$

Thus, the larger the factor k/τ, the better to consider only low order moments before recombination.
We also use the approximation of instantaneous recombination (treating the last scattering layer as a surface) in which the radiation behaves as a perfect fluid before recombination ($\tau >> 1$) and as an ensemble of free photons immediately afterwards ($\tau = 0$). Again, this approximation shows better results on large scales.
An other important assumption for our treatment is that v_b has only irrotational component, which is justified by the fact that any eventual vorticity is rapidly suppressed by the cosmic expansion. When Fourier-transforming with this assumption we obtain: $v_b \parallel \vec{k}$; therefore it is convenient to define the variable $\mu \equiv \hat{k} \cdot \hat{p}$ which will label the direction of the photons from now on.
We can finally write the Boltzmann equation for photons at the linear perturbation order, in Fourier space this reads [33][11]:

$$\dot{\Theta} + ik\mu(\Theta + \Phi) = +\dot{\Psi}(k,\eta) - \dot{\tau}\left[\Theta_0(k,\eta) - \Theta + \mu v_b(k,\eta) - \frac{1}{2}\mathcal{P}_2\Pi(k,\eta)\right]. \tag{3.16}$$

This equation describes the evolution of the pattern of anisotropies defined in Eq. (3.12). It takes into account the gravitational interactions, Compton scattering, and generally all the (possibly indirect) interactions between photons and all others components showed in Figure (3.1). The last term $\Pi(k,\eta)$, formally includes the quadrupole moment of radiation and the contribution of polarization, that we will not consider in this thesis. The solution of Eq. (3.16) for Θ involves the solution of equations for all the other coupled perturbation fields and requires initial conditions given by Inflation.

3.1.2 Growth of Matter Pertubations

The large-scale structure of the Universe started to grow after the epoch of the radiation–matter equality. Since non-relativistic matter has a negligible pressure relative to its energy density, the gravitational attraction becomes stronger than pressure repulsion in the matter-dominated epoch. The perturbations of pressureless matter, especially the CDM perturbations, are responsible for the formation of galaxies.

[1] Near recombination the temperature is sufficiently low to consider only Thomson scattering instead of the Compton one

Here we are interested in the evolution of such perturbations.
Starting from the metric in the Newtonian Gauge Eq. (3.1) it is possible to calculate the Ricci tensor and the Ricci scalar to the first order of perturbation, thus obtaining the following expression for the Einstein tensor:

$$G_0^0 = -\frac{3}{a^2} + \frac{1}{a^2}\left[+6\phi\left(\frac{\dot{a}}{a}\right)^2 + 6\frac{\dot{a}}{a}\dot{\psi} - 2\nabla^2\psi\right] \tag{3.17}$$

$$G_0^i = 0 + \frac{1}{a^2}\left[2\partial^i\dot{\psi} + 2\frac{\dot{a}}{a}\partial^i\phi\right] \tag{3.18}$$

$$G_i^0 = 0 + \frac{1}{a^2}\left[-2\partial^i\dot{\psi} - 2\frac{\dot{a}}{a}\partial^i\phi\right] \tag{3.19}$$

$$G_j^i = -\frac{1}{a^2}\left[2\frac{\ddot{a}}{a} - \left(\frac{\dot{a}}{a}\right)^2\right]\delta_j^i + \tag{3.20}$$

$$+ \frac{1}{a^2}\left[\left(2\frac{\dot{a}}{a}\dot{\phi} + 4\frac{\ddot{a}}{a}\phi - \left(\frac{\dot{a}}{a}\right)^2 + \nabla^2\phi + 4\frac{\dot{a}}{a}\dot{\psi} + 2\ddot{\psi} - \nabla^2\psi\right)\delta_j^i + \partial^i\partial_j(\psi - \phi)\right.$$

where the dots denote a derivative with respect to the conformal time $\mathrm{d}/\mathrm{d}\eta$. The above components of the Einstein tensor contain both the zero-order terms (the first addendum on the right hand side of each equation) and the first order corrections.
We note that the traceless contribution to G_j^i depends only on the quantity $(\psi - \phi)$. The right hand side of the Einstein equation is given by the energy momentum tensor.
Generally speaking, the energy-momentum tensor for a certain species of particles in the general relativistic framework can be expressed in terms of the distribution function as:

$$T_\nu^\mu(\vec{x}, t) = -g_i \int \frac{\mathrm{d}^3P}{2\pi^3}\sqrt{-g}\frac{P^\mu P_\nu}{P_0} f_i(\vec{x}, \vec{p}, \eta). \tag{3.21}$$

Considering matter and radiation contributions and using the line element Eq. (3.1), we can expand energy momentum tensor to the first perturbative order, thus obtaining the following equalities:

$$T_0^0 = -\rho_m(1 - \delta_m) - \rho_r(1 - \Theta_{r,0}) \tag{3.22}$$

$$T_i^0 = [\rho_m - 4i\rho_r\Theta_{r,1}] \tag{3.23}$$

$$\left[\hat{k}_i\hat{k}^j - \frac{1}{3}\delta_j^i\right] T_j^i = -\frac{8}{3}\rho_r\Theta_{r,2} \tag{3.24}$$

here the subscript m includes all matter (baryons and dark matter) and the subscript r all radiation (photons and neutrinos). In the last equality, Eq. (3.24), we considered the longitudinal traceless part of T_j^i, which can be extracted by contracting T_j^i with the projection operator $\hat{k}_i\hat{k}^j - \frac{1}{3}\delta_j^i$.
Inserting the above results for G_ν^μ and T_ν^μ in the Einstein equation and subtracting the background terms, we obtain the following set of equations in Fourier space:

$$k^2\psi + 3aH\left(\dot{\psi} + aH\phi\right) = 4\pi G a^2(\bar{\rho}_m\delta_m + 4\bar{\rho}_r\Theta_{r,0}) \tag{3.25}$$

$$k^2(\phi - \psi) = -32\pi G a^2[\bar{\rho}_\gamma\Theta_2 + \bar{\rho}_\nu\mathcal{N}_2] \tag{3.26}$$

$$k^2(\dot{\psi} + aH\phi) = 4\pi G a^2[\bar{\rho}_m v_m - 4i\bar{\rho}_r\Theta_{r,1}]. \tag{3.27}$$

From the above equations we see that the perturbation functions Φ and Ψ, differ in General Relativity, only in presence of a substantial quadrupole moment, which

is essentially carried by neutrinos [2]. However this contribution is sufficiently small at the epoch of our interest, therefore we will assume $\phi = \psi$ in the rest of our analysis. We underline that this difference needs to be included to reach 1% accuracy, in full treatment.
Combining Eq. (3.24) and Eq. (3.26) we obtain an algebraic equation in Fourier space (no temporal derivatives):

$$k^2\psi = -4\pi G a^2 \left[\bar{\rho}_m \delta_m + 4\bar{\rho}_r \Theta_{r,0} + 4\frac{aH}{k}(i\bar{\rho}_m v_m + 4\bar{\rho}_r \Theta_{r,1})\right]. \tag{3.28}$$

This equation reduces to the classical Poisson equation in the limit $k >> aH$, corresponding to scales on which the physical wavelength $\lambda = (2/k)a$ of perturbations is much larger than the Hubble radius H^{-1} (sub-horizon scales), and negligible radiation ($\rho_r \Theta_{r,0} << \rho_m \delta_m$):

$$k^2\phi(\eta, k) \simeq -4\pi G a^2\ \bar{\rho}_m(\eta)\delta_m(\eta, k) = -\frac{3}{2}\Omega_m^{(0)} H_0^2 \frac{1}{a}\delta_m(\eta, k), \tag{3.29}$$

in the last equality we have used the definition of the matter density parameter and the relation between the scale factor and the cosmological redshift Eq. (2.21).
Now we consider the evolution of matter density perturbations, starting from the Boltzmann equation for dark matter inhomogeneities and velocity.[3]. Differentiating Eq. (3.8) and using Eq (3.9) to eliminate $\dot{v}$ and v we obtain:

$$\ddot{\delta} + aH\dot{\delta} = k^2\phi + 3\ddot{\phi} - 3\frac{\dot{a}}{a}\dot{\phi} \tag{3.30}$$

where we have dropped the subscript. The last two terms on the right hand side are negligible with respect to $k^2\phi$ in the sub-horizon limit, thus substituting Eq. (3.29) in Eq. (3.30) we get:

$$\begin{aligned} &\frac{\mathrm{d}^2\delta}{\mathrm{d}\eta^2} + aH\frac{\mathrm{d}\delta}{\mathrm{d}\eta} - a^2H^2\frac{3}{2}\Omega_m\delta = 0, \\ or: \quad &\frac{\mathrm{d}^2\delta}{\mathrm{d}a^2} + \left(\frac{1}{H}\frac{\mathrm{d}H}{\mathrm{d}a} + \frac{3}{a}\right)\frac{\mathrm{d}\delta}{\mathrm{d}a} - \frac{3\Omega_m}{2a^2}\delta = 0. \end{aligned} \tag{3.31}$$

where Ω_m is the time-dependent matter density parameter and in the second equation we changed the variable from η to a. The last equation describes the evolution of sub-horizon matter perturbations in linear regime, well after the epoch of equality between radiation and matter(when the former is negligible). Since Eq. (3.31) is a second-order differential equation with respect to a, there are two independent solutions; a decaying mode and a growing mode which monotonically decreases and increases as a, respectively. The former mode becomes negligibly small as the Universe expands, and thus one is usually interested in the growing mode alone. Notice that the evolution of δ is driven by $H(a)$ and is scale-independent throughout (valid on sub- and super-Hubble scales after radiation-matter equality).
According with the formalism of [33] we define the *growth factor* [4] $D(a)$ from

[2]The quadrupole moment of photons is negligible due to tight coupling with matter
[3] Baryons and dark matter perturbations shows the same behaviour when the second term on the right hand side of Eq. (3.11) is negligible

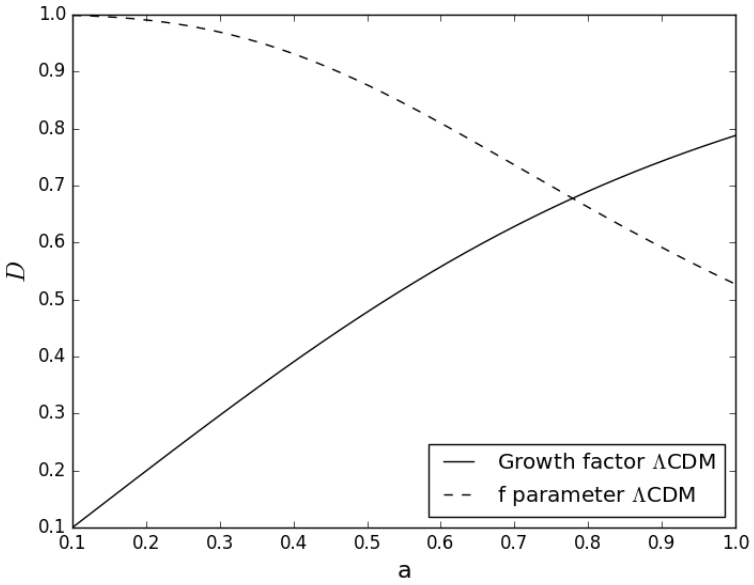

Figure 3.2: The linear growth factor D and the parameter $f \equiv \frac{\mathrm{d}\log D}{\mathrm{d}\log a} \simeq \Omega_m(a)^\gamma$ for the ΛCDM model with parameters in Table 2.1.

the scale independent growing mode of the gravitational potential:

$$\frac{\phi(a)}{\phi(a_{late})} \equiv \frac{D(a)}{a} \tag{3.32}$$

where a_{late} indicates an epoch well after the radiation-matter transition. This can be related to the growth of matter perturbations at sufficiently late time in the regime of validity of Eq. (3.28). During the matter dominated epoch, when $\Omega_m(a) \equiv \frac{8\rho_m(a)}{3H^2} \simeq 1$ and $H(a) \propto a^{-\frac{3}{2}}$ Eq. (3.31) admits analytical solutions:

$$\textit{Growing mode} \quad : \quad \delta(a) \propto a = D(a) \quad \phi(a) = \textit{ constant} \tag{3.33}$$

$$\textit{Decaying mode} \quad : \quad \delta(a) \propto a^{-\frac{3}{2}}. \tag{3.34}$$

More generally in ΛCDM model the solution for the growing mode in open or flat models gives:

$$D(a) = \frac{5\Omega_m^{(0)}}{2}\frac{H(a)}{H_0}\int_0^a \frac{\mathrm{d}a'}{(a'H(a')/H_o)^3}. \tag{3.35}$$

Clearly, if the actual theory of structure growth is not the ΛCDM scenario, the constraints will be modified, the growth equation will be different, and finally the growth factor is changed. Therefore, *the evolution of the growth factor can be used to test the ΛCDM paradigm.*
With this aim we introduce another useful parameter:

$$f \equiv \frac{\mathrm{d}\log D}{\mathrm{d}\log a} \simeq \Omega_m(a)^\gamma, \tag{3.36}$$

where the ΛCDM model predict a value of ~ 0.545 for the growth index γ.
Fig. (3.2) shows the evolution of the linear growth factor computed from Eq. (3.31) and of the parameter f defined in Eq. (3.36).

[4]With this definition the growth factor is in principle different from unity at the present epoch, however for the application discussed in this Chapter we will introduce a growth factor normalized to its present value.

3.1.3 Matter Power Spectrum

In order to study the evolution of $\delta_m(\vec{x},\eta)$ at given scale, the usual procedure is to Fourier transform, taking the comoving wave-vector $\vec{k}$ as parameter. We thus write the Fourier transform of the matter density contrast:

$$\delta(\vec{k},\eta) = \int \mathrm{d}^3x \delta_m(\vec{x},\eta) e^{-i\vec{k}\cdot\vec{x}}. \tag{3.37}$$

Note that we have already used this expansion in Eq. (3.31). When fluctuations are small, i.e. during the linear regime, the Fourier modes evolve independently. [33][59].
The quantity that statistically characterizes the matter density fluctuations at any time and any scale k [5], is the matter power spectrum $P(k,\tau)$, defined from the correlation function of $\delta_k(\tau)$:

$$\langle \delta(\vec{k},\eta)\delta^*(\vec{k}',\eta)\rangle \equiv (2\pi)^3 \delta_D^3(\vec{k}-\vec{k}')P(k,\eta) \tag{3.38}$$

where $\delta^3(\vec{k}-\vec{k}')$ denotes the three-dimensional Dirac delta distribution that account for rotational and translational invariance. Since the distribution of the perturbations is assumed to be statistically homogeneous and isotropic, the power spectrum only depends on the modulus of $\vec{k} : k$. It is a measure of the intensity of the correlation between density fluctuations at a scale $\lambda = 2/k$.
A useful parameter that constrains the current level of the fluctuations, in the galaxy power spectrum is called σ_8 and often referred to as the power spectrum normalization. It is defined ad the root-mean square of matter fluctuations in a sphere of radius $R = 8h^{-1}Mpc$, supposed to be a linear scale. Thus we can write, in terms of the redshift [33]:

$$\sigma_R^2 \equiv \int_0^\infty \frac{\mathrm{d}k}{k} \nabla^2(k,z)|W(kR)|^2, \tag{3.39}$$

where

$$W(kR) = \frac{3j_1(kR)}{kR} \tag{3.40}$$

is the Fourier transform of a normalized top hat window function and j_1 is a spherical Bessel function of the first kind, while:

$$\nabla^2(k,z) = 4\pi P(k,z)k^3/(2\pi)^3 \tag{3.41}$$

is the dimensionless power spectrum. The current value (derived by the Planck collaboration) of σ_8 is reported in Table 2.1.
If the perturbations followed a linear evolution, the evolution of their power spectrum could be expressed using only the growth factor Eq. (3.31). However, the physical transitions occurring in the Universe imprint a scale dependence to that evolution. Among such events, perhaps the most obvious is the density contrast reaching unity, thus breaking down the linearization of equations. One can also mention:

- the radiation domination era affecting the growth of structure,
- super-horizon fluctuations following their own evolution,

[5] $k = |\vec{k}|$ is an inverse scale, generally expressed in units $hMpc^{-1}$

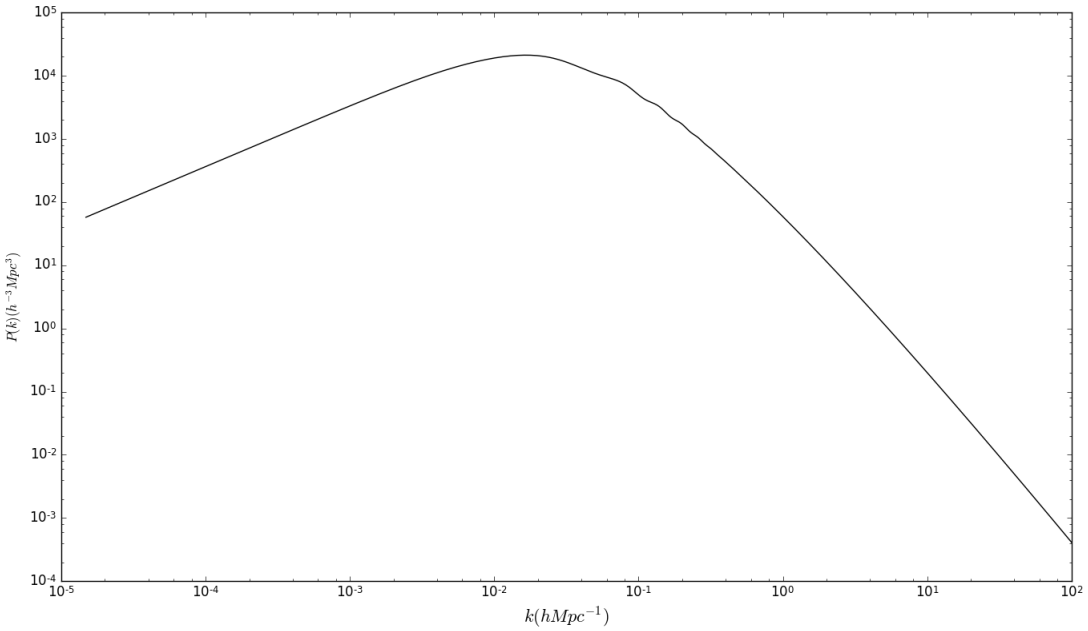

Figure 3.3: Matter power spectrum computed trough the fitting formula given by [35], with cosmological parameters given by Table 2.1 (Planck 2015)

- relativistic species streaming away instead of falling into potential well (photons, neutrinos).

All these transitions are summarized in the transfer function [33]:

$$T(k) \equiv \frac{\Phi(k, a_{late})}{\Phi_{Large-scale}(k, a_{late})}. \tag{3.42}$$

The term at the numerator indicates a scalar metric perturbation at wavenumber k and scale factor a_{late} (referring to a time well after the matter-radiation equality); the term at the denominator refers to a primordial perturbation (generated during inflation) decreased by a small amount ($\sim 9/10$ as shown in [33]), at the same wavenumber.
Taking into account the definition of the growth factor Eq. (3.32), that of the transfer function Eq. (3.42) and using the initial condition (primordial power spectrum) obtained from Inflation, one gets the following expression for the linear matter power spectrum at arbitrary times (redshift) and wavenumber [33]:

$$P(k, z) = 2\pi^2 \delta_H^2 \frac{k^{n_s}}{(H_0)^{n_s+3}} T(k)^2 \frac{D(z)}{D(z=0)}. \tag{3.43}$$

where n_s is the spectral index (given in Table 2.1), δ_H is the amplitude of scalar perturbations at the horizon crossing [33]. In Fig (3.3) we show the present time matter power spectrum for the cosmological parameters in Table 2.1.

3.2 Cosmic Microwave Background Anisotropies

For decades after its discovery, the only known anisotropy in the Cosmic Microwave Background was the dipole due to the Earth motion. Only in 1992, with the COBE satellite, fluctuations of $\sim 10^{-5}$ in the temperature of the CMB

were observed. Over the last twenty years, significant measurements of the CMB anisotropies have also been carried out using balloons and ground-based telescopes, and finally we reached the best ever sensitivity and angular resolution with the (all-sky) Planck Surveryor (2009).

3.2.1 Projected Anisotropies

In a map showing the microwave background temperature across the sky, the features subtending a given angle are associated with physics on a spatial scale. The correspondence depends on the value of the cosmological parameters in a ΛCDM model.
After recombination, the background radiation flows freely through the Universe, almost without further scatterings.[6] An observer today detects the photons that last interacted with matter at redshift z $\sim$ 1000, far beyond the stars and galaxies. The projection effect due to this *free streaming* can be modelled starting from the Boltzmann equation.
Let us rewrite Eq. (3.16) in a clever way, by introducing a source function that is thought to generate photons' fluctuations:

$$\begin{aligned} \dot{\Theta} \quad + \quad & (ik\mu - \dot{\tau})\Theta = e^{-ik\mu\eta+\tau}\frac{\mathrm{d}}{\mathrm{d}\eta}\left[\Theta e^{ik\mu\eta-\tau}\right] = \tilde{S}, \\ \tilde{S} \quad \equiv \quad & +\dot{\Psi} - ik\mu\Phi - \dot{\tau}\left[\Theta_0 + \mu v_b - \frac{1}{2}\mathcal{P}_2\Pi\right]. \end{aligned} \tag{3.44}$$

Neutrinos too, they undergo free streaming starting from their decoupling, long before the recombination of hydrogen. This implies that the main contribution to the quadrupole moment is led by them, because they are not affected by the tight coupling with matter. In this section we will see that the quadrupole of radiation is negligible to generate anisotropies, at least on large scales.
Integrating Eq. (3.44) between an initial time $\eta_{in} \approx 0$ (long before the recombination) and today η_0, with the assumption that the Universe is completely opaque at early epochs $\tau(\eta_{in}) \to \infty$, and noting that $\tau(\eta_0) = 0$, we obtain:

$$\Theta\left(k,\mu,\eta_0\right) = \int_0^{\eta_0} \mathrm{d}\eta \tilde{S}\left(k,\mu,\eta\right) e^{ik\mu(\eta-\eta_0)-\tau(\eta)}. \tag{3.45}$$

If $\tilde{S}$ did not depend on μ we could multiply each side by the Legendre polynomial and than directly integrate the fluctuation field Θ. Doing so, we would obtain a solution for each multipole moment Θ_l, in terms of the spherical Bessel function j_l. In order to do this, we look for a new source function that not explicitly depends on μ.
We can treat the μ-dependence of $\tilde{S}$ using the following substitution in the expression for $\tilde{S}$:

$$\mu \to \frac{1}{ik}\frac{\mathrm{d}}{\mathrm{d}\eta}. \tag{3.46}$$

In fact the exponential factor in Eq. (3.44) allows us to integrate by part each term that contains μ, and than to simply absorb a surface contribution in the definition of the mean temperature that we observe. Let's see it e.g. for the

[6] We do not consider effects such as re-ionization or inverse-Compton scattering by free electrons in clusters of galaxies, which give rise to secondary anisotropies

$-\dot{\tau}\mu v_b$ term:

$$
\begin{aligned}
-\int_0^{\eta_0} \mathrm{d}\eta \dot{\tau}\mu v_b e^{ik\mu(\eta-\eta_0)-\tau(\eta)} &= \frac{i}{k}\int_0^{\eta_0} \mathrm{d}\eta v_b \dot{\tau} e^{-\tau(\eta)} \frac{\mathrm{d}}{\mathrm{d}\eta} e^{ik\mu(\eta-\eta_0)} \\
= \left[\frac{i}{k} v_b \dot{\tau} e^{ik\mu(\eta-\eta_0)-\tau(\eta)}\right]_0^{\eta_0} &- \frac{i}{k}\int_0^{\eta_0} \mathrm{d}\eta e^{ik\mu(\eta-\eta_0)} \frac{\mathrm{d}}{\mathrm{d}\eta}\left[v_b \dot{\tau} e^{-\tau(\eta)}\right] \quad (3.47)
\end{aligned}
$$

where the $\eta = 0$ contribution is damped because of the high opacity, and the η_0 contribution has no angular dependence so it alters the (unobservable) monopole, thus we can ignore it. Now we can define a new source function:

$$
\begin{aligned}
S(k,\eta) \equiv e^{-\tau}\left[+\dot{\Psi} - \dot{\tau}\left(\Theta_0 + \frac{1}{4}\Pi\right)\right] + \\
+ \frac{\mathrm{d}}{\mathrm{d}\eta}\left[e^{-\tau}\Phi + \frac{iv_b}{k} g(\eta)\right] - \frac{3}{4k^2}\frac{\mathrm{d}^2}{\mathrm{d}\eta^2}\left[\dot{\tau} e^{-\tau}\Pi\right], \quad (3.48)
\end{aligned}
$$

which no longer depends from μ. To write an expression for each multipole moment, we need the following relations [33]:

$$
\begin{aligned}
\int_{-1}^{1} \frac{\mathrm{d}\mu}{2} \mathcal{P}_l(\mu) e^{ik\mu(\eta-\eta_0)} &= \frac{1}{(-i)^l} j_l\left[k(\eta-\eta_0)\right] \quad (3.49) \\
j_l(x) &= (-1)^l j_l(-x) \quad (3.50) \\
\frac{\mathrm{d}j_l(x)}{\mathrm{d}\eta} &= j_{l-1}(x) - \frac{l+1}{x} j_{l+1}(x). \quad (3.51)
\end{aligned}
$$

where the j_l's are the spherical Bessel functions [84].
Let us rewrite the source function in terms of $g(\eta) \equiv -\dot{\tau}e^{-\tau}$ and neglecting the small quadrupole term Π:

$$
S(k,\eta) \simeq g(\eta)\left[\Theta_0(k,\eta) + \Phi(k,\eta)\right] + \frac{\mathrm{d}}{\mathrm{d}\eta}\left(\frac{iv_b g(\eta)}{k}\right) + e^{-\tau}\left[\dot{\Phi} + \dot{\Psi}\right]. \quad (3.52)
$$

Recalling now the multipole expansion Eq.(3.13) we can finally integrate the source function Eq.(3.52) and express the solution in terms of j_l's by using Eq. (3.49) and Eq.(3.50), we obtain:

$$
\begin{aligned}
\Theta_l(k,\eta_0) = \int_0^{\eta_0} \mathrm{d}\eta g(\eta)\left[\Theta_0(k,\eta) + \Phi(k,\eta)\right] j_l[k(\eta_0-\eta)] + \\
- \int_0^{\eta_0} \mathrm{d}\eta \frac{iv_b(k,\eta)}{k}\left\{j_{l-1}[k(\eta_0-\eta)] - \frac{(l+1) j_{l+1}[k(\eta_0-\eta)]}{k(\eta_0-\eta)}\right\} \\
\int_0^{\eta_0} \mathrm{d}\eta\, e^{-\tau}\left[\dot{\Phi}(k,\eta) + \dot{\Psi}(k,\eta)\right] j_l[k(\eta_0-\eta)] \quad (3.53)
\end{aligned}
$$

where the second addendum rises from integration by parts and by using the identity Eq. (3.51).
Our goal now is to find a good approximate expression for the integral in Eq. (3.53). In order to do this we first focus on the function:

$$
g(\eta) \equiv -\dot{\tau}e^{-\tau}, \qquad \int_0^{\eta_0} \mathrm{d}\eta g(\eta) = 1 \quad (3.54)
$$

which is called "*visibility function*" and represents the probability that a photon last scattered at the time η. Remembering the definition of the optical depht

$\dot{\tau} = n_e \sigma_T a(\eta)$, we can understand the behaviour of $g(\eta)$. The visibility function is sharply peaked at the epoch of recombination since τ is very large early on, and $\dot{\tau}$ declines rapidly after photons' decoupling.
Moreover, we can assume that the velocity perturbation produces only a dipole term in the anisotropies, to the first order, before the last-scattering, due to tight coupling between radiation and matter. In fact higher multipoles tend to be cancelled out because of the small mean free path of photons. In conclusion: an observer on the LSS can see essentially a monopole and a dipole.
We can thus evaluate the integral in Eq. (3.53) by treating $g(\eta)$ like a δ-function centred in $\eta = \eta_{rec}$ (or using the *saddle-point* approximation) to obtain the following:

$$\begin{aligned}\Theta_l(k,\eta_0) \simeq\ & [\Theta_0(k,\eta_{rec}) + \Phi(k,\eta_{rec})]\, j_l[k(\eta_0-\eta_{rec})] + \\ & + 3\Theta_1(k,\eta_{rec}) \left\{ j_{l-1}[k(\eta_0-\eta_{rec})] - \frac{(l+1) j_{l+1}[k(\eta_0-\eta_{rec})]}{k(\eta_0-\eta_{rec})} \right\} + \\ & \int_0^{\eta_0} \mathrm{d}\eta\ e^{-\tau} \left[\dot{\Phi}(k,\eta) + \dot{\Psi}(k,\eta) \right] j_l[k(\eta_0-\eta)]. \quad (3.55)\end{aligned}$$

This semi-analytic solution provides a result accurate to $5\% - 10\%$ with respect to numerical solutions of Einstein-Boltzmann equations, moreover it is useful to scan different effects that contribute to anisotropies in the linear regime.
The main approximation in our argument has been to consider an instantaneous decoupling between matter and radiation or equivalently a null thickness of the last-scattering layer. However this assumption is not crucial for the aim of this thesis.
As we can see in Eq. (3.55), the major contribution to the multipole moments today, originates from a monopole and a dipole term at the recombination and from an integrate contribution. All anisotropies projected toward us are spread on all multipoles by means of the Bessel functions.
The Bessel functions determines how much anisotropy on an angular scale ℓ^{-1} is contributed by a perturbation mode k: a given k-mode contributes maximally to the angle that the corresponding scale subtends on the sky at last scattering. In a flat model we can write [46]:

$$l_{main} + \frac{1}{2} \sim k(\eta_0 - \eta_{rec}). \quad (3.56)$$

Clearly this angular scale depends on the angular diameter distance to the last scattering surface, which is a function of the cosmological parameters.

3.2.2 Angular Power Spectrum of CMB Anisotropies

The pattern of the angular temperature fluctuations today gives us a direct snapshot of the distribution of radiation and matter at the epoch of recombination, probing the evolution of primordial perturbations in the linear regime. The main tool used in the study of these fluctuations is the angular power spectrum C_l, which is essentially the variance derived from the spherical harmonic expansion of the temperature distribution. The comparison between observed C_l and theoretical ones provides accurate informations about the physics of the primordial plasma of baryons and photons.
Let us recall the definition of radiation temperature fluctuations Eq.(3.12), that

we simply rewrite as:

$$T(\vec{x},\hat{p},\eta) = T(\eta)[1+\Theta(\vec{x},\hat{p},\eta)]. \tag{3.57}$$

This general definition can be specialized to our case of observers sitting in $x = x_0$, thus the direction of the incoming photons can be parametrized by polar coordinates θ, ϕ. The symmetry of the problem allows us to expand the field Θ in spherical harmonics:

$$\Theta(\vec{x},\hat{p},\eta) = \sum_{l=1}^{\infty} a_{lm}(\vec{x},\eta)Y_{lm}(\hat{p}). \tag{3.58}$$

The sum in Eq. (3.57) formally would go from $l = 0$ to $l = \infty$, but practically we can't argue about the monopole, and the dipole is affected by a large error due to the subtraction of the kinematic contribution, which derives from our peculiar motion. At high multipole orders we are limited by the Silk damping and by the instrumental precision, thus the maximum l is next to $l \sim 3000$.
Spherical harmonics have many useful properties, the main one is orthonormality:

$$\int \mathrm{d}\Omega Y_{lm}(\hat{p})Y^*_{l'm'}(\hat{p}) = \delta_{ll'}\delta_{mm'}. \tag{3.59}$$

Now we can Fourier expand $\Theta(\vec{x},\hat{p},\eta)$ and use the definition of multipole moments Eq. (3.13) to get:

$$\Theta(\vec{x},\hat{p},\eta) = \int \frac{\mathrm{d}^3k}{(2\pi)^3} e^{i(\vec{k}\cdot\vec{x})}\Theta(\vec{k},\hat{p},\eta) = \int \frac{\mathrm{d}^3k}{(2\pi)^3} e^{i(\vec{k}\cdot\vec{x})} \sum_{l=0}^{\infty}(-i)^l(2l+1)\mathcal{P}_l(\mu)\Theta_l(k,\eta). \tag{3.60}$$

We can relate spherical harmonics to the Legendre polynomials $\mathcal{P}_l$ using the following:

$$\mathcal{P}_l(\mu) = \frac{4\pi}{2l+1}\sum_{m=-l}^{m=l} Y_{lm}(\hat{k})Y^*_{lm}(\hat{p}). \tag{3.61}$$

Combining Eq. (3.59) with Eq.(3.57) and using also Eq.(3.60) and Eq.(3.58), we obtain:

$$a_{lm}(\vec{x},\eta) = \int \frac{\mathrm{d}^3k}{(2\pi)^3} e^{i(\vec{k}\cdot\vec{x})} \int \mathrm{d}\Omega Y^*_{lm}(\hat{p})\Theta(\vec{k},\hat{p},\eta). \tag{3.62}$$

We can think to $a_{lm}(\vec{x},\eta)$ like a linear response to a random field: the primordial fluctuation field generated during Inflation. The a_{lm}'s are the harmonic coefficients of the Θ-field expansion and represent quantities that we can predict *statistically*. The term statistically indicates the fact that our model can only make predictions about the distribution from which the a_{lm}'s are drawn. The mean value is zero for all a_{lm}'s, so if they are Gaussian distributed (and according to Inflation they are), they are fully characterized by their variance. The variance of the a_{lm}'s defines the *power spectrum* of the CMB anisotropies:

$$\langle a_{lm}\rangle = 0 \quad ; \quad \langle a_{lm}a^*_{l'm'}\rangle \equiv C_l\delta_{ll'}\delta_{mm'} \tag{3.63}$$

where we keep the η dependence implicit.

Since we want to preserve statistical isotropy, we average over the azimuthal

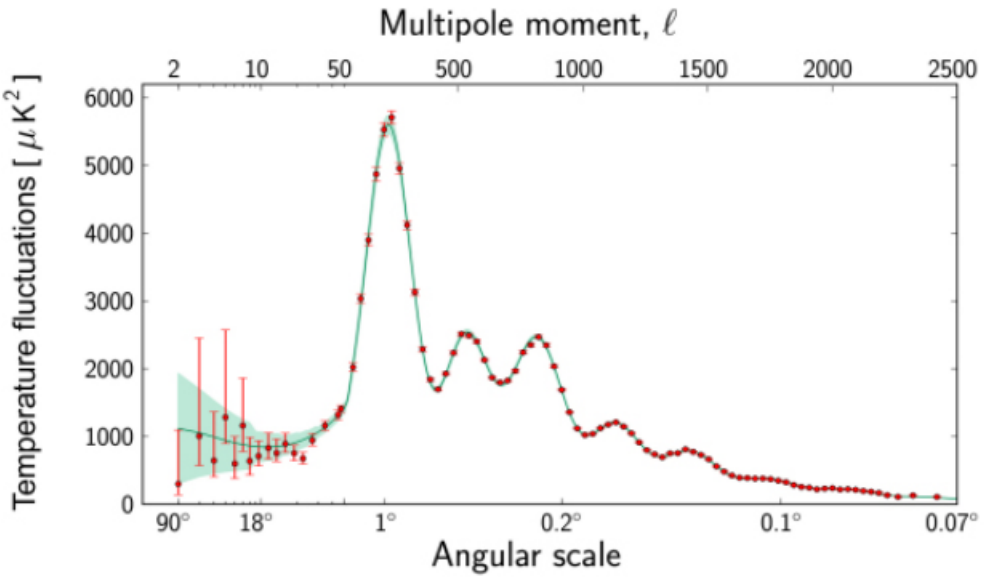

Figure 3.4: The angular power spectrum of CMB anisotropies as measured by Planck Surveyor[83].

number m, i.e. over different multipole orientations on the sky, obtaining a quantity C_l that is independent on m. We assume that this kind of angular average is equivalent to an average over many realizations of the full statistical ensemble, or more practically, over many different observers; thus we can apply the so called "*ergodic hypothesis*".
For a fixed l, we have only $2l+1$ elements in our sample, hence we obtain a fundamental lower limit to the error which affects the C_l. This is called *cosmic variance* and is defined as:

$$\left(\frac{\Delta C_l}{C_l}\right)_{cosmic\ variance} = \sqrt{\frac{2}{2l+1}}. \tag{3.64}$$

We want now to link directly C_l and Θ_l remembering the fact that we are in the linear regime and that, under the inflationary paradigm, we have only a single random field undergoing linear processes, to give rise to all the other random fields. Let us consider two of these random fields: $\Theta(\vec{k},\hat{p})$ and the matter fluctuation field $\delta(\vec{k})$, these two fields are linked by a linear relation. We can highlight this relation simply by taking the ratio $\frac{\Theta(k,\mu)}{\delta(k)}$, which depends only on the magnitude of $\vec{k}$ and on $\hat{k}\cdot\hat{p}=\mu$ because of linear evolution, therefore we can write:

$$\begin{aligned}\langle\Theta(\vec{k},\hat{p})\Theta(\vec{k}',\hat{p}')\rangle = \langle\delta(\vec{k})\delta^*(\vec{k}')\rangle\frac{\Theta(\vec{k},\hat{p})}{\delta(\vec{k})}\frac{\Theta^*(\vec{k}',\hat{p})}{\delta^*(\vec{k}')} = \\ = (2\pi)^3\delta^3(\vec{k}-\vec{k}')P(k)\frac{\Theta(k,\mu)}{\delta(k)}\frac{\Theta^*(k,\mu')}{\delta^*(k)}.\end{aligned} \tag{3.65}$$

In the last equality we used the definition of the matter power spectrum Eq. (3.38). Combining Eq.(3.58) with the definition of C_l Eq. (3.55) and Eq.(3.54), we finally obtain the following expression:

$$C_l = \frac{2}{\pi}\int_0^\infty \mathrm{d}k k^2 P(k)\left|\frac{\Theta_l(k)}{\delta(k)}\right|^2. \tag{3.66}$$

3.2.3 Primary Anisotropies

The anisotropies can be classified as primary, if they are generated on the last scattering surface, and secondary, if the deviations in photons temperature occurs in the journey towards us, after last scattering. The angular scale $\theta \sim 2^\circ$ corresponds to the Hubble radius at recombination. This is the dividing-line between the large-scale inhomogeneities, that have not changed much since inflation, and the small-scale perturbations that have entered the horizon before recombination and been substantially modified by gravitational instability.
In this section we give a qualitative description of the main mechanisms that affect anisotropies generated on the last scattering surface, responsible for the first two terms of Eq. (3.55), the third term of Eq. (3.55) will be object of study in the next Section.

Large Scales
Let us define the *co-moving particle horizon* at the time $\eta_\star$:

$$d_H(\eta_\star) \equiv \int_0^{\eta_\star} \frac{\mathrm{d}t}{a(t)} = \int_0^{\eta_\star} \mathrm{d}\eta. \tag{3.67}$$

this is the spatial scale on which causal processes could have act until the time $\eta_\star$.[7]
On (co-moving) scales larger than $d_H(\eta_{rec})$, micro-physics does not affect anisotropies: the only processes responsible for these anisotropies are non-causal. For this reason the only term to take into account in Eq. (3.55) is the first one.
Now, in both tight coupling and super-horizon ($k\eta << 1$) regimes, the evolution equations for the perturbations assume a really simple form [33]:

$$\dot{\Theta}_0(\vec{k}, \eta) = \dot{\Phi}(\vec{k}, \eta). \tag{3.68}$$

We can solve this equation thanks to the initial conditions set up by inflationary theory (adiabatic and growing mode), the one we need is:

$$\Theta_0(\eta = \eta_{in}) = -\frac{1}{2}\Phi(\eta = \eta_{in})$$

at some initial time $\eta_{in} \approx 0$. Assuming purely matter dominance at $\eta = \eta_{rec}$ we can easily link $\Phi(\eta_{in})$ with $\Phi(\eta_{rec})$ to get:

$$(\Theta_0 + \Phi)(k, \eta_{rec}) \simeq \frac{1}{3}\Phi(k, \eta_{rec}) \tag{3.69}$$

this is the standard "*Sachs Wolfe effect*" [75]. We can think to it as the energy gain (or lost) of a photon moving away from the gravitational well where it is generated on last scattering surface, added to the initial monopole contribution. It's interesting to note that a positive gravitational potential induces a positive perturbation in the temperature field. In other words, when we observe the CMB anisotropies generated by Sachs Wolfe effect, cold spots identifies potential wells . As a result of the linear perturbation theory developed in Sec. (3.1), and precisely from Eq. (3.32) and Eq. (3.33), we can state that the gravitational potential remains constant on all linear scales, in purely matter domination [8].

[7] Note that, using conformal time, the co-moving particle horizon $d_H(\eta_\star)$ trivially coincides with $\eta_\star$; consequently in Fourier-space the condition for a co-moving length $\lambda \sim 1/k$ to be out of the horizon is: $k\eta_\star < 1$

[8] This is valid also for super-horizon scales, as shown in [33]

Assuming now purely matter domination until today (neglecting dark energy and residual radiation), we can immediately evaluate all the quantities in the last equation at the current epoch η_0. By using the cosmological Poisson equation in Fourier space:

$$k^2\Phi(k,\eta) = -4\pi G\langle\rho\rangle a^2(\eta)\delta(k,\eta) \tag{3.70}$$

to relate gravitational potential Φ with matter perturbation, we can write:

$$\Theta_l(k,\eta_0) \simeq \frac{1}{3}\Phi(k,\eta_0) \propto \frac{1}{k^2}\delta(k) j_l[k\eta_0] \Rightarrow \tag{3.71}$$
$$\Rightarrow \left|\frac{\Theta_l(k)}{\delta(k)}\right|^2 \propto \frac{1}{k^4} j_l^2[k\eta_0].$$

Inserting this result in Eq.(3.59), we obtain the contribution to C_l due to SW effect:

$$C_l^{SW} \propto \int_0^\infty \frac{\mathrm{d}k}{k^2} j_l^2[k(\eta_0 - \eta_{rec})]. \tag{3.72}$$

This integral has been solved e.g. by Fabbri, Lucchin and Matarrese (1987), assuming a matter spectrum in the form: $P(k) \propto k^n$, derived from inflationary models. Considering in particular an exact scale-free power spectrum (Harrison-Zel'dovich) $n = 1$ the solution gives:

$$l(l+1)C_l^{SW} \propto \delta_H^2 \tag{3.73}$$

where δ_H is the scalar perturbation amplitude at the horizon-crossing. The plateau that we see in Figure (3.4) at low multipole orders, is the trace of a primordial power spectrum with spectral index near to n=1, in agreement with the theory of Inflation.[9]

Small Scales

Inside the horizon the fluctuations can be affected by causal physics. The main effect of Thomson scattering is the tight coupling between baryons and photons. In this regime we have the establishment of an equilibrium in which the gravitational potential is balanced by the radiation pressure. The main effects visible in the power spectrum are *acoustic oscillations* and *diffusion damping*.
The plotted spectrum presents a series of peaks and troughs starting from the sound horizon's scale at $l \sim 200$, whose amplitude decreases with the scale. This trend can be clearly observed in Figure (3.4). Being in strict relation with the composition of the primordial Universe the features of these peaks are a sensitive diagnostic for the amount of dark matter and baryons and more generally for the principal cosmological parameters.

Acoustic oscillations

Before recombination and above the diffusion scale, tight coupling regime $\tau >> 1$ occurs. In this limit, photons behave just like a fluid, which is described only by the density and the velocity. Hence, neglecting all multipoles up to l=1, we can extract from the radiation Boltzmann equation (3.16), two coupled first order equation in $\dot{\Theta}_0$ and $\dot{\Theta}_1$. These equations are equivalent to one second-order

[9] The best fit power-law flat ΛCDM model obtained from using only the Planck data now gives a scalar spectral tilt of $n_s = 0.9603 \pm 0.0073$

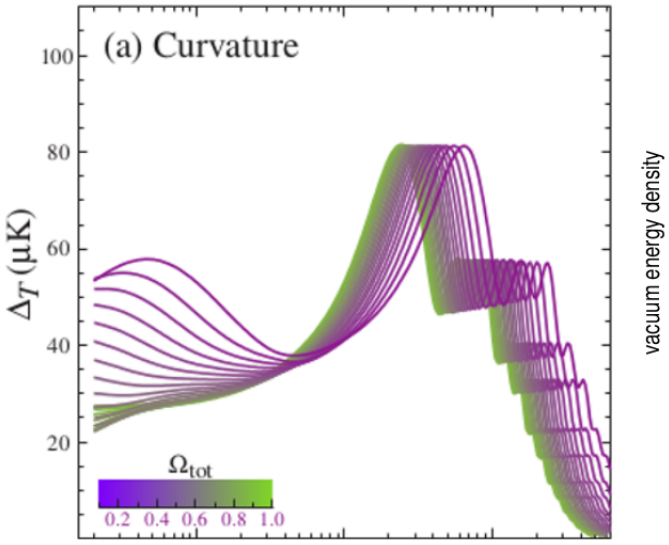

Figure 3.5: The influence of the curvature parameter Ω_K on the angular position of the acoustic peaks. [46]

differential equation:

$$\ddot{\Theta}_0 + \frac{\dot{a}}{a}\frac{R}{1+R}\dot{\Theta}_0 + k^2 c_s^2 \Theta_0 = -\frac{k^2}{3}\Phi + \frac{\dot{a}}{a}\frac{R}{1+R}\dot{\Psi} + \ddot{\Psi} \qquad (3.74)$$

$$R \equiv \frac{3\rho_b^{(0)}}{4\rho_\gamma^{(0)}} \quad ; \quad c_s^2 \equiv \frac{1}{3(1+R)}$$

where c_s is the adiabatic sound speed. Eq. (3.74) describes clearly a damped harmonic oscillator (the oscillating term is Θ_0), and the left hand side represents a forcing term. We see that the dissipative term is due to the Hubble expansion and is proportional to the baryon density, which thus acts as the inertia of the oscillator. Thus the photon-baryon fluid oscillates in both time and space, with a period which is related to the sound speed. It is possible to write an equation analogous to Eq. (3.74) for the dipole Θ_1. Physically the opposite effects of radiation pressure and gravity on the fluid leads to the oscillation of both Θ_0 and Θ_1. It can be shown that these oscillations are in phase opposition. The characteristic physical scale for this phenomenon is the *sound horizon*:

$$r_s(\eta) \equiv \int_0^\eta \mathrm{d}\eta' c_s(\eta') \qquad (3.75)$$

which is the co-moving distance travelled by a sound wave by time η.
These oscillations are imprinted on the last scattering surface, actually they stop when the optical depth goes to zero. The features reflected on the C_l are the so called *acoustic peaks*.
It is worth pointing out an important information we get by observing acoustic peaks. The projection effect of the radiation temperature perturbation that we discussed, is sensitive to the curvature of space-time since the photons move along geodesics. Thus, the same physical scales at the last scattering, are projected

on different multipoles today, changing the energy-content of the Universe. In particular, the multipole order (angular dimension) that corresponds to the first peak can be used to constraint the curvature parameter $\Omega_K \equiv 1 - \Omega_m - \Omega_{DE}$. However, the degeneracy between the contribution of gravitating matter (Ω_m) and dark energy (Ω_{DE}) the curvature , can not be broken using only information derived from the CMB, as we discussed in the previous Chapter.

Silk damping
Diffusion damping is an other effect due to the Thomson scattering between photons and electrons, appearing at very small scales. The effect is due to the finiteness of the mean free path of photons in the primordial plasma: the photons travel a certain distance λ_d between two scatters. This leads to a dissipation of the anisotropies under this scale. This effect is also known as *Silk Damping*.
The damping arises on scales on which it is necessary to take into account higher multipole moments in Eq. (3.16), specifically the quadrupole. In conclusion the effect arises because photons and baryons do not exactly behave like a fluid. The calculation is simplified by neglecting the gravitational potentials in Eq.(3.16). In fact, at these scales, we are dealing with perturbations which entered the horizon before the epoch of equality, hence they were almost cancelled out by the effect of the radiation pressure.

3.3 ISW effect as a probe of Dark Energy

In a Dark Energy dominated universe the gravitational potential varies unlike the case of matter dominated universe. This leads to an imprint on the CMB power spectrum. This phenomenon, the so called *Integrated Sachs-Wolfe* (ISW) effect, provides important help in discriminate between cosmological constant and dynamical Dark Energy models, since the evolution of the gravitational potential strongly depends upon the dynamical properties of the equation of state of dark energy.
As we will show in this Chapter, the Integrated Sachs-Wolfe effect is a sensitive probe for the evolution of the grow factor and an irreplaceable tool to investigate Dark Energy.

3.3.1 Integrated Sachs-Wolfe effect

After last scattering, the photons free stream toward the observer. Only gravitational effects can further alter the temperature. This effect must be integrated along the trajectory of the photons, in principle between last scattering and today.
The last term of Eq. (3.55) accounts for this contribution to anisotropies:

$$\Theta_l^{ISW}(k,\eta_0) \equiv \int_0^{\eta_0} \mathrm{d}\eta\; e^{-\tau} \left[\dot{\Phi}(k,\eta) + \dot{\Psi}(k,\eta)\right] j_l[k(\eta_0-\eta)] \simeq$$
$$\simeq \int_{\eta_{rec}}^{\eta_0} \mathrm{d}\eta\; e^{-\tau} \left[\dot{\Phi}(k,\eta) + \dot{\Psi}(k,\eta)\right] j_l[k(\eta_0-\eta)] \quad (3.76)$$

where the last line arises from tight coupling and instantaneous-recombination assumption. Since the projection effect due to j_l, is similar to that affecting the monopole term on the same multipole order, and basing on the pure gravitational

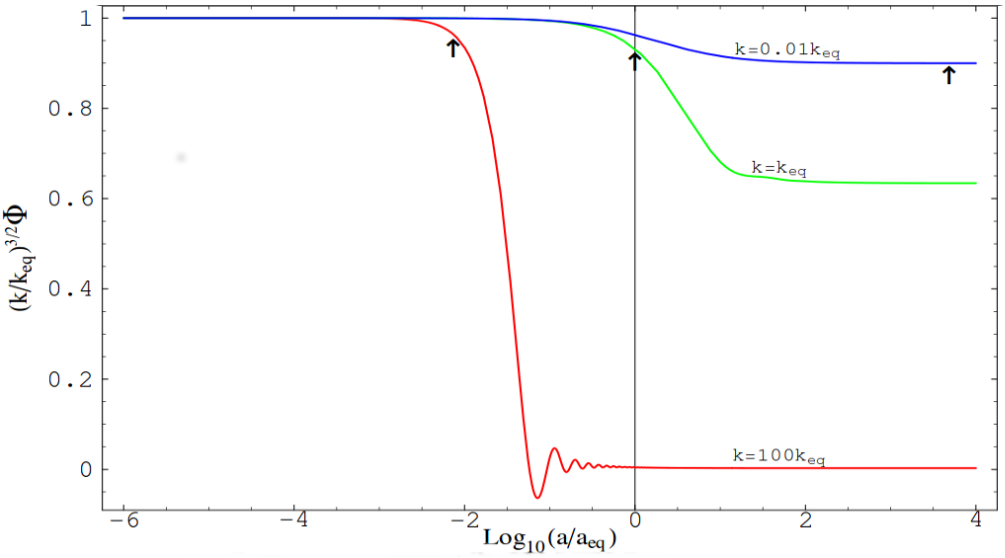

Figure 3.6: The evolution of gravitational potential Φ for 3 different k-modes. The wavenumber is indicated by the label and the epoch at which the k-mode enters the Hubble radius is indicated by a small arrow. Note that, at the epoch of recombination, about $(a_{rec}/a_{eq}) \approx 0.5$ many k-modes are still decaing. Here a flat model with $\Omega_m = 1$ and h=0,5 is assumed. (figure courtesy of Padmanabhan 2006)

nature of the effect, usually people refer to it as: *Integrated Sachs Wolfe* effect (ISW).
The first thing we note is that this contribution vanishes as long as the gravitational potential does not vary in time. As we already mentioned, the gravitational potential remains almost constant before the perturbation enters the particle horizon, in both radiation and matter dominance. This result can be achieved by studying linearised Einstein equations, for super-horizon perturbations in pure growing mode.
The evolution of a perturbation in the linear regime starts as soon as the corresponding k-mode enters the particle horizon. The k-modes who enter the horizon while radiation dominates, suffer the effect of the radiation pressure, that prevents gravitational collapse. The cosmic expansion thus erases the perturbation and the corresponding gravitational potential starts to decay. On the contrary, k-modes which enter the horizon in pure matter dominance, they do not feel any pressure; their gravitational potential is kept frozen by the opposite action of gravity and cosmic expansion, as shown in Figure (3.6).
The epoch of pure matter dominance, during which the time-derivative of gravitational potential is zero, separates two distinct contributions to the ISW effect.

Early-time ISW The transition between the radiation era and the matter era is extended in time. In particular the epoch of equality is approximately at $z \approx 3000$, but at the photons' decoupling ($z \approx 1000$) the radiation energy density is not completely negligible. This leads to the decay of the gravitational potential of perturbations which enter the horizon also near or immediately after last scattering, due to the action of radiation pressure. The anisotropies generated by this decay receive the main contribution at early epochs, soon after the recombination, thus we refer to them as *early ISW* effect.
The visible consequence is a boost on the power spectrum, occurring at the

ℓ's which correspond to k-modes entering the horizon near the recombination. According to Eq. (3.56), this means an enhancement of C_l approximately at the angular scale of the first acoustic peak.

Late-time ISW As we already stated, according to recent observations, we live in a flat Universe almost dominated by some form of Dark Energy. Again, since the Universe expands more rapidly than in pure matter dominance, the gravitational potential decays. The transition to Dark Energy dominance happens at a_{DE} such that: $a_{DE}/a_0 = (\Omega_m/\Omega_{DE})^{1/3}$, which leads to a redshift $z_{DE} \approx 0.3$. This represents a very recent epoch in cosmology, thus the consequent anisotropy is named *late ISW* effect.
Referring to Eq. (3.76) we can evaluate the integral in two opposite regimes, corresponding to two limits for k. The critical value is set up by the particle horizon at a_{DE}, namely: $\eta_{DE} = \eta(a_{DE})$. The two physical regimes are then identified with the limits:

- $k\eta_{DE} << 1$ The wavelength of the perturbation is much longer than the horizon size η_{DE}, photons essentially receive an instantaneous kick. The result is similar to the SW and early ISW effects.

- $k\eta_{DE} >> 1$ In the opposite regime the wavelength is much smaller than the horizon size. The photon traverses many wavelengths during the decay and suffers alternating red and blueshifts from crests and troughs. The result is a cancellation of contributions.

The integral in Eq. (3.76) can be evaluated in this two limits to give [46]:

$$\int_{\eta_{rec}}^{\eta_0} \mathrm{d}\eta\; e^{-\tau} \left[\dot{\Phi} + \dot{\Psi}\right] j_l[k(\eta_0 - \eta)] \simeq \begin{cases} [\Delta\Phi + \Delta\Psi] j_l[k(\eta_0 - \eta_{DE})] & k\eta_{DE} << 1 \\ [\dot{\Phi} + \dot{\Psi}][\eta_0 - (l+1/2)/k] I_l/k & k\eta >> 1 \end{cases} \tag{3.77}$$

where $\Delta\Phi$ and $\Delta\Psi$ are the changes in the potential from the matter-dominated form to the present, the potential at all scales decays at the same rate. The integral I_l is given by:

$$I_l \equiv \int_0^\infty \mathrm{d}x j_l(x). \tag{3.78}$$

Now, considering that Dark Energy domination occurs near the present, late-time ISW affects only low multipole orders. Since the critical scale η_{DE} is almost equal to the particle horizon today, we can conclude that most observable sales fall in the cancellation regime $k\eta_{DE} >> 1$, as shown in Figure (3.7). Compared with the SW effect which predicts a flat spectrum, the *late ISW* contributions fall with l due to cancellation of contributions from over-dense and under-dense regions. The damping does not occur for the early ISW effect. Since it arises when the perturbations are outside or just crossing the horizon, the time scale for the decay is always less than, or comparable to, the light travel time across a wavelength.
We conclude this subsection by mentioning an other kind of ISW effect arising beyond the linear theory. At non-linear level, the potential evolves also during matter domination giving rise to the *Rees-Sciama* effect. This effect is little and it has yet to be detected.

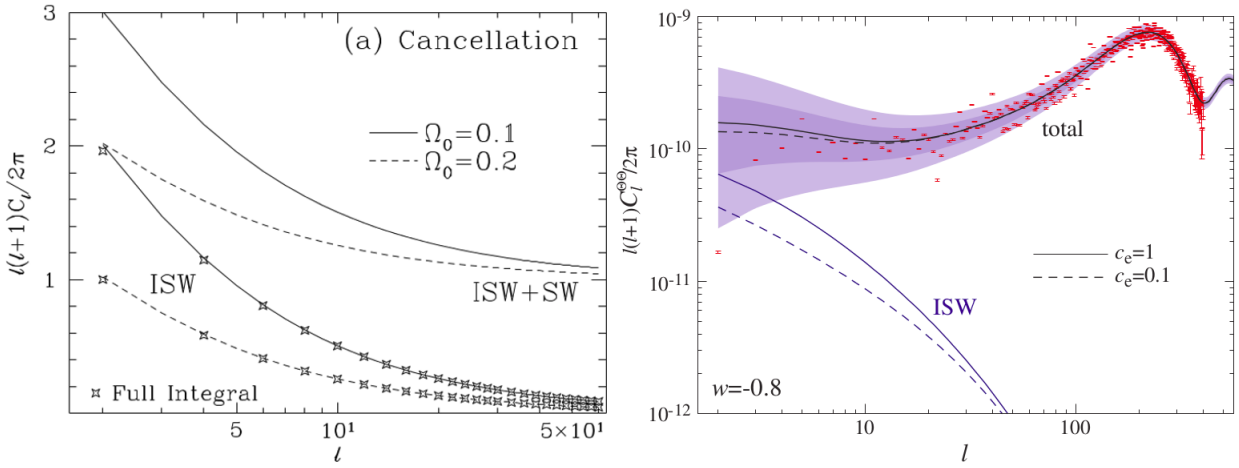

Figure 3.7: **Left**: Boost of the power spectrum at low l due to the *late ISW*. The effect is compared with ordinary Sachs Wolfe for two models with different matter density Ω_m
Right: Contributions to the angular power spectrum of CMB from *late ISW* effect for two different models of Dark Energy. As we can see the ISW signal is smaller than the total signal by factor ∼10. Note that the cosmic variance makes it impossible to distinguish between the two models. [46]

3.3.2 ISW-galaxy Cross-Correlation

We saw that the *late ISW* effect is caused by the decay of the gravitational potential due to a dynamic dominated by Dark Energy at late time. Different models of Dark Energy or Modified Gravity would lead to a different redshift evolution of the gravitational potential, hence to different imprints on the CMB anisotropies. Since, at the linear level, the gravitational potential is linked to the matter distribution by the Poisson's equation, the ISW effect provides a way to test the rate of evolution of the growth factor with redshift. This is a powerful tool to constrain Dark Energy parameters.
Performing a measurement of the *late ISW* effect is, however, a difficult task because of its small signal compared with that of primary anisotropies ($\sim$ 10 times larger), see Fig. (3.7). Furthermore, while on small scales the small differences in temperature tend to cancel out, the large scales, from which the most ISW effect contributions come from, are strongly affected by the cosmic variance 3.64.
In order to bypass the problem of *late ISW* detectability, we can use the link between matter distribution and gravitational potential (Poisson eq.) at the linear level. Thus, if the *late ISW* signal is non-zero, we expect a non-zero correlation among the observed CMB anisotropies and a tracer of the matter distribution on large scales up to redshift $z \approx 2$ [10]. Crittenden and Turok in [29] first proposed that cross-correlating the radiation-temperature anisotropies with some tracer of Large Scale Structure (LSS), e.g. galaxy counts, would give a non-zero result, allowing us to isolate the *late ISW* contribution.
Let us rewrite the temperature fluctuation due to the ISW effect 3.76 as a function

[10] Despite the epoch of Dark Energy starts at $z_{DE} \approx 0.3$ we begin to feel the effect of Dark Energy before that moment

of redshift, in real space:

$$\delta_T^{ISW}(\hat{n}) = -\int_0^{z_{rec}} \mathrm{d}z\ e^{-\tau} \frac{\mathrm{d}}{\mathrm{d}z} \left(\Phi(\vec{r}, z) + \Psi(\vec{r}, z)\right) \quad ; \quad \vec{r} = \chi(z)\hat{n}, \tag{3.79}$$

where $\hat{n}$ is a unit vector along a line of sight. We choose a reference system centred on the observer, the co-moving distance out to redshift z is defined as:

$$\chi(z) = \int_0^z \frac{\mathrm{d}z'}{H(z')}. \tag{3.80}$$

The observed fractional fluctuation in galaxies' counts projected along the line of sight in the direction $\hat{n}$ is:

$$\delta N_g(\hat{n}) = \int_0^\infty \mathrm{d}z \frac{\mathrm{d}N}{\mathrm{d}z} \delta_g(\vec{r}, z) \quad ; \quad \vec{r} = \chi(z)\hat{n}, \tag{3.81}$$

where $\frac{\mathrm{d}N}{\mathrm{d}z}$ is the normalized redshift distribution of galaxies, characteristic of the survey. Galaxies are thought to trace the underlying mass distribution in a way parametrized by the galaxy "bias" . The bias *b(z)* is only a function of z in the linear regime and can be derived from the galaxy auto-correlation function. Thus in the linear regime the fractional fluctuation in galaxies' counts $\delta_g(\vec{k}, z)$ (in Fourier space) is linked to the density-fluctuation as follows:

$$\delta_g(\vec{k}, z) = b(z)\delta(\vec{k}, z = 0)\tilde{D}(z), \quad \tilde{D} = D(z)/D(z = 0) \tag{3.82}$$

where *D(k,z)* is the linear growth function, normalized to unity today. In standard ΛCDM, the growth function depends on z only, but more generally it can have a scale dependence. In analogy with the definition of the CMB angular power spectrum Eq. (3.63), we can define the ISW-galaxy cross-power spectrum as follows:

$$\left\langle a_{lm}^{ISW} \left(a_{l'm'}^{gal}\right)^* \right\rangle \equiv C_l^{ISW-gal} \delta_{ll'} \delta_{mm'}. \tag{3.83}$$

The harmonic coefficients a_{lm} can be obtained by expanding δN_g and δ_T^{ISW} in spherical harmonics and Fourier transform them. For the galaxy counts we get:

$$\begin{aligned} a_{l'm'}^{gal} &= \int_0^\infty \mathrm{d}z \int \frac{\mathrm{d}^3k'}{(2\pi)^3} e^{i\vec{k'}\cdot\vec{r'}} \int \mathrm{d}\Omega\ Y_{lm}^*(\hat{n}') \frac{\mathrm{d}N}{\mathrm{d}z} \delta_g(\vec{k'}, z) \\ &= (i)^l \frac{4\pi}{(2\pi)^3} \int_0^\infty \mathrm{d}z \int \mathrm{d}^3k' Y_{lm}^*(\hat{k}') \frac{\mathrm{d}N}{\mathrm{d}z} \delta_g(\vec{k'}, z) j_{l'}(k'\chi(z)). \end{aligned} \tag{3.84}$$

The last line of Eq. (3.84) has been obtained using the expansion in spherical harmonics of a plane wave [77]:

$$\exp\left(i\vec{k}\cdot\vec{r}\right) = (4\pi) \sum_{l=0}^{\infty} i^l j_l(k\chi) \sum_{m=-l}^{m=l} Y_{lm}(\hat{n}) Y_{lm}^*(\hat{k}) \tag{3.85}$$

and the property of orthonormality of Y_{lm} Eq. (3.59). Identically for the ISW-term we can write:

$$\begin{aligned} a_{lm}^{ISW} &= \int_0^{z_{rec}} \mathrm{d}z \int \frac{\mathrm{d}^3k}{(2\pi)^3} e^{i\vec{k}\cdot\vec{r}} \int \mathrm{d}\Omega\ Y_{lm}^*(\hat{n}) \frac{\mathrm{d}}{\mathrm{d}z} \left(-\Phi(\vec{k}, z) - \Psi(\vec{k}, z)\right) e^{-\tau} = \\ &= (i)^l \frac{4\pi}{(2\pi)^3} \int \mathrm{d}^3k\ Y_{lm}^*(\hat{k}) \int_0^{z_{rec}} \mathrm{d}z \frac{\mathrm{d}}{\mathrm{d}z} \left(-\Phi(\vec{k}, z) - \Psi(\vec{k}, z)\right) e^{-\tau} j_l(k\chi(z)) \end{aligned} \tag{3.86}$$

Now we can insert the expressions for the harmonic coefficients in the definition of the cross-power spectrum and by applying the definition of matter power spectrum Eq. (3.38), we obtain:

$$\left\langle a_{lm}^{ISW}\left(a_{l'm'}^{gal}\right)^*\right\rangle =$$
$$\frac{16\pi^2}{(2\pi)^6}\int \mathrm{d}^3k \int \mathrm{d}^3k' \left\langle \delta(\vec{k})\delta^*(\vec{k'})\right\rangle I_l^{ISW} I_{l'}^{gal} Y_{lm}^*(\hat{k}) Y_{l'm'}(\hat{k}') =$$
$$\frac{16\pi^2}{(2\pi)^3}\int \mathrm{d}^3k \int \mathrm{d}^3k' P(k)\delta^3(\vec{k}-\vec{k}') I_l^{ISW} I_{l'}^{gal} Y_{lm}^*(\hat{k}) Y_{l'm'}(\hat{k}') =$$
$$= \frac{2}{\pi}\int \mathrm{d}k\ k^2 P(k) I_l^{ISW} I_{l'}^{gal}\delta_{ll'}\delta_{mm'} \Rightarrow$$
$$\Rightarrow C_l^{ISW-gal} = \frac{2}{\pi}\int \mathrm{d}k\ k^2 P(k) I_l^{ISW} I_l^{gal}. \tag{3.87}$$

The expression for the cross-power spectrum we found, contains the two redshift integrals:

$$I_l^{gal}(k) = \int_0^\infty \mathrm{d}z\ \frac{\mathrm{d}N}{\mathrm{d}z} b(z)\tilde{D}(z) j_l(k\chi(z)), \tag{3.88}$$

$$I_l^{ISW}(k) = -\int_0^{z_{rec}} \mathrm{d}z\ e^{-\tau}\frac{\mathrm{d}}{\mathrm{d}z}\left(\frac{\Phi(\vec{k},z)+\Psi(\vec{k},z)}{\delta(\vec{k},z=0)}\right) j_l(k\chi(z)). \tag{3.89}$$

We can write an equivalent expression for I_l^{ISW} (and thus for $C_l^{ISW-gal}$) in terms of the rate of change of the growth function. Using the definition of the matter density parameter $\Omega_m^{(0)} \equiv 8\pi G\rho_m^0/3H_0^2$, we can write the Poisson equation in Fourier space as follows:

$$\Phi(\vec{k},z) = -\frac{3}{2}\Omega_m^{(0)}\left(\frac{H_0}{k}\right)^2 (1+z)\delta(\vec{k},z) \tag{3.90}$$

If we neglect the quadrupole moments, thus $\Phi = \Psi$, we can substitute Eq. (3.90) in Eq. (3.89), hence obtaining:

$$I_l^{ISW}(k) = \int_0^{z_{rec}} \mathrm{d}z\ e^{-\tau} D_{ISW}(k,z) j_l(k\chi(z)), \tag{3.91}$$

$$D_{ISW}(k,z) = 3\Omega_m^{(0)}\left(\frac{H_0}{k}\right)^2 \frac{\mathrm{d}}{\mathrm{d}z}\left[(1+z)(\tilde{D}(z))\right]. \tag{3.92}$$

We introduce now the Limber approximation, valid for $l \gtrsim 10$, if *f(k)* is a slow-varying function we can write [78][61]:

$$\int \mathrm{d}k\ k^2\ f(k)\ j_l(k\chi) j_l(k\chi') \approx \frac{\pi}{2}\frac{1}{\chi^2} f\left(k_\perp \equiv \frac{(l+1/2)}{\chi}\right)\ \delta(\chi-\chi') \tag{3.93}$$

Finally we can rewrite the cross-power spectrum as an integral over z only, by using the latter definition of I_l^{ISW} and the Limber approximation we obtain:

$$C_l^{ISW-gal} \approx \int \mathrm{d}z\ \frac{H(z)}{\chi^2(z)}\ b(z)\frac{\mathrm{d}N}{\mathrm{d}z}\ \tilde{D}(z) D_{ISW}(k_\perp,z) P(k_\perp) =$$
$$\int \mathrm{d}z\ \frac{-3H_0^2\Omega_m^{(0)}}{(l+1/2)^2}\ b(z)\frac{\mathrm{d}N}{\mathrm{d}z}\ \tilde{D}(z)\frac{\mathrm{d}}{\mathrm{d}z}[(1+z)\tilde{D}(z)] P(k_\perp). \tag{3.94}$$

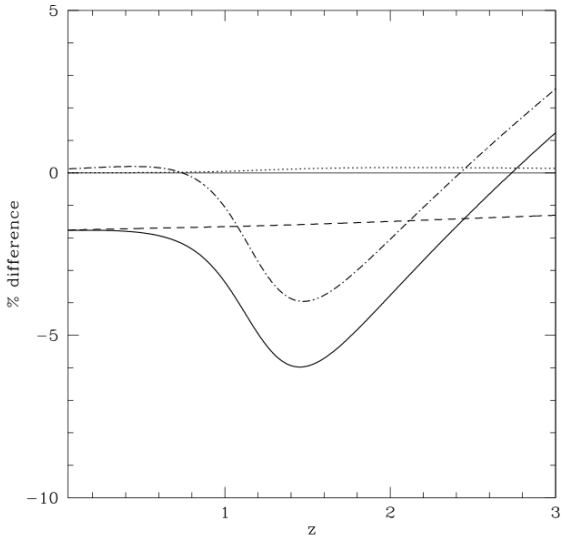

Figure 3.8: The percentage change in: $P(z) = D(z)\frac{\mathrm{d}}{\mathrm{d}z}[(1+z)D(z)]$ (solid line), $d_L(z)$ (dotted line), $D(z)$ (dashed line) and Ω_{DE} (dash-dotted line) as a responce to a 10 % variation in $\omega(z)$ around its mean value between the recombination epoch and today.[71]

3.3.3 Expected results and state of the art

Since the $C_l^{ISW-gal}$ is essentially the product of the growth function and its derivative averaged over a given range of redshifts, cross-correlation is particularly sensitive to the evolution of the the equation of state of Dark Energy as well as its averaged value [70][71]. Figure (3.8) shows the response of the quantity $P(z) = D(z)\frac{\mathrm{d}}{\mathrm{d}z}[(1+z)D(z)]$ to a variation of $\omega(z)$ compared to other quantities that are sensitive to Dark Energy. As we can see the combined dependence on both the growth rate and the cumulative growth factor is the reason why cross-correlation studies can provide a unreplaceable tool to probe Dark Energy. The time-derivative of the growth factor (measured through CMB-galaxy cross-correlation) is also sensitive to dark energy clustering properties. [11] The quantity often used to parametrize dark energy clustering is the dark energy sound speed $c_e^2 \equiv \frac{\delta p_{DE}}{\delta \rho_{DE}}$. Hu and Scranton [48] found that CMB-galaxy cross-correlation is a relatively sensitive probe of the Dark Energy equation of state and is mainly useful as a probe of dark energy clustering.
Moreover, in many models of modify gravity D_{ISW} has a redshift and a scale dependence substantially different from ΛCDM, since the potential evolves also in matter-dominated phase if General Relativity falls. This difference leads to an enhancement in the ISW signal generated in different modify gravity models, allowing us in principal to distinguish GR from alternatives [78].
Despite the hight sensitivity of ISW-galaxy cross-correlation to the details of dark energy models, the method presents large theoretical uncertainties arisen from limitations imposed by cosmic variance and from the fact that, in addition to the ISW contribution, the CMB signal has a sizeable primary component. Theoretical uncertainties in individual $C_l^{ISW-gal}$ are too large to allow comparing different models at each l. For this reason it makes sense to estimate the cumulative

[11] As argued in [21] a smoothly distributed, time-varying Quintessence-component is non-physical because it would violate the equivalence principle. Therefore, dark energy models involving a dynamical field must have fluctuations in the Quintessence-component.

(summed on l) signal-to-noise ratio. In the best conceivable case, we are limited only from cosmic variance and the signal-to-noise ratio in the determination of $\sum_l C_l^{ISW-gal}$ would be:

$$\left(\frac{S}{N}\right)^2 \approx \sum_{l=2}^{l_{max}} (2l+1) \frac{(C_l^{ISW-gal})^2}{(C_l^{ISW-gal})^2 + C_l^{TT} C_l^{gg}}, \tag{3.95}$$

this estimate will be revised in Chapter 6, to take into account other sources of noise.
In the latter equation we considered a full-sky survey, C_l^{TT} indicates the total angular CMB power spectrum, and C_l^{gg} is the analogously defined matter angular power spectrum inside a given window $\frac{\mathrm{d}N}{\mathrm{d}z}$.
So far the cross-correlation method has led to mixed results. As an example Afshordi et al. [2] detected an ISW signal at 2.5 σ level, by cross-correlating WMAP full-sky maps with the projected distribution of extended sources in the Two Micron All Sky Survey. Their signal is consistent with the expected value for the concordance ΛCDM cosmology. On the contrary Sawangwit et al. [77] used WMAP maps with the density map of Luminous Red Galaxies sample, extracted from the Sloan Digital Sky Survey. They found a very poor evidence for the *late ISW* effect at $z \approx 0.7$, quite in contrast with standard ΛCDM model.
A possible way to increase the signal-to-noise in practical applications, is to consider the cross-correlation in multiple redshift shells or bins [48] [70]. If the shells could be selected in a way that they were nearly uncorrelated then one could treat the cross-correlation in each shell as a separate measurement. Moreover, due to projection effects the cross-power spectrum in the higher redshift bins peaks at higher l where the cosmic variance is smaller, thus the binning choice influences the final detectability.
Attempts in this direction as been made e.g. by Giannantonio et al. [Giannantonio et al 2008], who cross-correlated multiple galaxy catalogs with the CMB maps from WMAP. The data used trace the distribution of the LSS in various bands of the electromagnetic spectrum, with median redshifts $0.1 < z < 1.5$, and consist of six catalogs (infrared 2MASS, visible SDSS main galaxies, luminous red galaxies and quasars, radio NVSS, and X-ray HEAO). The measurements were done in real space, calculating the angular cross-correlation functions between the maps. An high degree of correlation is present between data points belonging to different catalogs, due to the partial overlaps in redshift and in sky coverage of the sources. For this reason, they had to take into account the full covariance matrix between all data points, which can be estimated using several statistics method like Monte Carlo and jack-knife. This is an approximation of a true tomographic study of the ISW signal.
Otherwise it is possible to cross-correlate CMB with others LSS tracers, e.g. S. Ili¸ recently proposed [52] to cross-correlate the CMB with the Cosmic Infrared Background, in order to detect *late ISW* signal. He found that such an analysis is expected to reach a significance up to 5 σ in the real cases.
To summarize, detecting the *late ISW* signal through cross-correlation presents some unique advantages, such as:

- It probes the large scales (k=$0.1 \div 0.01h$ Mpc^{-1}) where the evolution of structure is safely inside the linear regime and there is no need for higher order corrections. Moreover the galaxy bias is expected to be independent on scale in the linear regime.

- *Late ISW* can probe the evolution of dark energy at relatively high redshifts, inaccessible by luminosity distance measurements. Thus *late ISW* detection and supernovae observations can be used as complementary probes.

- The cross-power spectrum marks the rate of the growth of structure as well as the total growth. This makes it sensitive to the evolution and clustering properties of Dark Energy, helping also to distinguish between Quintessence and and models with modified gravity.

Despite these attractive features the cross-correlation has a clear weakness: the large cosmic variance that hinders its utility as a precision cosmology probe. Mainly for this reason the method has not yet reached unassailable results.
Improving the determination of the redshift distribution for distant galaxies and optimizing the redshift bin selection, would increase the detectability of *late ISW* signal via cross-correlation. Upcoming galaxy surveys like Euclid and LSST will cover a large redshift range also providing photometric redshifts of the galaxies with high accuracy. This will permit to split a survey into multiple photometric redshift bins allowing for tomographic analysis.

Chapter 4

K-mouflage theory

In this Chapter we outline the theoretical framework for the models of modified gravity that we considered in our work. These scenarios fall under the class of *K-mouflage models*, providing for a mechanism to recover General Relativity on scales at which the latter is well tested.

4.1 Definition of the models

Let us introduce a class of models with an additional scalar-field with respect to General Relativity (GR), in analogy with the scenarios introduced in Sec. (2.3). In particular we consider models whose action in the Einstein frame can be expressed in the following form [14][15]:

$$S = \int \mathrm{d}^4x\sqrt{-g}\left[\frac{M_{Pl}^2}{2}R + \mathcal{L}_\varphi(\varphi)\right] + \int \mathrm{d}^4x\sqrt{-\tilde{g}}\mathcal{L}_m(\psi_m^{(i)}, \tilde{g}_{\mu\nu}). \tag{4.1}$$

This action involves two metrics, the Einstein-frame metric $g_{\mu\nu}$, with determinant g, and the Jordan-frame metric $\tilde{g}_{\mu\nu}$, with determinant $\tilde{g}$ (see Subsection 2.3.2). The matter Lagrangian density, $\mathcal{L}_m$ (where we denote with $\psi_m^{(i)}$ the various matter fields), takes the usual form of GR without explicit coupling to the scalar field. The gravitational sector is described by the usual Einstein-Hilbert action, but in terms of the Einstein-frame metric $g_{\mu\nu}$ and the associated reduced Planck mass $M_{Pl} = 1/(8G)$. We denote with $\mathcal{L}_\varphi(\varphi)$ the Lagrangian density of the scalar field. The two metrics are related by the conformal transformation:

$$\tilde{g}_{\mu\nu} = A^2(\phi)g_{\mu\nu}. \tag{4.2}$$

If the two metrics were identical, i.e. $A(\phi) \equiv 1$, this model would be a simple quintessence scenario with standard gravity described by the General Relativity, as we discussed in Section 2.3. In the most general case Eq. (4.2) gives rise to an explicit coupling between matter and the scalar field and to a modification of gravity.
K-mouflage models are characterized by scalar-field Lagrangian with a non-standard kinetic term:

$$\mathcal{L}_\varphi(\varphi) = \mathcal{M}^4K(\chi), \quad \chi = -\frac{1}{2\mathcal{M}^4}g_{\mu\nu}\partial^\mu\phi\partial^\nu\phi. \tag{4.3}$$

Here $\mathcal{M}^4$ is an energy scale that must be of the order the current dark-energy density density of the Universe, to recover the late time accelerated expansion of

the Universe. For simplicity we choose the potential $V(\phi) = 0$. From Eq. (4.3), we can see that uniform field configurations have $\chi > 0$; thus to describe the evolution of the cosmological background, where all the fields are uniform, we consider only the the $\chi > 0$ of the kinetic function $K(\chi)$.
The form of the kinetic function needs to be specified and different choices are possible. To satisfy the observational constraints, we require the canonical cosmological behaviour, with a cosmological constant, to be recovered at late time, i.e. when the scalar field time derivative tends to the limit: $\chi \ll 1$ (as we will show). We consider here three simple power law models as in [14][15]:

$$K(\chi) = -1 + \chi + K_0\chi^m \quad (4.4)$$
$$K_0 > 0, \quad m \geq 2,$$

$$K(\chi) = -1 + \chi + K_0\chi^m \quad (4.5)$$
$$K_0 < 0, \quad m \geq 2,$$

$$K(\chi) = -1 + \chi - \chi^2 + \chi^3/4. \quad (4.6)$$

The first model Eq. (4.4) corresponds to scenarios where $K' = \mathrm{d}K/\mathrm{d}\chi$ remains positive during the background cosmological evolution (for $\chi > 0$). For large values of χ we have $K \simeq K_0\chi^m > 0$ while for $\chi \to 0$ the kinetic function approaches -1: $K(\chi) \simeq -1 + \chi$. As we will show this corresponds to a cosmological constant behaviour, with $\rho_\Lambda \simeq \mathcal{M}^4$.
The second model in Eq. (4.5) corresponds to scenarios where the equation $K' = 0$ has a solution given by:

$$\chi_* = (-mK_0)^{-1/(m-1)}, \quad (4.7)$$
$$K_* = K(\chi_*) = -1 + \frac{m-1}{m}(-mK_0)^{-1/(m-1)}.$$

where the second line expresses the value of the kinetic function at the critical point χ_*. In this kind of models K' approaches zero from above and is negative for each $\chi > \chi_*$.
The model defined by Eq. (4.6) corresponds to a scenario in which K' has two roots:

$$\chi_* = 2, \ K(\chi_*) = -1; \qquad \chi_* = \frac{2}{3}, \ K(\chi_*) = -\frac{19}{27}. \quad (4.8)$$

The kinetic function is positive for large values of χ and K' approaches the zero from below.
For the coupling function we consider the simple exponential form:

$$A(\varphi) = e^{\beta\varphi/M_{Pl}}. \quad (4.9)$$

In the above equation the field φ has been normalized (without loss of generality) by the appropriate additive constant so that $A(0) = 1$.
The action in Eq. (4.1) is invariant with respect to the transformation $(\phi, \beta) \to (-\phi, -\beta)$, therefore we can choose $\beta > 0$.
Summarizing, in order to fully specify our K-mouflage model we need to fix the following parameters: β, K_0, m, $\mathcal{M}^4$ in addition to the usual cosmological parameters. The model of Eq. (4.6) does not require the parameters K_0, m as the kinetic function is fixed.

4.2 Cosmological background

In this section we derive the evolution equations characterizing K-mouflage cosmology at the background level. Since we are interested in the matter era and subsequent epochs, we consider only two components of the energy density of the Universe: a pressureless matter fluid and the scalar field. In the Einstein frame the field equations assume the same form as in usual General Relativity, the metric $g_{\mu\nu}$ and the Einstein tensor associated with the homogeneous and isotropic background follow the usual FLRW:

$$\begin{aligned} g_{\mu\nu} &= \mathrm{diag}(-1, a^2, a^2, a^2), \\ G_{00} = 3H^2, \quad G_{ij} &= -a^2(2\dot{H} + 3H^2)\delta_{ij}, \end{aligned} \tag{4.10}$$

where we consider a null spatial curvature and the dot indicates the derivative with respect to the proper time.
The matter energy-momentum tensor assumes the usual form of a perfect fluid Eq. (2.3). The Einstein-frame energy-momentum tensor of the scalar field reads as:

$$T_{\mu\nu(\varphi)} = \frac{-2}{\sqrt{-g}}\frac{\delta S_\varphi}{\delta g^{\mu\nu}} = K'\partial_\mu\varphi\partial_\nu\varphi + \mathcal{M}^4 K g_{\mu\nu}. \tag{4.11}$$

The previous expression leads to the definition of the background scalar field density and pressure:

$$\bar{\rho}_\varphi = -\mathcal{M}^4\bar{K} + \dot{\varphi}^2\bar{K}', \quad \bar{p}_\varphi = \mathcal{M}^4\bar{K} \tag{4.12}$$

where the over bars denotes a spatial average.
The energy momentum tensor is conserved in the Jordan frame, while in the Einstein frame the covariant derivative of $T_{\mu\nu}$ gives:

$$\mathrm{D}_\mu T^\mu_{\nu(\varphi)} = (\rho_\varphi - 3p_\varphi)\mathrm{D}_\mu \ln(A), \tag{4.13}$$

$$\mathrm{D}_\mu T^\mu_{\nu(m)} = -\rho_{m,E}\mathrm{D}_\mu \ln(A). \tag{4.14}$$

The previous equations leads to two non-conservation equations for the background matter density $\bar{\rho}_{m,E}$ and the scalar field density $\bar{\rho}_\varphi$ in the Einstein frame:

$$\frac{\bar{\rho}_{m,E}}{\mathrm{d}t} = -3H\bar{\rho}_{m,E} + \frac{\mathrm{d}\ln(\bar{A})}{\mathrm{d}t}\bar{\rho}_{m,E}, \tag{4.15}$$

$$\frac{\bar{\rho}_\varphi}{\mathrm{d}t} = -3H(\bar{\rho}_\varphi + \bar{p}_\varphi) - \frac{\mathrm{d}\ln(\bar{A})}{\mathrm{d}t}\bar{\rho}_{m,E}. \tag{4.16}$$

If the matter is pressureless, it is possible to redefine the above quantities in order to satisfy the standard conservation equation as in ΛCDM model:

$$\rho_m = A^{-1}\rho_{m,E}, \quad \rho_\varphi^{eff} = \rho_\varphi + [A(\varphi) - 1]\rho_m, \quad p_\varphi^{eff} = p_\varphi. \tag{4.17}$$

Using the above rescaling, the conservation equations for the background simply read:

$$\dot{\bar{\rho}}_m = -3H\bar{\rho}_m, \tag{4.18}$$

$$\dot{\bar{\rho}}_\varphi^{eff} = -3H(\bar{\rho}_\varphi^{eff} + \bar{p}_\varphi). \tag{4.19}$$

The Einstein equations lead to the usual Friedmann equations, in terms of the quantities defined in Eq. (4.17):

$$3M_{Pl}^2H^2 = \bar{\rho}_m + \bar{\rho}_\varphi^{eff}, \tag{4.20}$$

$$-2M_{Pl}^2\dot{H} = \bar{\rho}_m + \bar{\rho}_\varphi^{eff} + \bar{p}_\varphi. \tag{4.21}$$

We can now define the time dependent cosmological parameters analogously to ΛCDM:

$$\Omega_m = \frac{\bar{\rho}_m}{3M_{Pl}^2H^2}, \quad \Omega_\varphi = \Omega_{DE} = \frac{\bar{\rho}_\varphi^{eff}}{3M_{Pl}^2H^2}, \quad \omega_\varphi = \omega_{DE} = \frac{\bar{p}_\varphi}{\bar{\rho}_\varphi^{eff}}. \tag{4.22}$$

The dynamics of the scalar field is governed by the Klein-Gordon equation, by varying the action in Eq. (4.1) with respect to φ we obtain:

$$\frac{1}{\sqrt{-g}}\partial_\mu[\sqrt{-g}\partial^\mu\varphi K'] - \frac{\mathrm{d}A}{\mathrm{d}\phi}\rho_m = 0. \tag{4.23}$$

Taking the spatial average of the Klein Gordon equation (4.23) we obtain for the background value of φ:

$$\frac{\mathrm{d}(a^3\dot{\bar{\varphi}}\bar{K}')}{\mathrm{d}t} = \frac{\mathrm{d}\bar{A}}{\mathrm{d}\bar{\varphi}}\bar{\rho}_m a^3, \tag{4.24}$$

$$\ddot{\bar{\varphi}}\left(\bar{K}' + \frac{\dot{\bar{\varphi}}^2}{\mathcal{M}^4}\bar{K}''\right) + 3H\dot{\bar{\varphi}}\bar{K}' = \frac{\mathrm{d}\bar{A}}{\mathrm{d}\bar{\varphi}}. \tag{4.25}$$

Where the above forms are equivalent.

4.2.1 Early-time dynamics

To obtain a realistic cosmology, we should require that we recover the usual matter-dominated expansion at early times, after the epoch of matter-radiation equality. We require therefore the scalar field density to become negligible in the Friedmann equations: $\rho_\varphi^{eff} \ll \rho_m$ and $p_\varphi \ll \rho_m$ as $t \to 0$. With referring to Eq. (4.17) the condition is satisfied if:

$$\rho_m + \rho_\varphi^{eff} \simeq \rho_m \Leftrightarrow A\rho_m + \rho_\varphi \simeq \rho_m. \tag{4.26}$$

Therefore we must have $\rho_\varphi^{eff} \simeq \rho_\varphi \ll \rho_m$ i.e. $A \to 1$ as $t \to 0$, hence:

$$\bar{\varphi} \to 0, \quad A \simeq 1 + \frac{\beta\bar{\varphi}}{M_{Pl}}, \quad \frac{\mathrm{d}A}{\mathrm{d}\varphi} \simeq \frac{\beta}{M_{Pl}}, \quad t \to 0. \tag{4.27}$$

We can then solve the Klein-Gordon equation (4.25), in the limit given by Eq. (4.27). This leads to:

$$a^3\dot{\bar{\varphi}}\bar{K}' = -\frac{\beta\bar{\rho}_m^{(0)}}{M_{Pl}}(t+\gamma), \quad t \to 0, \tag{4.28}$$

where γ is an integration constant to be fixed. To satisfy the condition $\bar{\rho}_\phi \ll \bar{\rho}_m \sim t^{-2}$ we set the integration constant $\gamma = 0$ and require that $m \geq 2$. Notice

that $|\dot{\varphi}| \to \infty$, consequently $\bar{K} \sim \bar{K}_0 \chi^m$ and $\bar{K}' \sim \bar{K}_0 m \bar{\chi}^{m-1}$ as $t \to 0$, thus we obtain the early time behaviour of the scalar field and its derivative:

$$\dot{\bar{\varphi}} = -\,\mathrm{sgn}(K_0) \left(\frac{\beta \bar{\rho}_m (2\mathcal{M}^4)^{m-1} t}{M_{Pl} |K_0| m} \right)^{\frac{1}{2m-1}} \tag{4.29}$$

$$\bar{\varphi} = -\,\mathrm{sgn}(K_0) \frac{2m-1}{2m-2} \left(\frac{\beta \bar{\rho}_m (2\mathcal{M}^4)^{m-1} t^{2m}}{M_{Pl} |K_0| m} \right)^{\frac{1}{2m-1}}. \tag{4.30}$$

All the results expressed here for the early time behaviour in K-mouflage, are also valid for the kinetic model in Eq. (4.6), taking in this case $K_0 = \frac{1}{4}$ and $m = 3$. Taking into account that $\bar{\rho}_m \propto t^{-2}$ during the matter dominated era, we obtain the power law behaviour of $\bar{\varphi}$ and $\dot{\bar{\varphi}}$:

$$|\dot{\bar{\varphi}}| \sim t^{-1/(2m-1)} \ , \ |\bar{\varphi}| \sim t^{2(m-1)/(2m-1)}, \quad t \to 0. \tag{4.31}$$

Inserting the above limit in the definition of $\bar{\rho}_\varphi$, Eq. (4.12), $\bar{\rho}_\varphi^{eff}$, Eq. (4.17) and ω_φ, Eq. (4.22), we obtain:

$$t \to 0 : \quad \bar{\rho}_\varphi \simeq (2m-1)\mathcal{M}^4 \bar{K}, \quad \bar{\rho}_\varphi^{eff} \simeq -\frac{2m-1}{m-1} \mathcal{M}^4 \bar{K}, \tag{4.32}$$

$$p(\varphi) = \mathcal{M}^4 \bar{K}, \quad \omega_\varphi \simeq -\frac{m-1}{2m-1}.$$

Summarizing, we deduce from the above early-time behaviours that: the signs of $\bar{\varphi}$ and $\dot{\bar{\varphi}}$ are opposite to the sign of K_0, while the signs of $\bar{\rho}_\varphi^{eff}$ is the same of K_0 and the equation of state ω_φ tends to a negative constant as $t \to 0$.

4.2.2 Late-time dynamics

In the Einstein frame the masses of particles becomes environmentally dependent and changes according to:

$$\frac{\Delta m_\psi}{m_\psi} = \Delta A(\varphi) \tag{4.33}$$

where m_ψ is the bare mass appearing in the Lagrangian. The theory of Big Bang Nucleosynthesis (BBN) and the observed light elements abundances impose a constraint on the variation of particle masses, which must be less than $\mathcal{O}(30\%)$. This leads to a constraint on ΔA and thus on φ:

$$|\Delta A| \lesssim 1 \ \to \ |\Delta A| = \left| \exp\left(\frac{\beta \bar{\varphi}(t)}{M_{Pl}} \right) - \exp\left(\frac{\beta \bar{\varphi}(t_{BBN})}{M_{Pl}} \right) \right| \simeq \left| \frac{\beta \bar{\varphi}(t)}{M_{Pl}} \right| \lesssim 1 \tag{4.34}$$

as $t_{BBN} \simeq 0$ and $\varphi(t_{BBN}) \to 0$.
The Klein-Gordon equation (4.25), can be expressed in the integrated form:

$$a^3 \dot{\bar{\varphi}} \bar{K}' = \int_0^t \mathrm{d}t' \bar{\rho}_m^{(0)} \frac{\mathrm{d}\bar{A}}{\mathrm{d}\bar{\varphi}}(t'). \tag{4.35}$$

From the BBN constraint we deduce that:

$$\int_0^t \mathrm{d}t' \bar{\rho}_m^{(0)} \frac{\mathrm{d}\bar{A}}{\mathrm{d}\bar{\varphi}}(t') = \bar{\rho}_m^{(0)} \frac{\beta}{M_{Pl}} \int_0^t \mathrm{d}t' \bar{A} \lesssim \bar{\rho}_m^{(0)} \frac{\beta t}{M_{Pl}}. \tag{4.36}$$

Therefore if we take the late time limit ($t \to \infty$) of the Klein-Gordon equation, when we are fully in the dark energy dominated era ($\ddot{a} > 0$) we obtain:

$$t \to \infty : \quad \dot{\bar{\varphi}} \bar{K}' \to 0. \tag{4.37}$$

This condition leads to different behaviours, depending on whether K' has a zero χ_* on the positive semi axis, which will set the large-time dynamics, or not.

Models without χ_*.
We first analyse the class of kinetic models with $K_0 > 0$, described by Eq. (4.4), such models have $K' > 0$ for $\chi \geq 0$. The limits imposed by Eq. (4.27) and Eq. (4.37) to the kinetic function (4.4) imply that $\bar{K}'$ runs down from $+\infty$ to 1 as $\bar{\chi}$ rolls down $+\infty$ to 0 and $\dot{\bar{\varphi}}$ goes from $-\infty$ to 0. Evaluating the Klein-Gordon equation (4.35) and the conservation equation (4.19) in the limit $t \to +\infty$ and taking into account the constraint given by Eq. (4.37), we get the late time behaviour for the model with $K_0 > 0$:

$$\begin{aligned} t \to +\infty \ : \quad & \bar{\rho}_\varphi^{eff} \simeq \mathcal{M}^4, \quad \rho_m \propto a^{-3}, \\ & \dot{\bar{\varphi}} \to 0, \quad \bar{\varphi} \to constant < 0. \end{aligned} \tag{4.38}$$

Thus we recover a cosmological constant behaviour with a dark energy density $\rho_{DE} = \mathcal{M}^4$ and scale factor $a(t) \sim \exp(\mathcal{M}^2 t/(\sqrt{3}M_{Pl})$ in the asymptotic limit $t \to +\infty$.
Because the scalar field energy density ρ_φ^{eff} is negative at early times for models with $K_0 > 0$, see Eq. (4.32), it must change sign and vanish at a time t_c, before reaching the cosmological constant regime. This implies that the equation of state parameter ω_φ should diverge at t_c. This time t_c must occur sufficiently far in the past, in order to satisfy observational constraints on ω_{DE} at low redshifts $z \ll 1$; in this way when ρ_φ^{eff} becomes of the order ρ_m we are close to the cosmological constant regime with $\omega_\varphi = \omega_{DE} \simeq -1$.

Models with χ_*
We consider now the case of kinetic models such that $K' = 0$ at some positive value χ_*, like those described by Eq. (4.5) and Eq. (4.6). Following the Klein-Gordon equation (4.35), χ rolls down from $+\infty$ and converge at late time to the largest solution χ_* of $K'(\chi_*) = 0$, in order to obey the asymptotic behaviour given by Eq. (4.37).
In the case of the kinetic function (4.5), there is a single critical point given by Eq. (4.7) and K' is negative at large values of χ, to the right of χ_*. Thus instead of φ converging to zero as in the previous case, now φ converges to a constant (fixed by the value of χ_*) at large times, and the asymptotic solution gives:

$$\begin{aligned} t \to +\infty \ : \quad & \bar{\rho}_\varphi^{eff} \simeq -K_* \mathcal{M}^4, \quad a(t) \sim \exp(\sqrt{-K_*}\mathcal{M}^2 t/(\sqrt{3}M_{Pl}), \\ & \dot{\bar{\varphi}} \to \sqrt{2\chi_* \mathcal{M}^4}, \quad \bar{\varphi} \to \sqrt{2\chi_* \mathcal{M}^4} t. \end{aligned} \tag{4.39}$$

To recover a cosmological constant behaviour $-\bar{p}_\varphi \simeq \bar{\rho}_\varphi^{eff} \simeq -K_* \mathcal{M}^4 > 0$ the kinetic function Eq. (4.5) must satisfy the condition $K_* < 0$ which in turns implies $K_0 < -(m-1)^{m-1}/m^m \sim -1$. This implies that scenarios with $|K_0| < 1$ are ruled out and the remaining scenarios have $\bar{K}' < 0$ and $\bar{K} < 0$ at all times.
In particular, the scalar field energy density is now positive both at late and early

times and does note change sign. Hence, contrary to the class of models Eq. (4.4), the equation of state parameter never diverges.
For the model described by Eq. (4.6) the largest zero of K' corresponds to $\chi_* = 2, \quad K(\chi_*) = -1$. Because $K_* < 0$ this also corresponds to a positive cosmological constant $\rho_{DE} = \bar{\rho}_\varphi^{eff} \simeq K(\chi_*) - \mathcal{M}^4$ at late times, similarly to the previous case. However, contrary to the model (4.5), K' is positive for $\chi > \chi_*$, thus K grows and becomes positive for large χ. This implies, considering the early time limit given by Eq. (4.32), that the the scalar field energy density $\bar{\rho}_\varphi^{eff}$ must change sign at a time t_c , where the effective equation of state parameter diverges. On the other hand, because of the zero χ_*, $\bar{\varphi}$ grows linearly with time as in Eq. (4.39) at late times, but to negative values as:

$$t \to +\infty \ : \quad \bar{\rho}_\varphi^{eff} \simeq -K_* \mathcal{M}^4, \quad a(t) \sim \exp(\sqrt{-K_*}\mathcal{M}^2 t/(\sqrt{3}M_{Pl}),$$
$$\dot{\bar{\varphi}} \to -\sqrt{2\chi_* \mathcal{M}^4}, \quad \bar{\varphi} \to -\sqrt{2\chi_* \mathcal{M}^4}\, t. \tag{4.40}$$

4.3 Linear perturbations

In this section we give the basic results for the linear perturbation theory arising in K-mouflage models, with the aim of studying the growth of matter perturbation at the linear level.
The perturbed metric in the Einstein frame, using the Newtonian conformal gauge [65][20][33], assumes the same form as in ΛCDM, see Eq (3.1).
In this Section we adopt the conformal time(η) and comoving coordinates as in Sec. (3.1).
In the Newtonian gauge, the velocity 4-vector that enters the matter energy-momentum tensor Eq. (2.3), is given by:

$$u^\mu = a^{-1}(1 - \Phi + v^2/2, v^i), \quad u_\mu = -a^{-1}(1 - \Phi + v^2/2, -v^i), \tag{4.41}$$

where we denote the peculiar velocity:

$$v^i = \frac{\mathrm{d}x^i}{\mathrm{d}\eta}. \tag{4.42}$$

In the following calculation we consider the weak-field non-relativistic regime $\Phi \sim \Psi \sim v^2 \ll 1$ and we neglect the contribution of radiation, as in the previous Section. Studying the traceless part of the Einstein equation in this approximation it is possible to show [17] that the difference between Φ and Ψ is negligible at the linear order, thus the metric reads:

$$\mathrm{d}s^2 = a^2(\eta)\left[-\left(1 + 2\Psi_N(\vec{x}, \eta)\right)\mathrm{d}\eta^2 + \left(1 - 2\Psi_N(\vec{x}, \eta)\right)\delta_{ij}\mathrm{d}x^i\mathrm{d}x^j\right], \tag{4.43}$$

where we set $\Phi = \Psi = \Psi_N$.
From the $\nu = 0$ component of the non-conservation equation (4.14), we obtain the continuity equation [17][15]:

$$\frac{\mathrm{d}\rho_{m,E}}{\mathrm{d}\eta} + \nabla \cdot (\rho_{m,E}\vec{v}) + 3Ha\rho_{m,E} = \rho_{m,E}\frac{\partial \ln A}{\partial \eta}. \tag{4.44}$$

Using the matter density introduced in the previous Section $\rho_m = A^{-1}\rho_{m,E}$, the continuity equation assumes the same form as in the Λ CDM case [15]:

$$\frac{\mathrm{d}\rho_m}{\mathrm{d}\eta} + \nabla \cdot (\rho_m \vec{v}) + 3Ha\rho_m = 0, \tag{4.45}$$

where we have neglected a term $(\vec{v}\cdot\nabla)\ln A$ which is of order $\partial_\eta v^2$.
From the spatial $\nu = i$ components of Eq. (4.14) we obtain the Euler equation in K-mouflage models [17][15]:

$$\frac{\partial\vec{v}}{\partial\eta} + (\vec{v}\cdot\nabla)\vec{v} + \left(aH + \frac{\partial\ln A}{\partial\eta}\right)\vec{v} = -\nabla(\Psi_N + \ln A). \tag{4.46}$$

Note the term $\nabla\ln A$ on the right hand side, that represents a fifth force contribution.
Within a perturbative approach, we suppose now small fluctuations in the densities ($\delta\rho_i = \rho_i - \bar{\rho_i}$) and in the scalar field ($\delta\varphi = \varphi - \bar{\varphi}$). From the 0-0 component of the Einstein equation in K-mouflage, we obtain in the non-relativistic weak-field limit [15]:

$$\nabla^2\Psi_N = \frac{a^2}{2M_{Pl}^2}(\delta\rho_{m,E} + \delta\rho_\varphi) = \frac{a^2}{2M_{Pl}^2}(\delta\rho_m + \delta\rho_\varphi^{eff}). \tag{4.47}$$

The scalar field perturbations $\delta\varphi$, are related to the matter density perturbations $\delta\rho_m$ trough the Klein-Gordon equation (4.23), that can be written as:

$$\frac{1}{a^3}\frac{\partial}{\partial t}\left(a^3\frac{\partial\varphi}{\partial t}K'\right) - \frac{1}{a^2}\nabla\cdot(\nabla\varphi K') = -\frac{\mathrm{d}A}{\mathrm{d}\varphi}\rho_m, \tag{4.48}$$

with:

$$\chi = \frac{1}{2\mathcal{M}^4}\left[\left(\frac{\partial\varphi}{\partial t}\right)^2 - \frac{1}{a^2}(\nabla\varphi)^2\right]. \tag{4.49}$$

Therefore, linearising the Klein-Gordon Eq. (4.48), we obtain for sub-horizon scales and in Fourier space:

$$k/aH \gg 1: \quad \delta\varphi \simeq \frac{\bar{A}\beta a^2}{M_{Pl}K'k^2}\delta\rho_m. \tag{4.50}$$

In the sub-horizon regime, if we take $\rho_m \sim H^2M_{Pl}^2$, it is possible to obtain the following estimates:

$$k/aH \gg 1: \qquad \frac{\delta A}{A} \sim \frac{\beta\delta\varphi}{M_{Pl}} \sim \frac{\beta^2a^2H^2}{K'k^2}\frac{\delta\rho_m}{\rho_m} \ll \frac{\delta\rho_m}{\rho_m}, \tag{4.51}$$

$$\frac{\delta\rho_\varphi}{\delta\rho_{m,E}} \sim \frac{\beta^2\delta\varphi}{M_{Pl}} \sim \frac{\beta^2a^2H^2}{K'k^2}\left(1 + \frac{\delta\rho_m}{\rho_m}\right) \ll 1. \tag{4.52}$$

Indeed the Poisson Eq. (4.47) simplifies, as we can neglect $\delta\rho_\varphi$ and write:

$$\nabla^2\Psi_N \simeq \frac{a^2}{2M_{Pl}^2}\delta\rho_{m,E} = \frac{a^2}{2M_{Pl}^2}A\delta\rho_m. \tag{4.53}$$

Furthermore, using Eq. (4.51) we can neglect fluctuations of A in the Euler equation.
It is now possible to linearise the continuity equation (4.45) and the Euler Eq. (4.46); keeping in mind that the peculiar velocity is already a first order term, we can write in Fourier space:

$$\frac{\partial\delta_m}{\partial\eta} + ikv = 0, \tag{4.54}$$

$$\frac{\partial\vec{v}}{\partial\eta} + \left(aH + \frac{\mathrm{d}\ln\bar{A}}{\mathrm{d}\eta}\right)\vec{v} + ik\Psi_{tot} = 0, \tag{4.55}$$

where $\delta_m = \delta\rho_m/\bar{\rho}_m$ and we have introduced the total potential Ψ_{tot}. This quantity accounts for the gravitational force and the fifth force. From the Poisson equation (4.53) and Eq. (4.51) the total potential reads:

$$\Psi_{tot} = \Psi_N + \delta(\ln A) = -\frac{a^2\bar{A}}{2k^2M_{Pl}^2}\left(1 + \frac{2\beta^2}{K'}\right)\delta\rho_m. \tag{4.56}$$

4.3.1 Growth Factor equation

Combining Eq. (4.54), Eq. (4.55) and Eq. (4.56) we obtain the evolution equation for matter fluctuation at the linear perturbative order and on sub-horizon scales in K-mouflage:

$$\frac{\mathrm{d}^2\delta_m}{\mathrm{d}\eta^2} + aH(1+\epsilon_2)\frac{\mathrm{d}\delta_m}{\mathrm{d}\eta} - a^2H^2\frac{3}{2}\Omega_m(1+\epsilon_1)\delta_m = 0, \tag{4.57}$$

where Ω_m is the time-dependent matter density parameter in K-mouflage, defined in Eq. (4.22). In the above equation we have introduced the coefficients:

$$\epsilon_1(\eta) \equiv \bar{A} - 1 + \frac{2\bar{A}\beta^2}{\bar{K}'}, \quad \epsilon_2 \equiv \frac{\mathrm{d}\ln\bar{A}}{\mathrm{d}\ln a}. \tag{4.58}$$

As we have seen in Eq. (3.33) for the ΛCDM case, Eq. (4.57) have two solutions: a growing mode and a decaying mode, but we can assume that the decaying mode has had time to decrease to a negligible amplitude and using the definition of the growth factor D given in the previous Chapter we can write:

$$\delta(\vec{k},\eta) = \delta_0(\vec{k})D(\eta). \tag{4.59}$$

Thus we will refer to Eq. (4.57) as the (K-mouflage) linear growth factor equation from now on.
As in the ΛCDM case, the linear growth factor in K-mouflage is scale independent, in fact all the quantities that enter Eq. (4.57) are only time-dependent.
Comparing Eq. (4.57) with Eq. (3.31) we note that the differences between the two arises because of the two factors ϵ_1, ϵ_2 and because of the different behaviour of H and Ω_m.
The factor ϵ_1 arises from a fifth-force potential that enters the Euler equation and can be estimated like:

$$|\epsilon_1| = \left|\bar{A} - 1 + \frac{2\bar{A}\beta^2}{\bar{K}'}\right| \sim \left|\frac{\beta^2}{\bar{K}'}\right|, \tag{4.60}$$

as we have $\bar{A} \sim 1$. The sign of ϵ_1 cannot be determined a priori, because the terms $\bar{A} - 1 \simeq \beta\bar{\varphi}/M_{Pl}$ and $2\bar{A}\beta^2/\bar{K}'$ are of the opposite sign and of the same order.
The term ϵ_2 appears as a friction term in the Euler equation and is of the same order of ϵ_1, in fact:

$$\epsilon_2 = \frac{\mathrm{d}\ln\bar{A}}{\mathrm{d}\ln a} = \frac{\beta}{M_{Pl}}\frac{\mathrm{d}\bar{\varphi}}{\mathrm{d}\ln a} \sim -\frac{\beta^2}{\bar{K}'}. \tag{4.61}$$

The common dependence on the ratio $\beta^2/\bar{K}'$ has a precise meaning, indeed this quantity measures the deviation of the background evolution in K-mouflage from the ΛCDM scenario. Looking at the action (4.1), we see that the coupling between

the scalar field and the the matter only occurs through the function $A(\varphi)$. A small β means that this coupling function becomes independent on φ and almost equal to unity. Then the Jordan metric becomes identical to the Einstein metric and the matter no longer feels the scalar field which does not evolve.
On the other hand, a large K' means that the scalar field is sensitive to the non-linear part of the kinetic function $K(\chi)$. As we will show this gives rise to a mechanism that screens the effect of the scalar field and General Relativity is recovered. As we have shown in the previous Section $\dot{\bar{\varphi}}$ and $\bar{K}'$ diverge at early time, thus $\epsilon_1 \to 0$ and $\epsilon_2 \to 0$ and we recover the matter-dominated era as in ΛCDM.

4.4 Screening mechanism

We illustrate here the mechanism that allows to recover the General Relativity from the K-moulfage theory, in the case of sufficiently dense environments. For detailed treatment on this mechanism see [8] and [16].
For a simplified analysis we consider the static case, with zero temporal derivative. The Klein-Gordon equation (4.48) then reads:

$$\nabla \cdot (\nabla\varphi) K' = a^2 \frac{\beta \rho_m}{M_{Pl}}, \tag{4.62}$$

$$\chi = -\frac{1}{2\mathcal{M}^4}\frac{1}{a^2}(\nabla\varphi)^2, \tag{4.63}$$

where we have assumed $A \simeq 1$ and thus $\mathrm{d}A/\mathrm{d}\varphi \simeq \beta/M_{Pl}$.
Comparing Eq. (4.62) with the Poisson equation, we obtain:

$$K'\nabla\varphi = 2\beta M_{Pl}(\nabla\Psi_N + \nabla \times \vec{\omega}), \tag{4.64}$$

where $\vec{\omega}$ is a divergence-free potential vector (which must be determined along with φ). For some special cases, like e.g. that in which the matter distribution is spherically symmetric, $\vec{\omega}$ vanishes. Thus we can write the fifth force that appears on the right hand side of the Euler equation like:

$$\vec{F}_\varphi = -\frac{\beta}{M_{Pl}}\nabla\varphi = -\frac{2\beta^2}{K'}(\nabla\Psi_N + \nabla \times \vec{\omega}). \tag{4.65}$$

The K-mouflage screening mechanism relies on the fact that that in the non-linear regime the factor K' can be large, which suppresses the fifth force as compared with the Newtonian gravity $F_N = -\nabla\Psi_N$, with $|F_\varphi| \sim |F_N/K'|$. This is also true for the term $\nabla \times \vec{\omega}$ as it can be shown [16] that $\nabla \times \vec{\omega} \sim |F_N/K'|$.
Looking at Eq. (4.63) and for the models defined in Eq. (4.4)-(4.6) we see that requiring large K' is equivalent to put a condition on the gradient of the scalar field $\nabla\varphi$. Indeed it is possible to show that the suppression of the scalar field effect in dense environments due to K-mouflage is significant when the gradient of the scalar field satisfies [14]:

$$|\nabla\varphi| \gtrsim \mathcal{M}^2. \tag{4.66}$$

This translate into a condition on the Newtonian potential Ψ_N, from Eq. (4.64) we obtain:

$$|\nabla\Psi_N| \gtrsim \frac{\mathcal{M}^2}{2\beta M_{Pl}}. \tag{4.67}$$

For the Newtonian potential around a dense object of mass m, screening occurs inside the K-mouflage radius [16]:

$$R_K = \left(\frac{\beta m}{4\pi M_{Pl}\mathcal{M}^2}\right)^{\frac{1}{2}}. \tag{4.68}$$

For cosmological scales, screening appears when the wave number k characterizing a given structure satisfies:

$$k \lesssim 3\Omega_m^{(0)} A\beta \frac{H_0^2 M_{Pl}}{\mathcal{M}^2}\delta_m. \tag{4.69}$$

where δ_m is the matter density contrast. We can give an estimate of this scale considering that we must have $\mathcal{M}^4 \sim 3\Omega_\Lambda^{(0)} M_{Pl}^2 H_0^2$ in order to reproduce the observed cosmological constant energy density. Thus we obtain:

$$\frac{k}{H_0} \lesssim \sqrt{\frac{3}{\Omega_\Lambda^{(0)}}}\Omega_m^{(0)} A\beta\delta_m \tag{4.70}$$

The previous condition is associated to super-horizon scales, as a result all observable quasi-linear object in the Universe are unscreened in K-mouflage models. Therefore we expect linear scales of order the horizon scales to be maximally affected by the effect of modified gravity in K-mouflage models, and in particular the ISW effect should be significantly different from ΛCDM.

Chapter 5

K-mouflage analysis and results

In this Chapter we compare the predictions of different models of K-mouflage with those of ΛCDM and derive the behaviour of the growth factor in K-mouflage. We start illustrating the methods we adopt to achieve the solution for the background evolution of the Universe and for the growth of linear perturbations in K-mouflage, then we show and discuss our results.
In particular, the solution of the the growth factor Eq. (4.57) is necessary for our subsequent analysis, in order to compute the ISW-galaxy cross-correlation power spectrum in K-mouflage.
We chose three models of K-mouflage, one for each of the three different forms of the kinetic term defined in Eq. (4.4)- Eq.(4.6). The parameters which define each model are shown in Table (5.1), the reader can see that the three models differ only for the kinetic term, keeping the same coupling between the matter and scalar field.
The choice of the parameters which defines each model is the same of [14] [15], in order to compare directly our results and check their consistency. For the same reason, throughout this Chapter we adopt the Planck 2013 cosmological parameters, shown in the second column of Table 2.1.

Table 5.1 Definition of K-mouflage models that we adopted in our analysis. In the second column we define the form of the kinetic function (χ), in the third column we report the coupling function A, the last three columns fix the value of the parameters : β, m, K_0.

	Kinetic term	Coupling function	β	m	K_0
Model 1	$-1+\chi+K_0\chi^m$	$A=e^{\beta\varphi\sqrt{8\pi G}}$	0.3	3	1
Model 2	$-1+\chi+K_0\chi^m$	$A=e^{\beta\varphi\sqrt{8\pi G}}$	0.3	3	-5
Model 3	$-1+\chi-\chi^2+\chi^3/4$	$A=e^{\beta\varphi\sqrt{8\pi G}}$	0.3	-	-

5.1 Numerical implementation

In order to solve the equation for the linear growth factor in K-mouflage Eq. (4.57), it is necessary to know the behaviour of its time-dependent coefficients. More precisely the evolution equation for D, is coupled to the evolution equations

for the background quantities. Thus one has to solve a closed system of coupled ordinary differential equations (ODEs system).
An analytic solution to this problem is known in the case of a flat matter-dominated Universe (Eistein De-Sitter model), as we have shown in Chapter 2. Unfortunately, simply adding the contribution of a cosmological constant to the matter fluid, makes it impossible to find a true analytic solution for the growth factor, though good approximated formulas are available. In the case of K-mouflage the only feasible way is to proceed numerically.

5.1.1 Numerical methods for ODEs

Consider a so called *Initial Value Problem* (IVP) of the form:

$$y'(t) = f(t, y(t)),\ y(t_0) = y_0, \tag{5.1}$$

where f is a function that maps $[t_0, \infty) \times \mathbb{R}^d$ to $\mathbb{R}^d$, and the initial condition $y_0 \in \mathbb{R}^d$. Note that only the first derivative of y appears in the equation, so that this is a system of first order ODEs. Without loss of generality, a higher-order ODE can be converted into a larger system of first-order equations by introducing extra variables, thus Eq. (5.1) represents the most general case of IVP.
Assume we want to know the solution $y(t)$ of Eq. (5.1) in a certain interval $[t_0, T]$; it is rarely possible to succeed using symbolic computation, in most physical cases the problem requires a numerical approach.
In this subsection we give brief review about the algorithms implemented to solve IVPs, which we used for our purpose.
The use of a numerical method, requires to sample continuous variables with a finite number of points, thus let $h = (T - t_0)/N$ be the time step, for some large integer N. The goal of a numerical integrator for ODE is to determine values that approximate the true solution at each $t_i = t_0 + ih$, it is important to note that h can in principle vary along the interval.
These algorithms are based on two different schemes: explicit or implicit. Explicit methods calculate the state of a system at a later time t_{i+1} from the state of the system at the current time t_i, while implicit methods find a solution by solving an equation involving both the current state of the system and the later one.
As an illustrative example we show the two basic algorithms for ODEs: the direct Euler method and the backward Euler method. The Euler method reconstructs the solution $y(t)$ by approximating the curve at each step with its first-order Taylor expansion; starting from a certain point of the solution curve, the subsequent point is found by moving a short distance along a line tangent to that curve. Formally the approximation consists in replacing the derivative y' with the finite difference:

$$y'(t) \approx \frac{y(t+h) - y(t)}{h}, \tag{5.2}$$

which can be applied to Eq. (5.1), to give:

$$y(t+h) \approx y(t) + hy'(t) = y(t) + hf(t, y(t))). \tag{5.3}$$

Now the numerical estimate of the exact solution at the step $i+1$ based the on the Euler method, can be simply written as:

$$y_{i+1} = y_i + hf(t_i, y_i). \tag{5.4}$$

The solution at the point $i+1$ is given explicitly in terms of the value of the solution at the previous point and its derivative.
If, instead of Eq. (5.2), we use the approximation:

$$y'(t) \approx \frac{y(t) - y(t-h)}{h}, \tag{5.5}$$

we get the backward Euler method:

$$y_{i+1} = y_i + hf(t_{i+1}, y_{i+1}). \tag{5.6}$$

The backward Euler method is an implicit method, meaning that we have to solve an equation to find y_{i+1}.
Despite on its simplicity, the Euler method is too much inaccurate for practical applications. This is due to the fact that the Euler method is a single-step method i.e. it uses only the informations about the solution at the current step to approximate the solution at the next step.
To improve the efficiency of a method, more informations have to be used to construct the solution. Two kind of approaches can be used. Methods of the Runge–Kutta family, take some intermediate steps (for example, a half-step) to obtain a higher order method, but then discard all previous information before taking a second step. The most widely known member of the Runge–Kutta family is the 4-th-Order Runge-Kutta method, which starting from a certain y_i uses the follow algorithm to get y_{i+1}:

$$\begin{aligned} K_1 &= f(t_i, y_i) \\ K_2 &= f(t_i + \tfrac{h}{2}, y_i + \tfrac{h}{2}K_1) \\ K_3 &= f(t_i + \tfrac{h}{2}, y_i + \tfrac{h}{2}K_2) \\ K_4 &= f(t_i + h, y_i + hK_3) \\ y_{i+1} &= y_i + \tfrac{h}{6}(K_1 + 2K_2 + 2K_3 + K_4). \end{aligned} \tag{5.7}$$

It can be shown [Wikipedia] that for this method the cumulative error at each step is order $O(h^4)$, while for the Euler method the cumulative error is order $O(h)$.
The method in Eq. (5.7) can be generalized to get higher order ones.
The other class of numerical methods for ODE is represented by multistep methods. This kind of methods attempt to gain efficiency by keeping and using the information from previous steps rather than discarding it. Consequently, multistep methods refer to several previous points and derivative values.
In the case of linear multistep methods, a linear combination of the previous points and derivative values is used. Given s, the number of previous points that the method uses to calculate the current solution y_{i+s}, we can write a linear multistep method in the general form:

$$\begin{aligned} &y_{i+s} + a_{s-1}y_{i+s-1} + a_{s-2}y_{i+s-2} + \cdots + a_0 y_i = \\ &\quad = h \cdot (b_s \cdot f(t_{i+s}, y_{i+s}) + b_{s-1} \cdot f(t_{i+s-1}, y_{i+s-1}) + \cdots + b_0 \cdot f(t_i, y_i)). \end{aligned} \tag{5.8}$$

The coefficients $a_0, \ldots, a_{s-1}$ and $b_0, \ldots, b_s$ determine the method. On this base the requests $a_{s-1} = -1$ and $a_{s-2} = \cdots = a_0 = 0$, define the subclass of Adams methods. Adams methods can be implicit (Adams-Moulton) or explicit (Adams-Bashforth), the b coefficients are chosen are chosen such that the methods has order s and this choice determines the method uniquely.
Trying to solve an IVP with one of the algorithms just described, could anyway be

difficult in some cases. The most known numerical instability which affects ODEs problems is called *stiffness*. The problem of *stiffness* manifests when a numerical algorithm is forced to use in a certain interval of integration a step-length (h), which is excessively small in relation to the smoothness of the exact solution in that interval.
To treat stiff ODEs it is convenient using an other sub-class of linear multistep methods: the Backward Differentiation Formula (BDF). BDF are implicit methods which can be characterized by taking $b_{s-1} = \cdots = b_0 = 0$ in Eq.(5.8).
The phenomenon of numerical instability is not a property of the exact solution of an IVP, rather it is related with the form of the differential system itself and with the algorithm that we choose for the solution.

5.1.2 IVP definition and stability tests

We have written several `Python` scripts. Each one solves a closed system of differential equations to get the evolution of the scale factor, of the scalar field and of the growth factor in K-mouflage, for the models defined in Table (5.1).
We spent a considerable amount of effort to test the numerical stability of our results as much as their internal consistency.
In order to test the numerical stability of the system, we decided to implement different numerical integrators and compare their results. The functions *ode* and *odeint* of `Python` provide the following numerical integrators:

- *"lsoda"* is based on implicit Adams method for non-stiff problems but can switch automatically to a method based on backward differentiation formulas (BDF) in case the problem is stiff. It is part of ODEPACK, a collection of Fortran solvers for IVPs, and it was written by Petzold and Hindmarsh. [5]

- *"vode"* it provides variable-coefficient Adams-Moulton method for non-stiff problems or a BDF in case the problem is stiff, it was developed by Brown, Byrne, and Hindmarsh subsequently to *"lsoda"* [44].

- *"dopri5"* and *"dop853"* which provide explicit Runge-Kutta methods respectively of order (4)5 and 8(5,3) due to Dormand and Prince [44].

All these integrators have been tested in our scripts; the results showed very good agreement, with relative differences in the solution less than 10^{-6}.
Implementing one of these alghorithms, requires the precise definition of a closed system of differential equations with the corresponding initial conditions. The coupled evolution equations to be solved are: the Friedmann equation (4.20) and Eq. (4.21)), the Klein-Gordon equation (4.25) and the growth factor equation (4.57), that were written in the previous Chapter in terms of the cosmic time t .
To close the system, also the definitions of K and A must be added, since they determine unambiguously the model of K-mouflage.
In order to further verify our numerical results , we compared those obtained from differential systems of different form but with the same analytical solution.
To change the form of an ODE's system while preserving the solution, one can in principle change the independent variable or replace some equation with an equivalent one.
We considered four different temporal variables, such as: the proper time t, the scale factor a, the redshift $z = \frac{1}{a} - 1$ and the number of e-folds $\mathcal{N} \equiv \log \frac{a}{a_0}$. Note

that the relation between a and t is given by the Friedmann equation, while the other quantities can be trivially expressed in terms of a.
To write our system in terms of each variable, we have suitably transformed the derivatives using a generalization of the chain rule to any order of derivation, namely the Faà di Bruno's formula. In particular we made use of the following relations, assuming that $y = f(u)$ and $u = g(x)$:

$$\frac{\mathrm{d}y}{\mathrm{d}x} = \frac{\mathrm{d}y}{\mathrm{d}u}\frac{\mathrm{d}u}{\mathrm{d}x} \tag{5.9}$$

$$\frac{\mathrm{d}^2y}{\mathrm{d}x^2} = \frac{\mathrm{d}^2y}{\mathrm{d}u^2}\left(\frac{\mathrm{d}u}{\mathrm{d}x}\right)^2 + \frac{\mathrm{d}y}{\mathrm{d}u}\frac{\mathrm{d}^2u}{\mathrm{d}x^2}. \tag{5.10}$$

Applying the transformation rules Eq. (5.9) and (5.10), we can write Eq. (4.21)), Eq. (4.19), Eq. (4.25) and Eq. (4.57), in terms of the variables t, a, $\mathcal{N}$, z:

$$\begin{cases} \dfrac{\mathrm{d}H}{\mathrm{d}t} = -4\pi G(\rho_m + \rho_\varphi^{eff} + p_\phi) \\ \dfrac{\mathrm{d}\rho_\varphi^{eff}}{\mathrm{d}t} = -3H(\bar{\rho}_\varphi^{eff} + \bar{p}_\varphi) \\ \dfrac{\mathrm{d}^2\varphi}{\mathrm{d}t^2} = -\dfrac{3HK'\frac{\mathrm{d}\varphi}{\mathrm{d}t} + \frac{\mathrm{d}A}{\mathrm{d}\varphi}\rho_m}{K' + (\frac{\mathrm{d}\varphi}{\mathrm{d}t})^2\frac{K''}{\mathcal{M}^4}} \\ \dfrac{\mathrm{d}^2D}{\mathrm{d}t^2} = -H(2+\epsilon_2)\dfrac{\mathrm{d}D}{\mathrm{d}t} + \dfrac{3}{2}H^2\Omega_m(1+\epsilon_1)D \end{cases} \tag{5.11}$$

$$\begin{cases} \dfrac{\mathrm{d}H}{\mathrm{d}a} = -\dfrac{4\pi G}{aH}(\rho_m + \rho_\varphi^{eff} + p_\phi) \\ \dfrac{\mathrm{d}\rho_\varphi^{eff}}{\mathrm{d}a} = -\dfrac{3}{a}(\rho_\varphi^{eff} + p_\phi) \\ \dfrac{\mathrm{d}^2\varphi}{\mathrm{d}a^2} = -\dfrac{3aH^2K'\frac{\mathrm{d}\varphi}{\mathrm{d}a} + \frac{\mathrm{d}A}{\mathrm{d}\varphi}\rho_m}{K'a^2H^2 + (\frac{\mathrm{d}\varphi}{\mathrm{d}a})^2a^4K''\frac{H^4}{\mathcal{M}^4}} - \dfrac{\mathrm{d}\varphi}{\mathrm{d}a}\left(\dfrac{1}{a} + \dfrac{1}{H}\dfrac{\mathrm{d}H}{\mathrm{d}a}\right) \\ \dfrac{\mathrm{d}^2D}{\mathrm{d}a^2} = -\dfrac{1}{a}\left(\dfrac{a}{H}\dfrac{\mathrm{d}H}{\mathrm{d}a} + 3 + \epsilon_2\right)\dfrac{\mathrm{d}D}{\mathrm{d}a} + \dfrac{3D\Omega_m(1+\epsilon_1)}{2a^2} \end{cases} \tag{5.12}$$

$$\begin{cases} \dfrac{\mathrm{d}H}{\mathrm{d}\mathcal{N}} = -\dfrac{4\pi G}{H}(\rho_m + \rho_\varphi^{eff} + p_\phi) \\ \dfrac{\mathrm{d}\rho_\varphi^{eff}}{\mathrm{d}\mathcal{N}} = -3(\rho_\varphi^{eff} + p_\phi) \\ \dfrac{\mathrm{d}^2\varphi}{\mathrm{d}\mathcal{N}^2} = -\dfrac{3H^2K'\frac{\mathrm{d}\varphi}{\mathrm{d}\mathcal{N}} + \rho_m\frac{\mathrm{d}A}{\mathrm{d}\varphi}}{K'H^2 + (\frac{\mathrm{d}\varphi}{\mathrm{d}\mathcal{N}})^2K''\frac{H^4}{\mathcal{M}^4}} - \dfrac{1}{H}\dfrac{\mathrm{d}\varphi}{\mathrm{d}\mathcal{N}}\dfrac{\mathrm{d}H}{\mathrm{d}\mathcal{N}} \\ \dfrac{\mathrm{d}^2D}{\mathrm{d}\mathcal{N}^2} = -\left(\dfrac{1}{H}\dfrac{\mathrm{d}H}{\mathrm{d}\mathcal{N}} + 2 + \epsilon_2\right)\dfrac{\mathrm{d}D}{\mathrm{d}\mathcal{N}} + \dfrac{3}{2}D\Omega_m(1+\epsilon_1). \end{cases} \tag{5.13}$$

$$\begin{cases} \dfrac{\mathrm{d}H}{\mathrm{d}z} = \dfrac{4\pi G}{H(1+z)}(\rho_m + \rho_\varphi^{eff} + p_\phi) \\ \dfrac{\mathrm{d}\rho_\varphi^{eff}}{\mathrm{d}z} = \dfrac{3}{1+z}(\rho_\varphi^{eff} + p_\phi) \\ \dfrac{\mathrm{d}^2\varphi}{\mathrm{d}z^2} = \dfrac{3H^2(1+z)K'\frac{\mathrm{d}\varphi}{\mathrm{d}a} - \rho_m\frac{\mathrm{d}A}{\mathrm{d}\varphi}}{K'(1+z)^2H^2 + (\frac{\mathrm{d}\varphi}{\mathrm{d}z})^2(1+z)^4K''\frac{H^4}{\mathcal{M}^4}} - \dfrac{\mathrm{d}\varphi}{\mathrm{d}z}\left(\dfrac{1}{1+z} + \dfrac{1}{H}\dfrac{\mathrm{d}H}{\mathrm{d}z}\right) \\ \dfrac{\mathrm{d}^2D}{\mathrm{d}z^2} = -\dfrac{1}{1+z}\left(\dfrac{1+z}{H}\dfrac{\mathrm{d}H}{\mathrm{d}z} - (1+\epsilon_2)\right)\dfrac{\mathrm{d}D}{\mathrm{d}z} + \dfrac{3D\Omega_m(1+\epsilon_1)}{2(1+z)^2} \end{cases} \tag{5.14}$$

where we have dropped the over bar on the variables for simplicity, as it is clear that we are dealing with background quantities.
These equations are actually superabundant, in fact the first two lines of each system are not independent. The Friedmann equation for $\dot{H}$ can be safely replaced with the continuity equation (4.19) for the scalar field density with a little forethought. This is possible considering that the evolution of the (pressureless) matter density is given by: $\rho_m = \rho_{m,0}/a^3$, and that the solution for H in terms of ρ_m and ρ_φ^{eff} is already given by the first Friedmann equation (4.20).
This is an example of how two different equations, that add the same information to the system, can be exchanged to modify the form of the ODEs system, without altering the solution in principle. We tried different configurations of independent equations and different temporal variables, in order to check the self-consistency and numerical stability of our method. All these tests have produced positive results , indeed we got excellent agreement in the various solutions.
Once the ODE's system is built, the other ingredient necessary to formulate our IVP is the set of initial conditions. If we start the computation sufficiently far in the past, deep in the matter dominated era, all the quantities defined in K-mouflage, for which we have an analogous in ΛCDM (e.g. H, a, D), must converge to the same behaviour as in ΛCDM. For the variable directly related to the scalar field in K-mouflage, we used the early time limits derived in Sec. (4.2.1).
Therefore considering the independent variable a, and given a certain initial value a_i, we can write the set of initial conditions:

$$H_i = \Omega_m^{(0)} a_i^{-3} \tag{5.15}$$

$$D_i = a_i \tag{5.16}$$

$$\left.\frac{\mathrm{d}D}{\mathrm{d}a}\right|_{a=a_i} = 1 \tag{5.17}$$

$$\left.\frac{\mathrm{d}\varphi}{\mathrm{d}a}\right|_{a=a_i} = -\operatorname{sgn}(K_0)\left(\frac{2\beta\rho_m^{(0)}(2\mathcal{M}^4)^{m-1}}{3mM_{Pl}a_i^3|K_0|H_i^{2m}}\right)^{\frac{1}{2m-1}}(a_i)^{-1} \tag{5.18}$$

$$\varphi(a_i) = -\operatorname{sgn}(K_0)\frac{2m-1}{3m-3}\left(\frac{2\beta\rho_m^{(0)}(2\mathcal{M}^4)^{m-1}}{3mM_{Pl}a_i^3|K_0|H_i^{2m}}\right)^{\frac{1}{2m-1}} \tag{5.19}$$

$$\rho_\varphi(a_i) = -\frac{2m-1}{m-1}\mathcal{M}^4K_0\left(\frac{a_iH_i\frac{\mathrm{d}\varphi}{\mathrm{d}a}|_{a=a_i}}{\sqrt{\mathcal{M}^4}}\right)^{2m} \tag{5.20}$$

where the first three equations represents the exact solution of ΛCDM in pure

matter domination, whereas the last three as been obtained taking the early time limit (small a) of the Klein-Gordon equation (4.35) written in terms of a. We stress that analogous initial condition can be found for any independent variable that we used, by applying the appropriate transformation rule.

5.1.3 Description of the programs

As already stated, we developed several `Python` scripts for the computation of the background dynamics and the linear growth factor of a given model of K-mouflage. We provide here a general description of these codes.
First we define the input parameters: H_0, $\rho_m^{(0)}$, β, m, K_0, $\mathcal{M}^4$ and the temporal vector. The K-mouflage parameters (β , m, K_0) are given in Table (5.1) for each model we considered. For the energy scale of the scalar field $\mathcal{M}^4$, we initially assumed a random value of order the present energy density of the Universe, then we tuned iteratively, running the code several times, in order to reproduce the exact density of matter and dark energy at the present time. Indeed $\mathcal{M}^4$ is an eigenvalue of the problem rather than a free parameter. We also assumed an exactly flat Universe without radiation, so that only matter and dark energy contribute to the total density which is equal to the critical density.
Given the input parameters and the discretized temporal variable, we define a function that returns the first derivative of each variable of the ODE system we want to solve.
After that, the code extrapolates the initial conditions by evaluating Eq. (5.15)-(5.20) at a certain instant, which correspond to the initial value of the independent variable vector.
The initial value of the temporal variable was fixed at $z_i = 100$ or $a_i = 1/99$; however we verified that changing the initial instant (e.g. the initial $t, a, z, \mathcal{N}$) does not alter our final results, provided that it is deep enough in the matter era ($z_0 > 10$).
Finally we call the function *odeint* that takes in input the time vector, the ODEs system and the initial conditions and returns the discretized solution in terms of output vectors.

5.2 Results for background evolution

In this section we show our results for the evolution with redshift of the background cosmological parameters and of the Hubble expansion rate, comparing the results for the models in Table (5.1) with the reference Λ CDM model.
Since we normalize the density and dark-energy parameters to be equal to the ones observed today, all models coincide at $z = 0$.
We first consider the density parameters, in Fig. (5.1) we show the evolution of Ω_m and Ω_{DE} for the three models of Table (5.1) and the ΛCDM. We notice that for Model 2 and for the ΛCDM the dark energy density is positive at all z, thus Ω_m remains less than 1 as we assume a flat Universe. Contrariwise Model 1 and Model 3 show a negative scalar field energy density for high redshift, this implies a matter density parameter Ω_m that is grater than unity far in the past and an equation of state ω_φ that diverges when $\Omega_\varphi = \Omega_{DE} = 0$, in agreement with our discussion of Section (4.2). We see that for all the models, the scalar field density matches the matter density at a low redshift $z \sim 0.4$
In Figure (5.2) we plot the equation of state parameter ω_φ. As explained in the

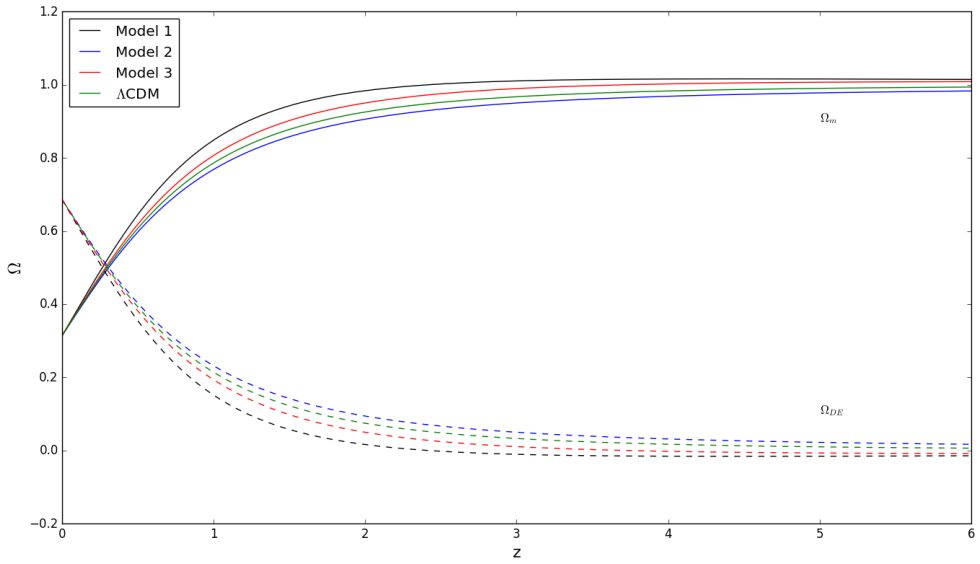

Figure 5.1: Density parameter of matter and dark energy for the K-mouflage models defined in Table (5.1) and for the ΛCDM (in K-mouflage $Omega_\varphi = \Omega_{DE}$ in ΛCDM $Omega_\Lambda = \Omega_{DE}$).

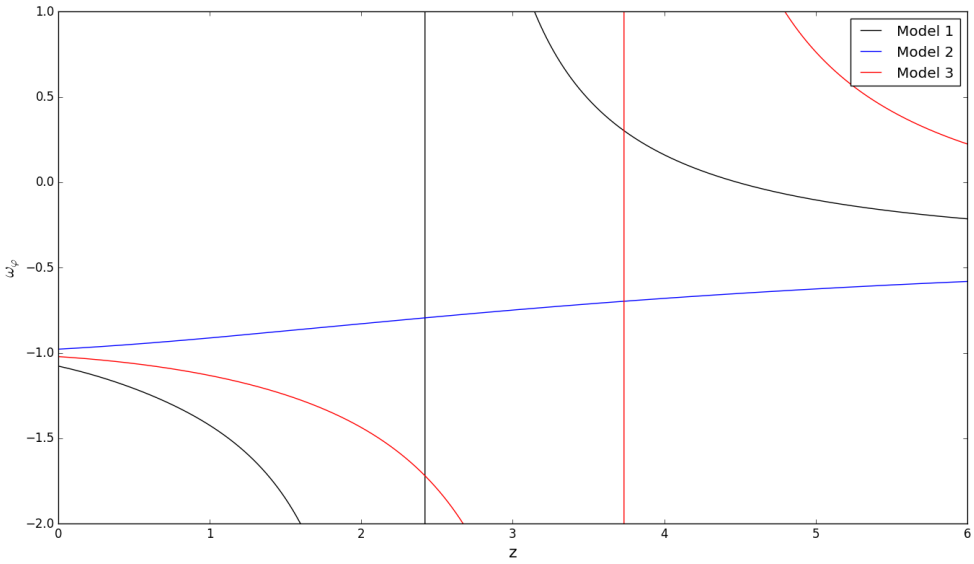

Figure 5.2: Equation of state parameter ω_φ for the models defined in Table (5.1).

previous Chapter, for models with positive kinetic function K at high redshift, ρ_φ^{eff} must change sign and ω_φ must diverge. For Model 1 and Model 3 this happens at $2 < z_{*,1} < 3$ and $3 < z_{*,3} < 4$ respectively, in correspondence of the vertical lines of Fig (5.2).
In Model 2, contrary to the other cases, the equation of state remains always negative and smoothly runs from $-(m-1)/(2m-1)$ to -1 at low redshifts. This means that models with $K_0 < 0$ are closer to the ΛCDM scenario with respect to such background quantity, because ω_φ does not go very far from -1.
Comparing Fig. (5.1) and Fig. (5.2), we see that when the scalar field starts to dominate (after $z \sim 0.4$) ω_φ^{eff} is sufficiently next to -1 for all the models, thus to reproduce a cosmological constant dynamics. At high redshift ω_φ converges to $-(m-1)/(2m-1) = -0.4$ for $m = 3$, independently of other parameters, as

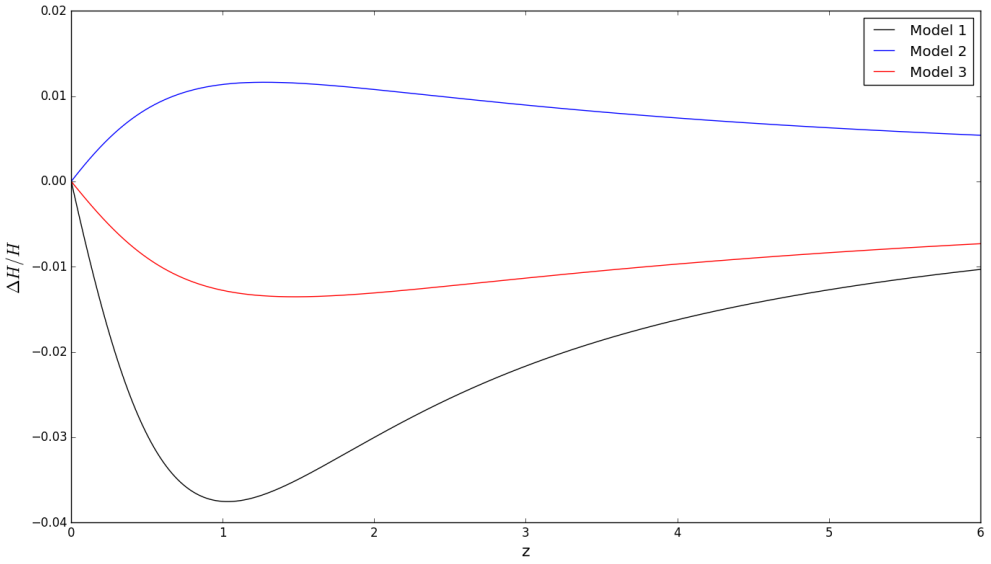

Figure 5.3: Relative deviation $[H(z) - H_{\Lambda CDM}(z)]/H_{\Lambda CDM}(z)$ of the Hubble expansion rate with respect to the ΛCDM reference. We consider the same models as in Table (5.1).

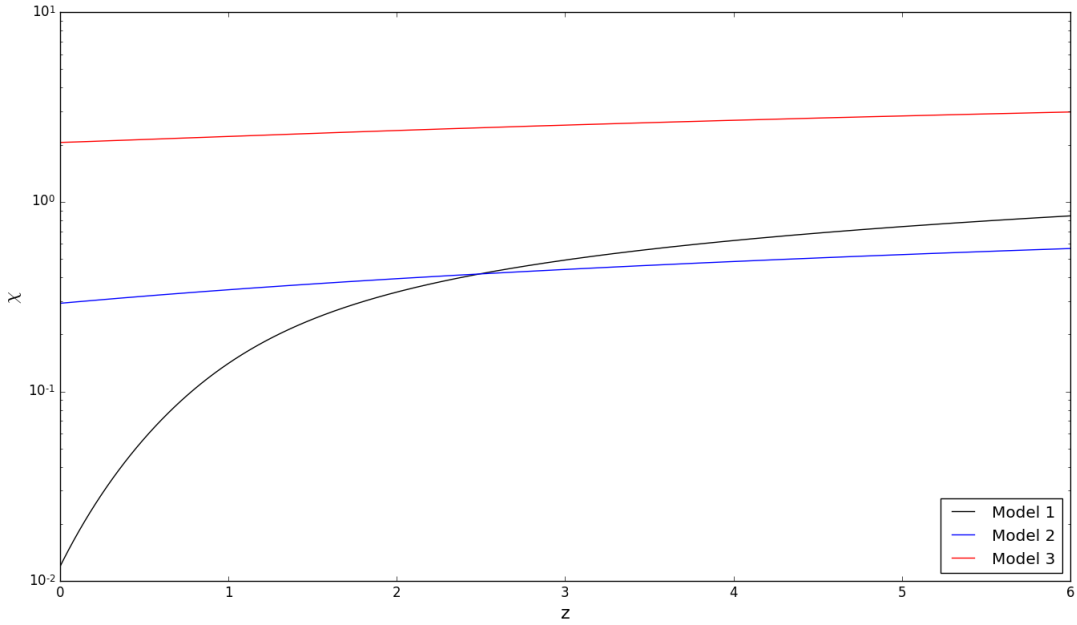

Figure 5.4: Scalar field time-derivative term $\bar{\chi} = \frac{1}{2\mathcal{M}^4}\left(\frac{\partial\varphi}{\partial t}\right)^2$ for the same models as in Table (5.1).

predicted by the early time behaviour Eq. (4.32).
In Figure (5.3) we report the deviation of the Hubble expansion parameter of the three models, with respect to ΛCDM. For models that have negative ω_φ^{eff} at high z, the Hubble expansion rate is reduced, in agreement with the Friedmann equation (4.20). In contrast, if ω_φ^{eff} is positive at high z and grows with redshift (whereas in the ΛCDM scenario ρ_Λ), then the Hubble expansion rate is enhanced. Thus Model 1 and Model 3 show negative deviation from ΛCDM, while for Model 2 the parameter H is higher than in ΛCDM. Comparing Fig. (5.1) and Fig. (5.3) we note the direct correspondence between a lower Ω_{DE} and a lower H.

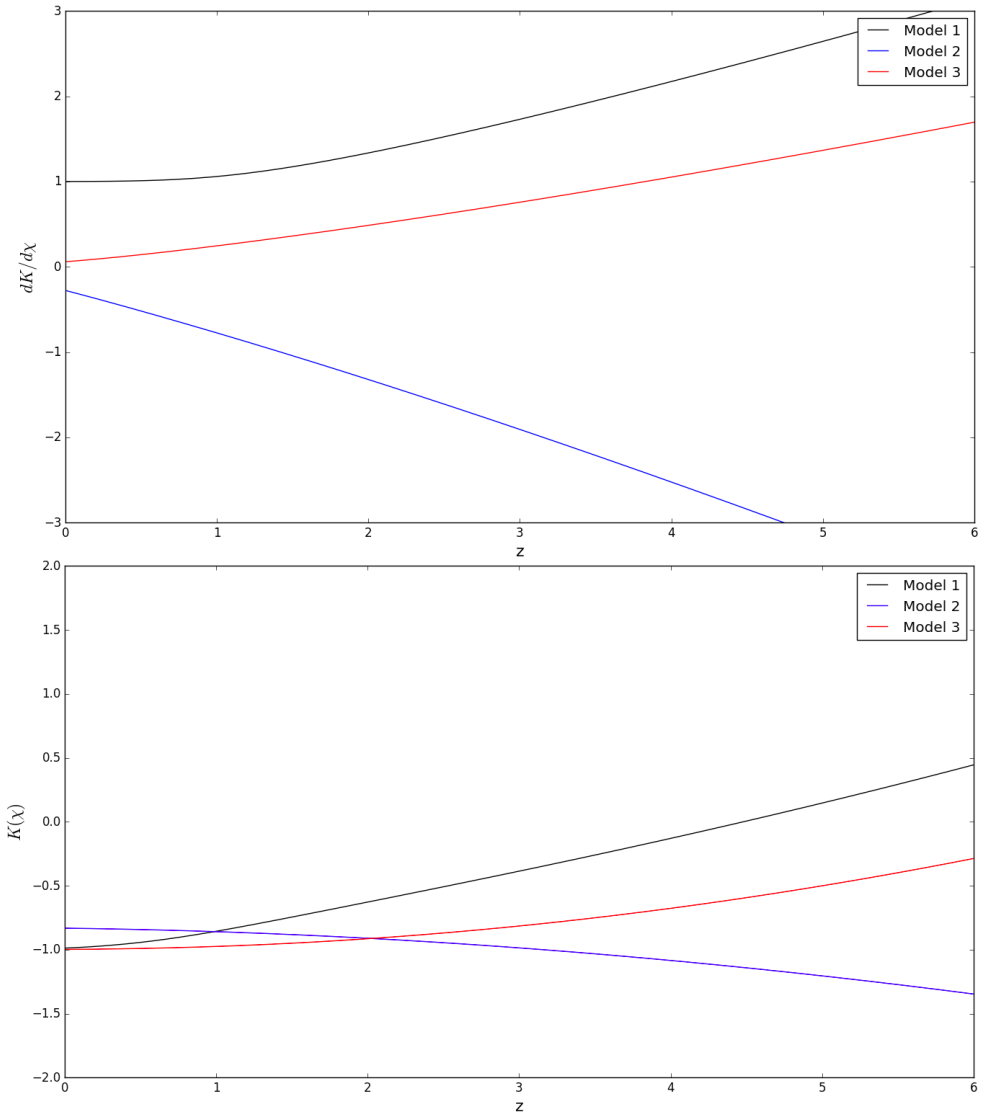

Figure 5.5: **Upper panel:** Evolution with redshift of the Kinetic function $K(z)$ for the models in Table (5.1).
Lower panel: Evolution with redshift of the first derivative of the Kinetic function $\mathrm{d}K(z)/\mathrm{d}\chi$ for the models in Table (5.1).

We display the scalar field time-derivative term $\bar{\chi} = \dot{\bar{\varphi}}/(2\mathcal{M}^4)$ in Fig (5.4). We see that for Model 1 $\bar{\chi}$ converges to 0 at late times as required by the the infinite time limit of the Klein-Gordon equation (4.37). For this quantity Model 2 and Model 3 show similar results, due to the fact that the kinetic function Eq. (4.5) and Eq. (4.6) admit a critical value χ_* where $K'(\chi_*) = 0$. Thus for Model 3 χ converges to the non-zero value $\chi_* = 2$ given by Eq. (4.8), while for Model 2 we have from Eq. (4.7) $\chi \to \chi_* \simeq 0.26$ as t increases and z decreases, these trends are visible in Fig. (5.4).
Figure (5.5) displays the evolution of the kinetic function $K(\chi)$ and of its first derivative $K' = \mathrm{d}K/\mathrm{d}\chi$. As shown in Fig. (5.5) lower panel, K' converges to 1 from above at low redshift in Model 1, as χ converges to zero. Whereas Model 2 and Model 3 are characterized by a K' that crosses the zero for some χ_*. Thus, according to the discussion of Sec. (4.2.2) and in agreement with the results for χ

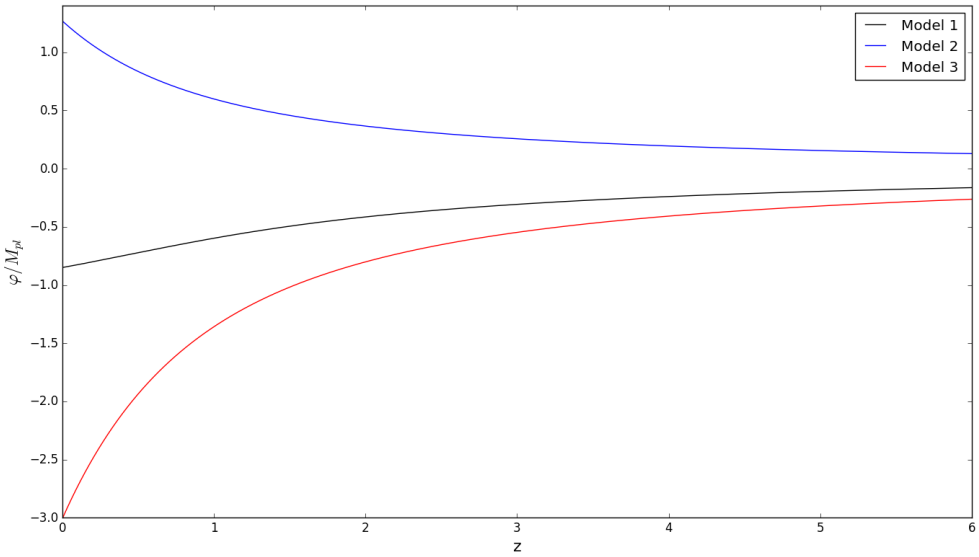

Figure 5.6: Normalized scalar field φ/M_{Pl} for for the three models defined in Table (5.1).

shown in Fig. (5.4), we see that for Model 3 K' converge to zero from positive values at low redshift, while Model 2 has a negative K' converging to zero at low redshift.
Looking at the early time limit given by Eq. (4.32), we deduce that there is a correspondence between a positive K' and a negative ρ_φ^{eff} at high redshift and vice versa. The comparison of Fig. ((5.5)) with Fig. (5.1) and Fig. (5.3) confirms this result: models with $K' < 0$ have negative Ω_φ and their Hubble expansion rate is reduced with respect to ΛCDM; whereas for scenarios with $K' > 0$ the scalar field density ρ_φ^{eff} and the parameter Ω_φ are always positive and this leads to a greater Hubble rate $H(z)$.
The kinetic function of Model 1 converges to -1 at low z, as shown in the upper panel of Fig. (5.5), as to recover the cosmological constant regime at late time (see our discussion in Sec. (4.2.2) and see Eq. (4.38)). The kinetic function of Model 3, also converges to -1 at late time, because for this model we have $K(\chi_*) = K(2) = -1$. The kinetic function of Model 2 converges to a value $K(\chi_*) \simeq -0.82$ as clearly shown in Fig (5.5).
In Fig. (5.6) we report our results for the normalized scalar field φ/M_{Pl}. While at high redshift (i.e. early times) φ goes to zero for all the three models, the behaviours are different at late times. The scalar field in Model 1 converges to a negative constant at low z, as seen in Eq. (4.38). Whereas for Model 2 and Model 3, φ keeps growing (in Model 2) or decreases (in Model 3) linearly with time in agreement with Eq. (4.39) and Eq. (4.40). The sign of φ is opposite to the one of K'.
We conclude this Section underling that all our results for the evolution of the background quantities for all scenarios of K-mouflage we tested, are in perfect agreement with those of [14].

5.3 Results for the growth factor

In this Section we report our results for the quantities related to the growth factor equation (4.57) that we have derived in the previous chapter. This results

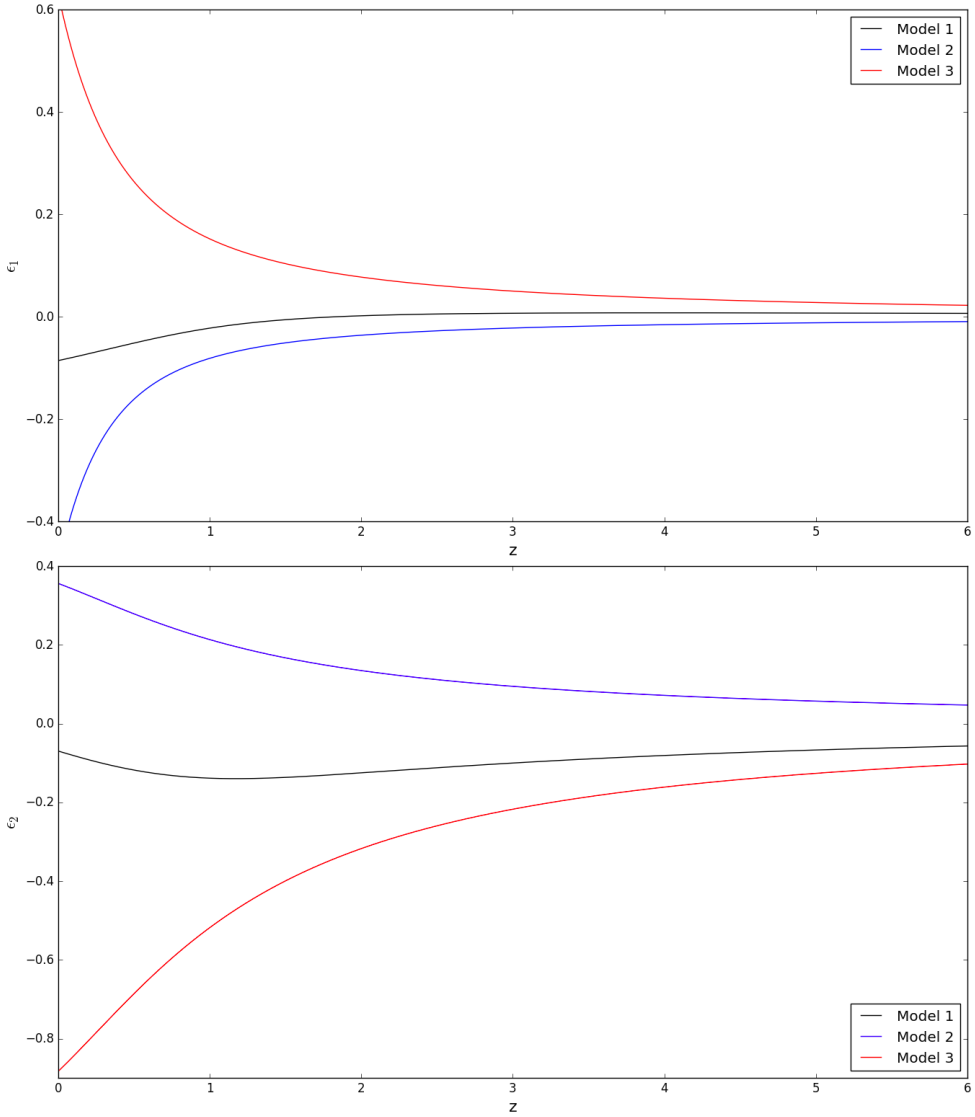

Figure 5.7: **Upper panel:** factor ϵ_1 defined in Eq. (4.58) for the Model 1, Model 2, Model 3 with parameter defined in Table (5.1).
Lower panel: factor ϵ_2 for the same models.

constitute a fundamental pieces of our analysis, in fact the growth factor and its first derivative enter the integral which allow to compute the ISW-galaxy cross-correlation power spectrum, as we discussed in Chapter 3.

We start from the plots of the coefficients ϵ_1 and $_2$ defined by Eq. (4.58), that modify the form of the growth factor equation with respect to that derived in ΛCDM. The factor ϵ_1 is shown in the upper panel of Fig. (5.7) while ϵ_2 is shown in the lower panel Fig. (4.58), again the various curves refer to the models of K-mouflage defined in Table (5.1). At high redshifts both ϵ_1 and ϵ_2 go to zero, as $\bar{\varphi} \to 0$ and $|K'| \to \infty$, but it appears that the convergence to zero is faster for ϵ_1. The low z behaviour can be understood deriving the late time limit of ϵ_1 and ϵ_2, from the theory developed in Sec (4.2.2). For Model 1, considering the results

given by Eq. (4.38) we find that during the cosmological constant regime:

$$\epsilon_2 \sim \frac{a^{-2}}{\dot{a}} \sim \exp\left(\frac{\mathcal{M}^2 t}{\sqrt{3}M_{Pl}}\right),$$

while ϵ_1 converges to a constant value along with $\bar{\varphi}$ and $\bar{A}$.
For Model 2 and Model 3 we consider Eq. (4.39) and Eq. (4.40). In these scenarios $\bar{\varphi}$ keeps increasing linearly with time while $\bar{K}'$ goes to zero, thus ϵ_1 goes to infinity at an exponential rate while ϵ_2 converges to a finite value.
The coefficient ϵ_2 is positive, along with $\bar{\varphi}$ for Model 2 where $\bar{K}' < 0$, and negative for Model 1 and Model 3 where $\bar{K}' > 0$.
We note that for Model 1 the deviations from zero of the coefficients ϵ_1 and ϵ_2 are of the same order of magnitude as the deviations from ΛCDM of the background quantities e.g the Hubble rate $H(z)$. For Model 2 and Model 3, the deviations from ΛCDM are amplified, due to the different late time dynamics. Thus we expect the growth factor $D(z)$ in Model 2 and Model 3 to show more consistent deviations from the ΛCDM solution than the growth factor in Model 1.
In Figure (5.8) we display our results for the linear growth factor D and for the parameter $f(z)$ defined in Eq. (**??**). As for the Hubble expansion rate (see Fig. (5.3)), the sign of the deviation of D from the ΛCDM is determined by the sign of $\bar{K}'$ for the various models. However, while in the case of the Hubble rate a positive $\bar{K}'$ yields a smaller $H(z)$, scenarios with $\bar{K}' > 0$ show an enhanced growth factor $D(z)$ with respect to the ΛCDM. Thus, in our case Model 1 and Model 3, which both have $\bar{K}' > 0$, yield a smaller $H(z)$ (when we require a common normalization today) and a larger linear growth factor $D(z)$, as well as a larger $f(z)$ at high redshift as we can see in Fig. (5.8), while opposite deviations are obtained for the Model 2 where $\bar{K}' < 0$. We can conclude that a positive $\bar{K}'$ (resp. a negative $\bar{K}'$) yields a faster (resp. slower) growth of large-scale structures at the linear level.
We note that deviations from ΛCDM of $D(z)$ and $f(z)$ are of the same order of the coefficients ϵ and somewhat grater than those of the background quantity H. On the other hand the background parameter like H or Ω are constrained to be equal to the ΛCDM reference values today.
Since there is a substantial deviation of the growth factor (and its derivative) between K-mouflage models and ΛCDM, at both low and high redshift, we expect the emergence of a significantly different ISW signal in this kind of models. As we have outlined in Chapter 3, cross-correlation between galaxy distribution and CMB anisotropies constitute a probe sensitive to the features of the linear growth rate of cosmic structure, thus they can be successfully used to constraint K-mouflage models.
In the next Chapter, we will deepen the ISW-galaxy correlation in K-mouflage, with this aim we introduce here another fundamental quantity for this analysis, that is the growing mode of the gravitational potential Ψ_N. In ΛCDM the growing mode of the gravitational potential is related to the growth factor by Eq. (3.32); in K-mouflage, starting from the modified Poisson equation (4.53), we can we can write the linear growing mode D_{Ψ_N} of the gravitational potential as:

$$D_{\Psi_N} = \bar{A}\frac{D}{a}. \tag{5.21}$$

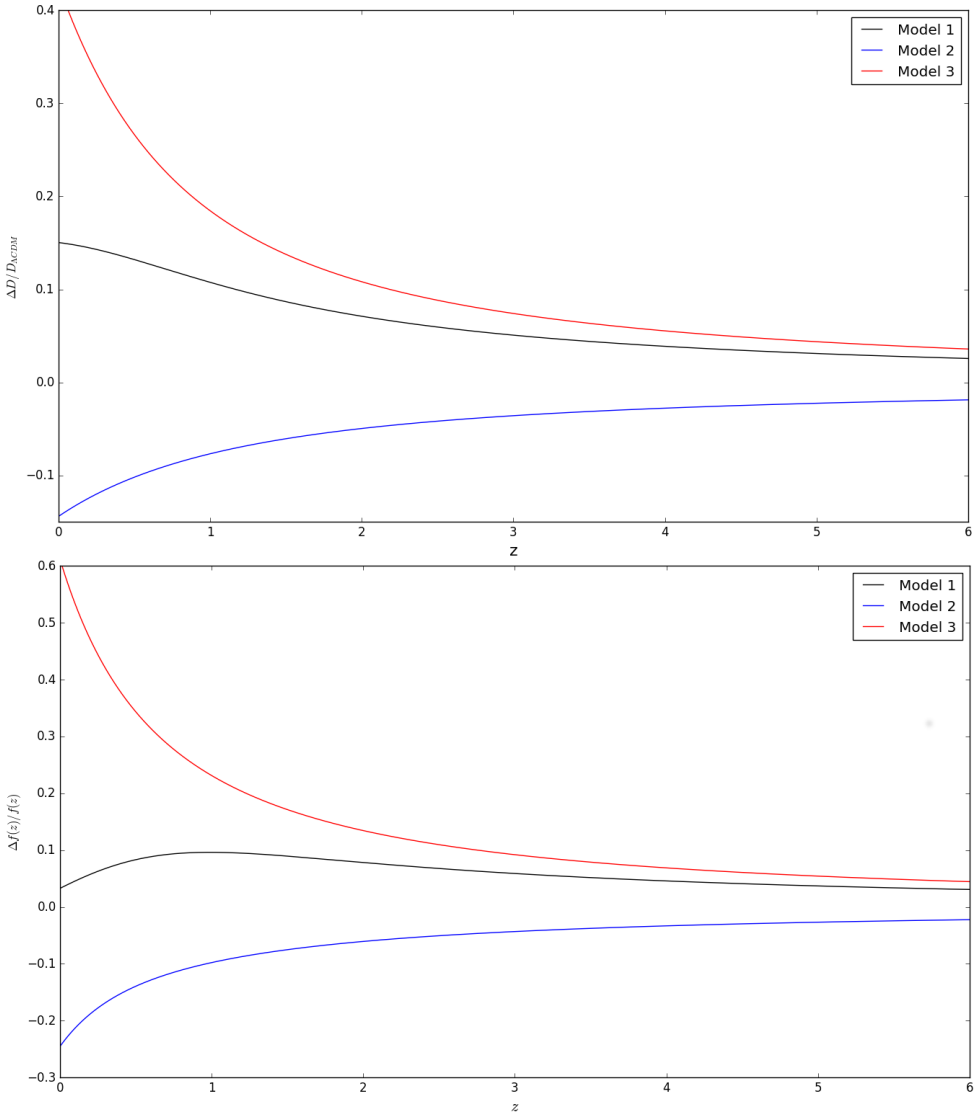

Figure 5.8: **Upper panel:** Relative deviation $(D(z) - D_{\Lambda CDM}(z)/D_{\Lambda CDM}(z))$ of the linear growth factor from the ΛCDM reference, for the same models defined in Table (5.1)
Lower panel: Relative deviation $((f(z) - f_{\Lambda CDM}(z))/f_{\Lambda CDM}(z))$ of the factor $f = \mathrm{dln}D/\mathrm{dln}a$ with respect to the ΛCDM reference, for the same models as above.

From Eq. (3.92) we see that:

$$D_{ISW}(k,z) = 3\Omega_m^{(0)} \left(\frac{H_0}{k}\right)^2 \frac{\mathrm{d}D_{\Psi_N}}{\mathrm{d}z}, \tag{5.22}$$

thus the derivative with respect to the redshift of D_{Ψ_N} constitutes the kernel of the integral I_l^{ISW} and enters directly in the computation of $C_l^{ISW-gal}$, indeed a late ISW effect arises when dark energy modifies the linear growing mode and makes $|\Psi_N|$ decrease. For K-moufage models the derivative with respect to the redshift can be computed as:

$$\frac{\mathrm{d}D_{\Psi_N}}{\mathrm{d}z} = -a^2 \frac{\mathrm{d}D_{\Psi_N}}{\mathrm{d}a} = -AD(\epsilon_2 + f - 1). \tag{5.23}$$

In Figure (5.9) we report our results for $\mathrm{d}D_{\Psi_N}/\mathrm{d}z$, comparing the models of K-mouflage we have analysed and the ΛCDM.

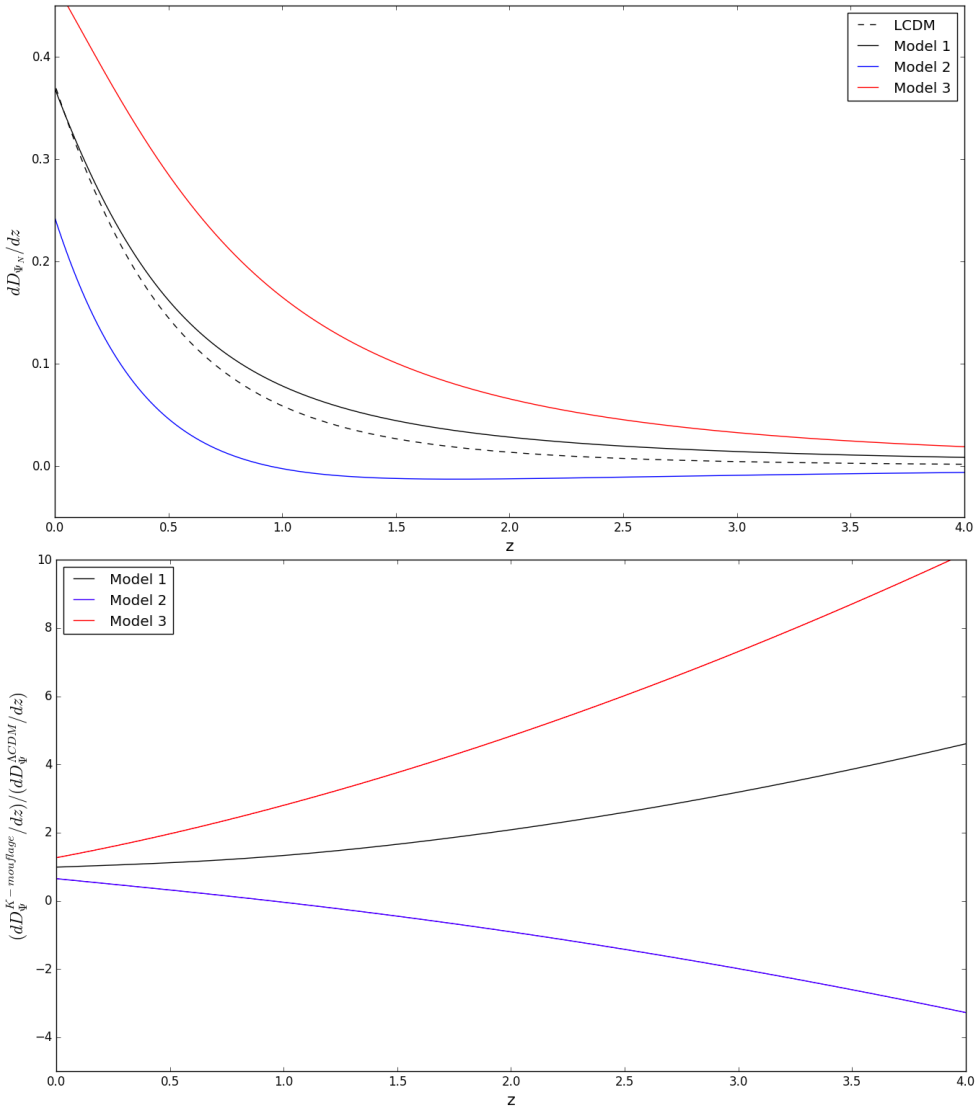

Figure 5.9: **Upper panel:** the factor ($\mathrm{d}D_{\Psi_N}/\mathrm{d}z$) of Eq. (5.23) for the reference ΛCDM Universe and the scenarios of Table (5.1)
Lower panel: ratio of these factors ($\mathrm{d}D_{\Psi_N}/\mathrm{d}z$) to the ΛCDM reference

At high z, we recover the Einstein-de Sitter cosmology and the derivative $-\mathrm{d}D_{\Psi_N}/\mathrm{d}z$ goes to zero for all models. For the modified-gravity models, we have $\bar{A} \simeq 1$ and $f(z)$ remains quite close to the ΛCDM reference, as seen in Fig. (5.8). Thus, the main source of deviation from the ΛCDM prediction is the coefficient ϵ_2 in Eq.(5.9).
For scenarios with $\bar{K}' > 0$, we have seen in Fig. (5.7) that ϵ_2 is negative, like $(f-1)$. Then, $-\mathrm{d}D_{\Psi_N}/\mathrm{d}z$ is negative, as in the ΛCDM reference (i.e., linear gravitational potentials decay with time in the dark energy era). For Model 1, where ϵ_2 goes to zero at late times, the factor $\mathrm{d}D_{\Psi_N}/\mathrm{d}z$ always remains close to the ΛCDM reference, whereas for Model 3, where ϵ_2 converges to a finite value, the deviation remains significant at low z.
For scenarios with $\bar{K}' < 0$, as we have seen in Fig. (5.7) lower panel, ϵ_2 is positive and decreases slowly at high redshift. Then, the term ϵ_2 can dominate over the factor $(f-1)$ at early times and, as shown in Fig. (5.9) for the Model

2, $(\mathrm{d}D_{\Psi_N}/\mathrm{d}z)$ becomes negative for $z \gtrsim 0.4$. Therefore, in similar models with negative K_0, the derivative of the gravitational growing mode changes sign, and there is a phase in which the gravitational potential slowly grows with time despite the dynamic effect of the scalar field is no longer negligible.
The lower panel in Fig. (5.9) shows the ratio of $\mathrm{d}D_{\Psi_N}/\mathrm{d}z$ to the ΛCDM solution. In agreement with the upper panel and the discussion above, this ratio remains positive for Model 1 and Model 3 (with $\bar{K}' > 0$) and becomes negative at high redshift for Model 2($\bar{K}' < 0$). In both cases, because of the factor ϵ_2, which decays rather slowly with redshift, $(\mathrm{d}D_{\Psi_N}/\mathrm{d}z)$ decays more slowly than the ΛCDM prediction at high z. This yields a ratio to the ΛCDM reference that grows at high z.
Thus, although the most of the late ISW signal originates at low redshift as we can see from the upper panel of Fig. (5.9), the results of the lower panel suggest that a significant deviation between modified gravity scenarios and ΛCDM in the cross-correlation power spectrum should be measured at at $z \gtrsim 1$.
Finally, we again invite the reader to compare our results with those obtained in [15]. For the coefficients ϵ_1 and ϵ_2 we recover exactly the same solution of [15]. Nevertheless, when checking our results for the growth factor D (and for all the derived quantities like $f(z)$ and $\mathrm{d}D_{\Psi_N}/\mathrm{d}z$), we found a non-negligible discrepancy with [15]. Specifically, the deviation between the growth factor $D(z)$ in K-mouflage and the ΛCDM reference, that we report in Fig. (5.8), results slightly higher than that found in [15]. The fact that all the background quantities and the ϵ coefficients are in agreement with the results of [15]. indicates that this difference should be related to the computation procedure. After checking our results against errors or numerical instabilities as discussed in Sec. (5.1.2) without finding any critical issues in our procedure, we contacted the author of [15]. for a direct comparison.
In the end, we can state that our result represents the correct solution of the growth factor equation in K-mouflage.

Chapter 6

Cross-correlation analysis

The purpose of this Chapter is to study the ISW-galaxy cross-correlation in the case of K-mouflage models and to forecast about the possibility of distinguish K-mouflage models from ΛCDM using data from the upcoming wide and deep galaxy surveys.
As we have outlined in the last Chapter, the late ISW signal is expected to decay more slowly with redshift (see our discussion of Sec. (5.3)) in K-mouflage with respect to ΛCDM. This different redshift evolution makes it interesting to study the cross-correlation signal in different redshift bins. Extremely deep and wide surveys, will gather an exceptional catalog of sources. In particular their main galaxy distribution will extend to very high redshifts. This makes them ideal for a tomographic study of the ISW effect through CMB-galaxy cross-correlation.
For our purpose we concentrated on two promising surveys, Euclid and LSST, that are optimized for CMB-galaxy cross-correlation [34][73][62]. In the first Section we describe the two surveys, then we illustrate the numerical methods adopted in our analysis, and finally we show our results. All the results shown in this Chapter, refers to cosmological models with parameters specified in Table (2.1), third column (Planck 2015).

6.1 Upcoming cosmological surveys

Nowadays the exploration of the Universe can be performed by a variety of observational probes and methods over a wide range of the wavelengths: the temperature anisotropy map of the cosmic microwave background (CMB), the Hubble diagrams of nearby galaxies and distant Type Ia supernovae, wide-field photometric and spectroscopic surveys of galaxies, deep surveys of galaxies in sub-mm, infrared, and optical bands, quasar surveys in radio and optical, strong and weak lensing of distant galaxies and quasars, high-energy cosmic rays, and so on. Among those, galaxy redshift surveys, i.e. surveys that observes a large number of galaxies measuring their redshifts, are the most classical. Indeed one may phrase that the modern observational cosmology started with a sort of galaxy redshift survey by Edwin Hubble. The scientific results achieved so far by this kind of cosmological probes motivated the production of considerably more extended surveys.
In order to probe Dark Energy, that manifests its effects on the overall structure and evolution of the Universe, we need to sample enough large volumes and to probe different epochs of the cosmic evolution. Observationally these requirements

are only met by big surveys that probe wide areas of sky and that are deep enough to sample structure at high redshifts. By averaging over substantially larger volumes in the Universe, it is expected that the statistics on the galaxy distribution could be significantly improved. In addition, the analysis of the galaxy distribution at higher redshift enable a better measurement of the growth of cosmic structures. This two features will allow to probe Dark Energy using the ISW effect, with much more efficiency than the present. Two very extensive redshift surveys are planned with these main objectives in mind: Euclid and LSST.
One of the main challenges that needs to be addressed by future wide surveys, comes from the requirement that the redshift distribution of observed galaxies be known to high precision. Since the depth and large number density of typical galaxy samples preclude the possibility of obtaining spectroscopic redshifts for all galaxies, the standard approach is to employ broadband photometry, using the measured flux through a number of bands to estimate redshifts. These photometric redshifts (photo-z's) can also be used to divide the sample into tomographic bins, which allows the extraction of information on redshift evolution of the background cosmology and of large scale structure. Since photometric redshifts are essentially based on very low resolution spectra, they tend to have large uncertainties ($\sigma_z \sim 0.03 - 0.1$).

6.1.1 Euclid

Euclid is a space-based Medium Class mission of the ESA Cosmic Vision 2015-2025 programme [73], and will be launched in 2020. It will consist in a satellite orbiting around the 2^{nd} Lagrange point of the Sun-Earth System.
Its primary goal is to place high accuracy constraints on Dark Energy, Dark Matter, Gravity and cosmic initial conditions using two independent cosmological probes: weak gravitational lensing (WL) and baryonic acoustic oscillations (BAO). For this purpose, Euclid will measure the shape and spectra of galaxies over the entire extragalactic sky in the visible and near-infrared, out to redshift 2, thus covering the period over which dark energy accelerated the universe expansion. Euclid is also optimized for probing cosmology using galaxy clusters observations and the Integrated Sachs-Wolfe effect. The Euclid datasets will also provide unique legacy surveys for the study of galaxy evolution, large-scale structure, the search for high redshift objects and for various other fields of astronomy.
The baseline mission is based on a 1.2 m Korsch telescope designed to provide a large field of view (see Fig. (6.1)). The telescope directs the light to two instruments via a dichroic filter in the exit pupil. The reflected light is led to the visual instrument (VIS) and the transmitted light from the dichroic feeds the near infrared instrument (NISP) which contains a slitless spectrometer and a three bands photometer. Both instruments cover a large common field-of-view of $\sim 0.54 deg^2$. VIS is equipped with 36 CCDs and is used to measure the shapes of galaxies for weak lensing, with a resolution better than $0.2 arcsec$ (PSF FWHM) in a wide visible red band ($R + I + Z$, $550 - 920 nm$). The near-infrared photometric channel provides three near-infrared bands (Y, J, H, spanning $1000 - 1600 nm$) with a resolution of $0.3 arcsec$. The baseline for the NIR spectroscopic channel operates in the wavelength range $1.0 - 2.0 \mu m$ in While the VIS and NISP operate in parallel, the NISP performs the spectroscopy and photometry measurements in sequence by selecting a grism wheel in case of spectroscopy and a filter wheel in

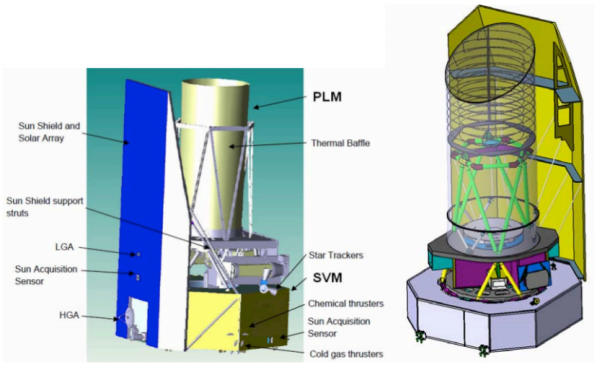

Figure 6.1: Euclid Spacecraft concept from EADS [73]

case of photometry.
The mission will perform a wide survey that covers $15,000 deg^2$ of the extragalactic sky and is complemented by two $20 deg^2$ deep fields observed on a monthly basis. The wide survey will measure the shapes of 30 resolved galaxies per $arcmin^2$ in one broad visible $R+I+Z$ band $(550-920nm)$ down to AB mag 24.5 (10 σ). For all galaxies, photometric redshifts will be obtained from the broad-band visible and near-IR measurements and complementary ground-based observations in other visible bands, reaching a precision of $\sigma_z/(1+z) < 0.05$. For $40-60$ million galaxies with Hα line flux level $\gtrsim 3 \cdot 10^{16} ergs^{-1} cm^{-2}$, the slitless spectrometer will directly measure the redshift with a $\sigma_z/(1+z) < 0.001$.

6.1.2 Large Synoptic Survey Telescope

The *Large Synoptic Survey Telescope* (LSST) [62] is one of the most ambitious survey currently planned in the optical wavelength range. LSST will be a large, wide-field ground-based system, located on the El Peñón peak of Cerro Pachón, in northern Chile. The telescope, shown in Fig. (6.2), is currently under construction and will have his first light in 2019 while scientific operations will start by 2021. The telescope design is a three-mirror anastigmatic, also called a Mersenne-Schmidt, which proposes a mirror configuration that reduces optical aberrations. The mirror characteristics as well as the corrective lenses are detailed on Fig. (6.3). The primary mirror, already build, reach a diameter size of $8.4m$, including the $5.0m$ tertiary mirror embedded at its center. Combined with a field-of-view of $9.8 deg^2$, these mirrors will enable the LSST to reach an unprecedented depth for a wide-field survey [85].

The camera built for LSST is a 3.2-Gigapixel prime focus digital camera, the largest digital camera ever constructed. The focal plane is about $64cm$ large, consisting in a mosaic of 189 CCD detectors, each of 16-Megapixel, which allow the detection of photons in the visible and near-infrared domains. It includes a shutter and a filter changing mechanism.
This system can image about $10,000$ square degrees of sky in three clear nights using pairs of 15-second exposures twice per night, with typical 5σ depth for point sources of $r \sim 24.5 (AB)$.
The telescope is designed to yield high image quality as well as superb astrometric and photometric accuracy. The overall system image quality budget for the LSST is 0.4 arcsecond FWHM. With this image quality budget the LSST's delivered

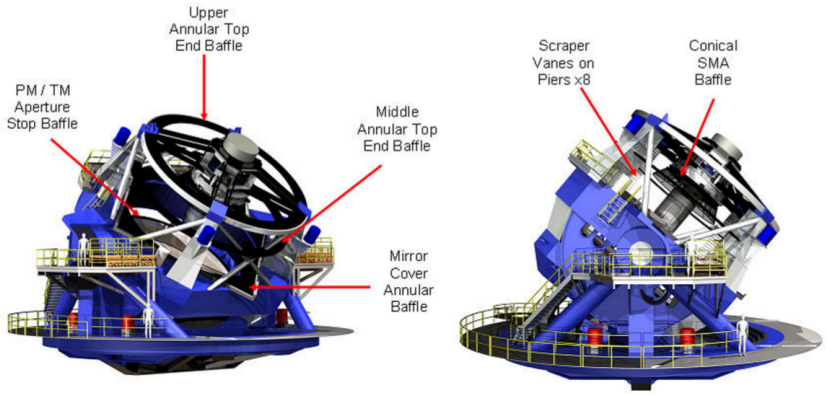

Figure 6.2: Rendering of the telescope, showing mirror support structures, top end camera assembly, and integrated [62]

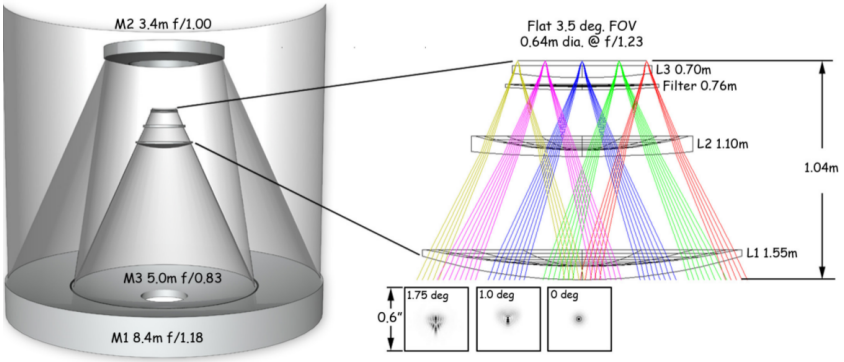

Figure 6.3: The optical design configuration showing the telescope (left) and camera (right) layouts. Diffraction images in r for three field radii, 0, 1.0, and 1.75 degrees, are shown in boxes 0.6 arcseconds square [62]

resolution is dominated by the atmospheric seeing at its site on Cerro Pachòn in Chile. In order to preserve its resolving power LSST will use an active optics system. Corrective actions fed to the LSST AOS are determined from information derived from 4 curvature wavefront sensors located at the corners of the focal plane [85].

The survey will yield contiguous overlapping imaging of over half the sky in six broad optical bands *ugrizy*, covering the wavelength range $320 - 1050nm$. As mentioned earlier, the thickness of the silicon detectors allows for near-infrared photons to be detected, which is of great advantage for e.g. the computation of the photometric redshift. About 90% of the observing time will be devoted to a deep-wide-fast survey mode which will uniformly observe a $20.000deg^2$ region about 800 times (summed over all six bands) during the anticipated 10 years of operations, and yield a coadded map to $r \sim 27.5$. This survey will allow the measurement of photometric redshifts with a precision of of $\sigma_z/(1+z) < 0.05$, in the optimistic case reaching $\sigma_z/(1+z) = 0.02$ [62].

These data will result in databases including $\sim 2 \cdot 10^{10}$ galaxies and a similar number of stars, and will serve the majority of the primary science programs. The remaining 10% of the observing time will be allocated to special projects such as a Very Deep and Fast time domain survey.

A vast array of science will be enabled by this single wide-deep-fast sky survey.

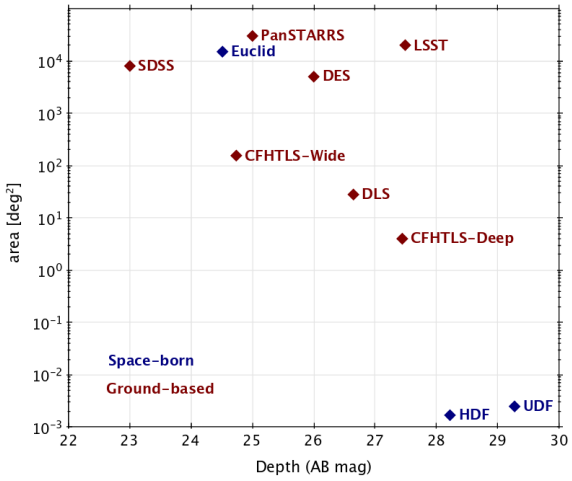

Figure 6.4: Diagram of final survey area and depht of optical and near-infrared surveys [13]

Indeed the LSST design is driven by four main science themes: probing dark energy and dark matter, taking an inventory of the Solar System, exploring the transient optical sky, and mapping the Milky Way. The LSST instrument shows an extreme adaptability to study a huge variety of objects, from stars to galaxy clusters, transients from asteroids to supernovae, and scales from a few kiloparsecs (solar system) to cosmological scales.
All these goals have set challenging requirements for the instrument and telescope. The most important goals concerning this thesis work are the magnitude limit, that should reach $r = 27.5$ (see Table 6.1) in order to obtain a number counts of galaxies of ~ 50 per $arcmin^2$, and the sky coverage, that should reach at least $20000 deg^2$. A comparison of galaxy surveys doing weak lensing science is shown on Fig. (6.4) .
Thanks to its performances, LSST is expected to measure the ISW effect (through cross-correlation with CMB data) to greater precision than current efforts involving combinations of galaxy catalogs from multiple sources, already in the first year of operation.

Table 6.1 – LSST baseline imaging parameters. The depths are given in AB magnitude (5 σ significance), and correspond to point sources and zenith observations. The number of visits are averaged on the sky position [53].

Band	u	g	r	i	z	y
Single visit depth	23.9	25.0	24.7	24.0	23.3	22.1
Average number of visits (10yr)	56	80	184	184	160	160
Coadded (final) depth	26.1	27.4	27.5	26.8	26.1	24.9

6.2 Algorithm implementation

In this Section we describe the numerical methods and the structure of algorithms that we have implemented in the `Python` programming language to compute different type of power spectra.
All the results shown in this Chapter have required the numerical resolution of definite integrals. In particular the computation of the cross-correlation power-spectrum $C_l^{ISW-gal}$, that is the fundamental quantity in our analysis, relies on

the solution of the two integrals over redshift given by Eq. (3.88) and Eq. (3.91) and of the integral over the wave number k in Eq. 3.87. The computation of this tern of integrals had to be repeated for each multipole order ℓ to obtain the complete $C_l^{ISW-gal}$.
The main problem we had to face was that this process involves the computation of the spherical Bessel function $j_l(k\chi(z))$ in a large number of points and their subsequent integration. This is not an easy task to address numerically. In fact spherical Bessel functions are quite expensive to compute and can be hard to integrate numerically due to their rapid oscillation.
To compute the spherical Bessel function, the library SciPy of `Python` implements a specific `Python` function, but we verified that this is unstable for high multipole orders. For this reason we computed each j_l starting from the ordinary Bessel function J_l (also included in the SciPy library) and using the following relation [84]:

$$j_l(x) = \sqrt{\frac{\pi}{2x}} J_{l+\frac{1}{2}}(x). \tag{6.1}$$

For the numerical computation of definite integrals, we tried different methods, looking for the one that best suited our needs.
In particular we tested three types of numerical integrations: the trapezoidal rule, the Simpson rule and the adaptive quadrature method. The first two methods are based on the following approximations of definite integrals:

$$\text{Trapezoidal}: \quad \int_a^b f(x)\mathrm{d}x \approx \frac{1}{2}\sum_{i=1}^{N-1}\left[(x_{i+1}-x_i)(f(x_{i+1})+f(x_i))\right], \tag{6.2}$$

$$error < \frac{(b-a)^3}{12N^2}\max_{\xi\in[a,b]}|f''(\xi)|;$$

$$\text{Simspon}: \quad \int_a^b f(x)\mathrm{d}x \approx \frac{b-a}{3N}\sum_{i=1}^{N/2}\left[f(x_{2i-2})+4f(x_{2i-1})+f(x_{2i})\right], \tag{6.3}$$

$$error < \frac{(b-a)^4}{180N^4}\max_{\xi\in[a,b]}|f^{(4)}(\xi)|.$$

Where N is the number of points used to sample the integration interval. The trapezoidal and the Simpson rules are basics method and allow a fast computation, but require to sample the integration variable.
On the contrary adaptive quadrature methods automatically chose the sampling depending on the behaviour of the integrand function. Adaptive methods take in input a given tolerance and at every step compute the integral in the same way of static methods, like e.g. using Newton-Cotes formulas (that generalize those in Eq. (6.2) and Eq. (6.3)). However in the case of adaptive quadrature at every step the algorithm gives an estimate of the error and checks if it is larger than the required tolerance, in which case the sampling interval is further subdivided to increase the precision. Adaptive quadrature methods are implemented in `Python` by the function *scipy.integrate.quad*, that uses a technique from the Fortan library QUADPACK.
In our scripts we have implemented the Simpson method when we had to compute integrals on redshift, like those of Eq. (3.88) and Eq. (3.88). This was necessary because we needed to integrate discretized functions like the growth factor $D(z)$ and its derivative. To sample the redshift interval of integration we chose a non-constant step. The integrand functions D_{ISW} and the comoving distance

$\chi(z)$ (argument of $j_l(k\chi)$) vary rapidly at low resdshift (both in ΛCDM that in K-mouflage models) and then reach a plateau at higher z; thus the integrand needs to be oversampled near $z = 0$. For this reason we have chosen to divide the redshift interval $[0, z_o]$ with the following N nodes:

$$z_i = z_0 - z_0 \cos\left(\frac{\pi}{2}\frac{i-1}{N}\right), \quad i = 1, ..., N+1. \tag{6.4}$$

this induces a denser sampling to the lowest z with respect to higher ones.
After choosing the integration method and fixing the sampling, we had to fix the integration boundaries. The integrals on redshift would be in principle computed for all z , but practically we are limited by the selection function (i.e. the galaxy distribution of the survey introduced in Eq. (3.81)), and by the decay of the function D_{ISW}, see Fig. (5.9), so that we expect a null signal after $z \sim 10$, we tested different $20 < z_0 < 100$, always obtaining the same results.
After the computation of I_l^{gal} and I_l^{ISW}, our scripts compute the cross-correlation power spectrum from Eq. (3.87). Fo the integration over the wave number k we used an adaptive quadrature method. We verified that the results given by the adaptive quadrature were in agreement with those obtained using the Simpson rule or the Trapezoidal rule. To obtain results accurate to $\sim 1\%$, we chose a tolerance of about 3 order of magnitude less than the value of $C_l^{ISW-gal}$, keeping in mind that requiring a smaller tolerance amounts to increase the computational time.
One strategy to significantly reduce the computational time, avoiding the problems related to the numerical solution of integrals of rapidly varying function (spherical Bessel functions), consists in computing the power spectra using the Limber approximation that we introduced in Eq (3.93), thus solving the single integral in Eq. (3.94). The Limber approximation [61] is a powerful method to accurately estimate the magnitude and understand the analytic dependencies of the power spectra. Since the Limber approximation reduces the number of integrals, numerical calculations are simpler. In adopting the Limber approximation, one implicitly assumes that the part of the integrand that is independent on the sperical Bessel functions is more slowly varying than the j_l part. The Limber approximation is accurate only when the width of the redshift selection function (or of the redshift bin) is much larger than the linear size corresponding to the angular scale of interest. In other words, the cross-correlation power spectra calculated using Eq. (3.94) are not accurate on large scales (low ℓ) (see [61]). For this reason we decide to compute the first ~ 20 multipole orders using the exact procedure, and to apply the Limber approximation for the subsequent "l".
Another strategy that we tested in our scripts in order to reduce the computational time, is to compute the exact $C_l^{ISW-gal}$ for a representative sample of ℓ (about 30 points chosen between $l = 2$ and $l = 250$) and than perform a cubic-spline interpolation to obtain the complete power spectrum.
The computation of $C_l^{ISW-gal}$ from Eq. (3.87) also requires the knowledge of the matter power spectrum $P(k)$ at the present time. This was computed from Eq. (3.43] taking for the spectral index n_s the value given in Table 2.1 (Planck 2015). We computed the transfer function $T(k)$ and δ_H applying the fitting formula given in [35], that includes contributions of the baryonic matter, especially it reproduces the baryon acoustic oscillations features; more simple (but less accurate) fitting formulas are reported in [ref] and [59]. After computing $P(k)$ we normalized it to the Planck 2015 σ_8 value given in Table (2.1), following the procedure

illustrated in Sec. (3.1.4). The result is shown in Fig. (3.3). To estimate of the errors in our analysis (see discussion below), it was also necessary to compute the auto-correlation power spectrum of galaxies C_l^{gg} and the angular power spectrum of CMB anisotropies C_l^{TT}. The former was computed from the following integral:

$$C_l^{gg} = \frac{2}{\pi} \int \mathrm{d}k \; k^2 P(k) (I_l^{gal})^2, \tag{6.5}$$

with I_l^{gal} given by Eq. (3.88). To obtain C_l^{TT}, we used a package of Python that encapsulate the Fortran code CAMB, which is very useful for cosmological applications.

6.3 Cross-correlation power spectra

In this Section we develop a cross-correlation analysis, comparing the results for different models of K-mouflage with those of ΛCDM, and estimating the significance of a possible future detection. The main goal of this analysis is to forecast about the possibility of investigating K-mouflage using the differences in the late ISW effect predicted by such theory, opening the way to more detailed studies.
Following the standard procedure for similar forecasts [60] [48][32][34][43] [78][10], we bin the (predicted) redshift distribution of galaxies for Euclid and LSST, then we compute ISW-galaxy cross-correlation power spectra from Eq. (3.87), for all the three models of K-mouflage defined in Table 5.1 and for ΛCDM.
Considering the upcoming surveys Euclid and LSST, we assume a parametrization of the redshift distribution of galaxies that is more or less the standard in the literature for this kind of forecasts:

$$\frac{\mathrm{d}N}{\mathrm{d}z} = \frac{1}{\Gamma\left(\frac{\alpha+1}{\beta}\right)} \beta \frac{z^\alpha}{z_0^{\alpha+1}} \exp\left[-\left(\frac{z}{z_0}\right)^\beta\right]. \tag{6.6}$$

The above parametrization gives the normalized distribution of galaxies per steradian, α, β and z_0 are characteristic of each survey and determine the shape of the distribution as well as its median redshift.
We assume that the galaxies have photometric redshifts z_{ph}, characterized by a distribution $p(z_{ph}|z)$ (the probability density for the photometric redshift, given the true galaxy redshift) and that tomographic bins are defined by cuts in z_{ph} . The redshift distribution in a bin is then:

$$\frac{\mathrm{d}n_i}{\mathrm{d}z} = \frac{\mathrm{d}N}{\mathrm{d}z} \int_{z_{i-1}}^{z_i} \mathrm{d}z_{ph} p(z_{ph}|z), \tag{6.7}$$

where z_{i-1} and z_i are the boundaries of the bin. As a baseline model for the photo-z distribution, we assume a Gaussian:

$$p(z_{ph}|z) = \frac{1}{\sqrt{2\pi}\pi\sigma_z(z)} e^{-\frac{1}{2}(z_{ph}-z)/\sigma_z^2} \tag{6.8}$$

characterized by a scatter σ_z. In reality, the photo-z distribution is typically not Gaussian, but the Gaussian form serves as a simple ansatz with which to include uncertainties in the photo-z measurements. We assume a fiducial of $\sigma_z = 0.05(1+z)$ for Euclid and $\sigma_z = 0.02(1+z)$ for LSST.

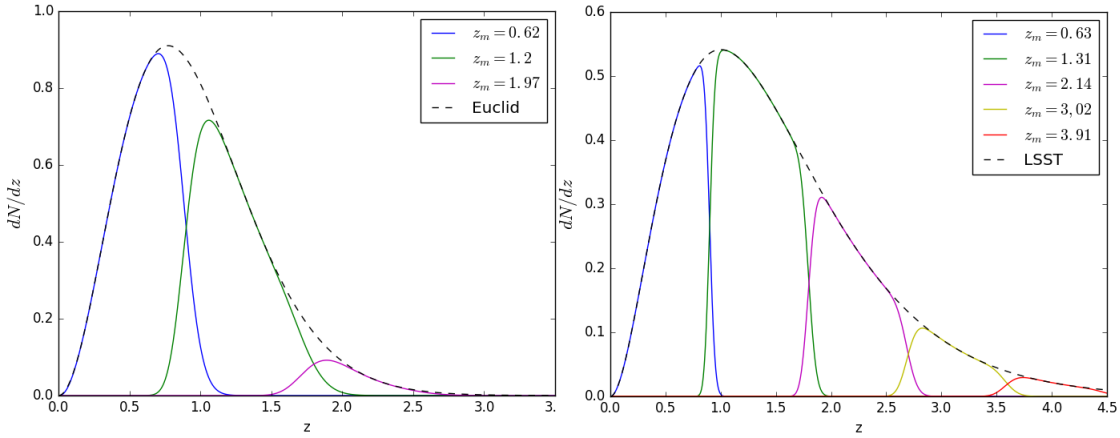

Figure 6.5: **N**ormalized redshift distribution for Euclid and LSST and redshift bins. Each bin is labelled with its median redshift.

Table 6.2. Properties of the upcoming surveys considered in this analysis. We consider photometric surveys, for LSST we follow the forecast of [62], while for Euclid we assume the same predictions given in [3].

	Euclid-like survey	LSST-like survey
Number density	$n_g = 30$ arcmin^{-2}	$n_g = 50$ arcmin^{-2}
Sky coverage	15.000 deg^2	20.000 deg^2
Redshift distribution (6.6)	$\alpha = 2,\ \beta = 1.5,\ z_0 = 0.64$	$\alpha = 2,\ \beta = 1,\ z_0 = 0.5$
Median redshift	$z_m = 0.96$	$z_m = 1.34$
tomography	3 bins	5 bins
photo-z errors	$\sigma_z = 0.05(1+z)$	$\sigma_z = 0.02(1+z)$
galaxy bias	$b = \sqrt{1+z}$	$b = 1 + 0.84z$
multipole range	$l \in [2, 250]$	$l \in [2, 250]$

We divide the Euclid galaxy distribution in 3 equally spaced redshift bins, while for LSST we chose 5 equally spaced redshift bins, with median redshift reported in Fig. (6.5). Solving the integral in Eq. (6.7) we get the following distribution for each redshift bin:

$$\frac{\mathrm{d}n_i}{\mathrm{d}z} = \frac{1}{2}\frac{\mathrm{d}N}{\mathrm{d}z}\left[\mathrm{erfc}\left(\frac{z_{i-1}-z}{\sqrt{2}\sigma_z}\right) - \mathrm{erfc}\left(\frac{z_i - z}{\sqrt{2}\sigma_z}\right)\right], \tag{6.9}$$

where $\mathrm{erfc}(x)$ denotes the complementary error function. The total galaxy distribution and the redshift bins for Euclid and LSST are shown in Fig. (6.5), while the features assumed for each survey are summarized in Table. 6.2.

To compute $C_l^{ISW-gal}$ we also need an estimate of the galaxy bias factor. Since most of the contribution to the CMB-galaxy correlation signal comes from large scales, where perturbations are well described by the linear theory and on such scales, galaxies are expected to closely trace the distribution of dark matter, we can assume a scale-independent bias factor b.

The bias is also known to vary with redshift, hence, each of the photometric bins will, in principle, have a different bias factor. The bias factors corresponding to each bin can be determined from the amplitude of the primordial spectrum extracted from the CMB and the galaxy-galaxy autocorrelation spectra.

In our simplified analysis we assumed the same bias redshift dependence as [62]

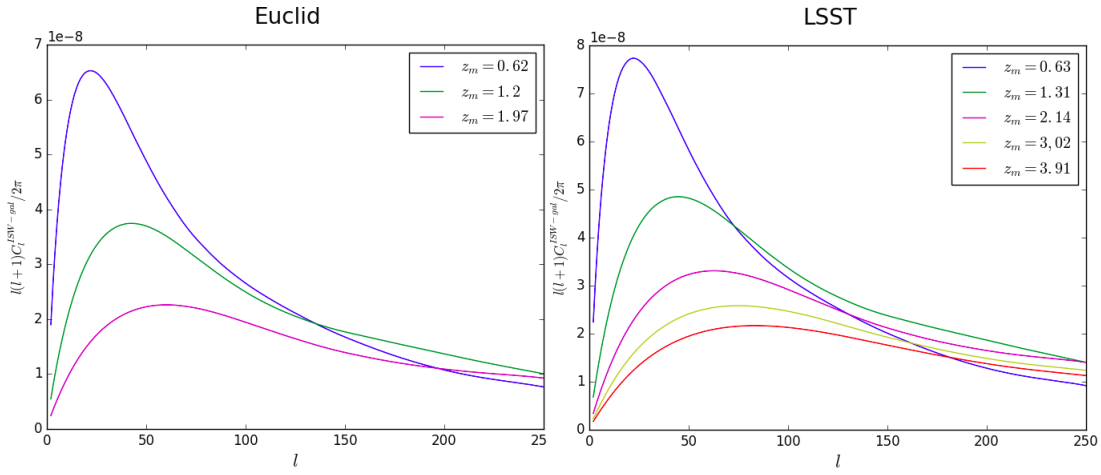

Figure 6.6: ISW-galaxies cross-correlation power spectrum for **Model 1** of Table 5.1. Left panel shows the cross-correlation within 3 redshift bins of the Euclid-like redshift distribution. Right panel shows the cross-correlation within 5 redshift bins of the LSST-like redshift distribution. Each bin is labelled with its median redshift.

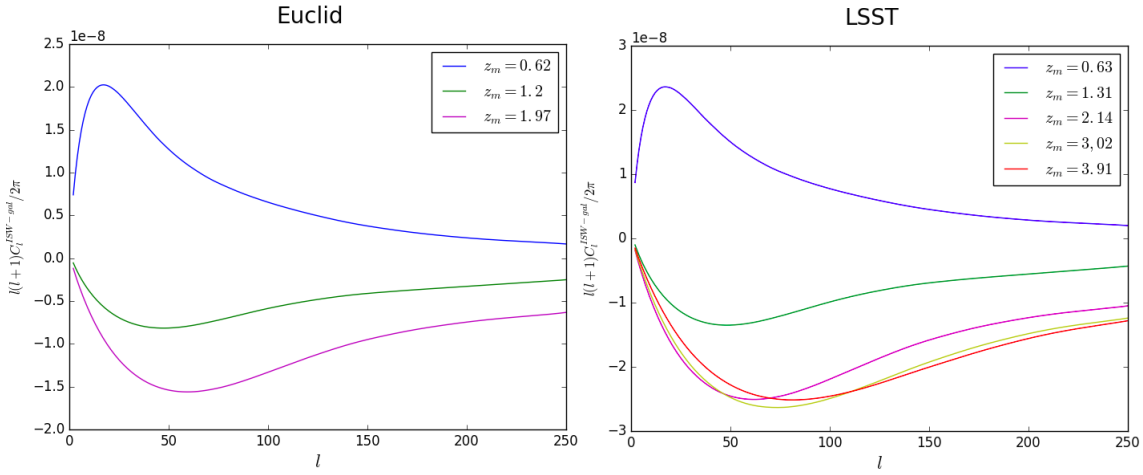

Figure 6.7: ISW-galaxies cross-correlation power spectrum for **Model 2** of Table 5.1. Left panel shows the cross-correlation within 3 redshift bins of the Euclid-like redshift distribution. Right panel shows the cross-correlation within 5 redshift bins of the LSST-like redshift distribution. Each bin is labelled with its median redshift.

for LSST and as [3] for Euclid.
The cross-correlation power spectrum computed in each redshift bin for the K-mouflage models of Table 5.1 and for the ΛCDM are shown in Fig. (6.6)-(6.9). The first thing to note from these plots is that the peak of each power spectrum (l_{max}) is related to the median redshift of the bin. The higher the median redshift z_m, the larger is l_{max}. This is merely a consequence of the fact that the main contribution to $C_l^{ISW-gal}$ is generated by linear scales ($0.01hMpc^{-1} \lesssim k \lesssim 0.01hMpc^{-1}$); on smaller scales the ISW effect is negligible (due to the cancellation of opposite contributions); On very large scales the cross-correlation signal naturally decreases with the reduction in clustering (the decaying in the matter power spectrum). Due to the projection effect discussed in Chapter 3, the same comoving scale is seen at higher multipoles ℓ if we are observing it at an higher redshift, thus the comoving scale at which the maximum cross-correlation

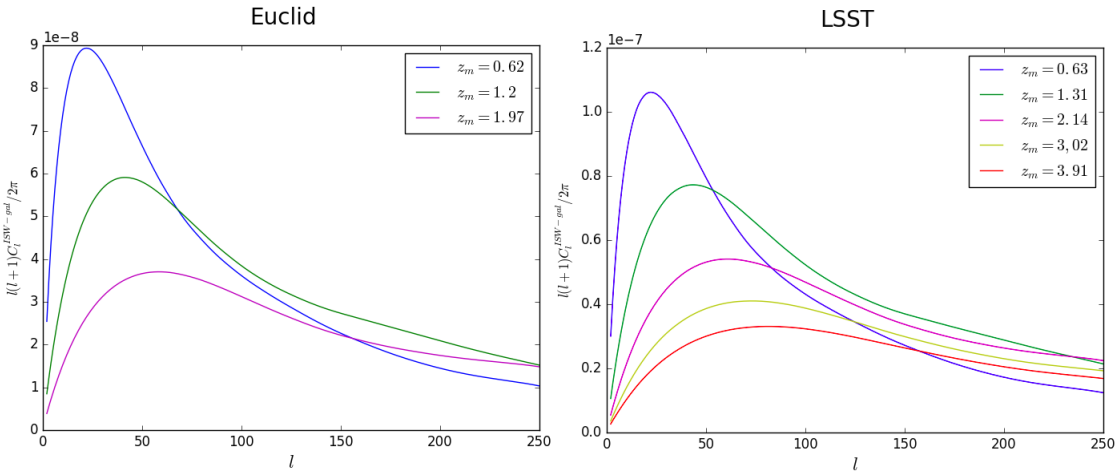

Figure 6.8: ISW-galaxies cross-correlation power spectrum for **Model 3** of Table 5.1. Left panel shows the cross-correlation within 3 redshift bins of the Euclid-like redshift distribution. Right panel shows the cross-correlation within 5 redshift bins of the LSST-like redshift distribution. Each bin is labelled with its median redshift.

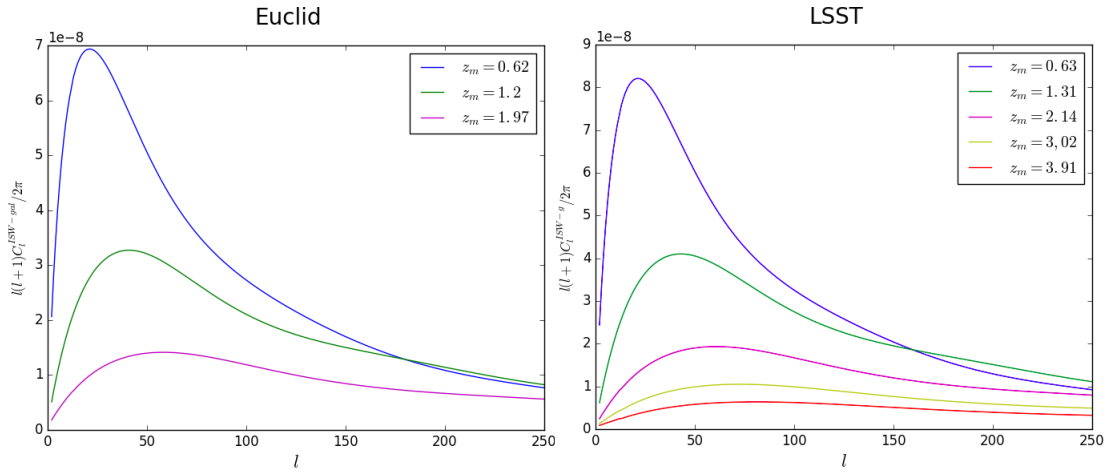

Figure 6.9: ISW-galaxies cross-correlation power spectrum for ΛCDM of Table 5.1. Left panel shows the cross-correlation within 3 redshift bins of the Euclid-like redshift distribution. Right panel shows the cross-correlation within 5 redshift bins of the LSST-like redshift distribution. Each bin is labelled with its median redshift.

is generated is seen at different l_{max} depending on the redshift.
Comparing the corresponding results obtained for the same models but different surveys (i.e. comparing left and right panel of each Figure), we note that $C_l^{ISW-gal}$ is systematically enhanced for the LSST-like survey with respect to the Euclid-like. This is likely due to the different choice for the galaxy bias parametrization $b(z)$ for the two surveys (as shown in Table 6.2, the bias for an LSST-like survey is supposed to be larger than for a Euclid-like survey at all redshift). The effect of the bias can be seen e.g. looking at the approximated expression for $C_l^{ISW-gal}$, Eq. (3.94), from what we see that the bias factor direct contributes to the integrand function, an than to the final result. From a more physical point of view, a larger bias means that the dark-matter over-densities are underestimated by the luminous matter tracer. Since the ISW effect is related to the gravitational potential, it is sensitive to the total mass distribution, thus a

larger galaxy bias corresponds enhance the ISW-galaxies cross-correlation signal. Finally we compare our results for the different models we considered (i.e. comparing the corresponding panels of each Figure). We note that, at least for low multipoles, the amplitude of $C_l^{ISW-gal}$ decreases with the median redshift of the redshift bin for all the models considered. This is expected from our discussion of Sec. (5.3), in particular looking at Fig. (5.9) we see that the fundamental quantity $\frac{\mathrm{d}D_{\Psi_N}}{\mathrm{d}z}$ which originates the cross-correlation signal, grows at low redshifts. For the Model 2 we outline the striking result of an anti-correlation between the ISW effect and the galaxy distribution at high redshift. The negative value of $C_l^{ISW-gal}$ is again expected from the change in sign of the quantity $\frac{\mathrm{d}D_{\Psi_N}}{\mathrm{d}z}$ for the Model 2 of K-mouflage and represents a feature also predicted in other scenarios of modified gravity, e.g. TeVes as shown by Schmidt, Liguori and Dodelson in [78].

6.3.1 Error analysis

As a last step in our work, we investigate the detectability of the K-mouflage models via cross-correlation. To do this, we must first estimate the error on a possible measurement of $C_l^{ISW-gal}$. Assuming a Gaussian distribution we can write the variance of $C_l^{ISW-gal}$ as:

$$(\Delta C_l^{ISW-gal})^2 = \left\langle \left(C_l^{ISW-gal}\right)^2 \right\rangle - \left\langle C_l^{ISW-gal} \right\rangle^2 = \left\langle a_{lm}^{ISW} \left(a_{l'm'}^{gal}\right)^* \right\rangle + \left\langle a_{lm}^{gal} \left(a_{l'm'}^{gal}\right)^* \right\rangle \left\langle a_{lm}^{ISW} \left(a_{l'm'}^{ISW}\right)^* \right\rangle = = \left(C_l^{ISW-gal}\right)^2 + \left(C_l^{gg}\right)\left(C_l^{ISW-ISW}\right). \quad (6.10)$$

Since in reality the power spectrum $C_l^{ISW-ISW}$ is undetectable (see our discussion of Sec. (3.3)), due the noise originated by primary temperature anisotropies of the CMB, we have to take into account the total CMB angular power spectrum C_l^{TT}. This leads to the cumulative signal-to-noise ratio estimated in Eq. (3.95). The estimate in Eq. (3.95) is still not valid for practical applications, since it assumes a 100 % sky coverage and zero instrumental noise and shot noise. For a more realistic estimate we assume the following error associated to $C_l^{ISW-gal}$ in a given redshift bin for a single multipole ℓ [78] [34]:

$$\left(\Delta C_l^{ISW-gal}\right)^2 = \frac{1}{f_s(2l+1)}\left(\left(C_l^{ISW-gal}\right)^2 + \left(C_l^{gg} + \frac{1}{n_g}\right)\left(C_l^{TT}\right)\right) \quad (6.11)$$

where $C_l^{ISW-gal}$, $C_l^{gal-gal}$ and C_l^{TT} are the cross-correlation and the auto-correlation power spectra already introduced in Chapter 3, f_s is the fraction of sky covered by the survey and given in Table 6.2, n_g is the number density of galaxies per steradian in the considered redshift bin (so that $4\pi f_s n_g$ is the total number of galaxies in the corresponding redshift bin of the survey).
Assuming the errors given by Eq. (6.11) to be uncorrelated, we can compute the signal-to-noise ratio of the deviation between K-mouflage models and the ΛCDM:

$$\frac{S}{N} = \frac{\left|\left(C_l^{ISW-gal}\right)_{K-mouflage} - \left(C_l^{ISW-gal}\right)_{\Lambda CDM}\right|}{\sqrt{\left(\Delta C_l^{ISW-gal}\right)^2_{K-mouflage} + \left(\Delta C_l^{ISW-gal}\right)^2_{\Lambda CDM}}} \quad (6.12)$$

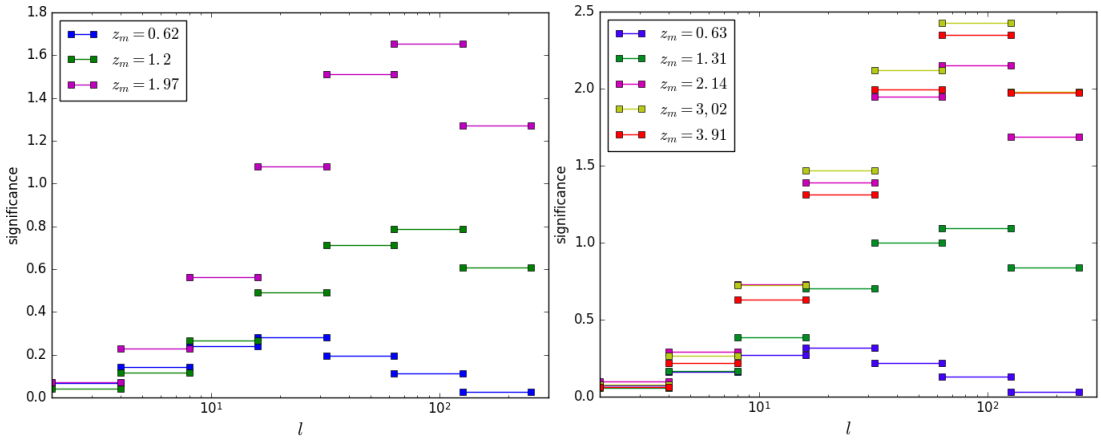

Figure 6.10: **Right panel:** The significance of the Model 1- ΛCDM deviation in the galaxy-CMB cross power for the LSST-like survey; i.e. difference between Model 1 of K-mouflage and ΛCDM divided by the expected error in each angular bin. **Left panel**: same quantity for the Euclide-like survey

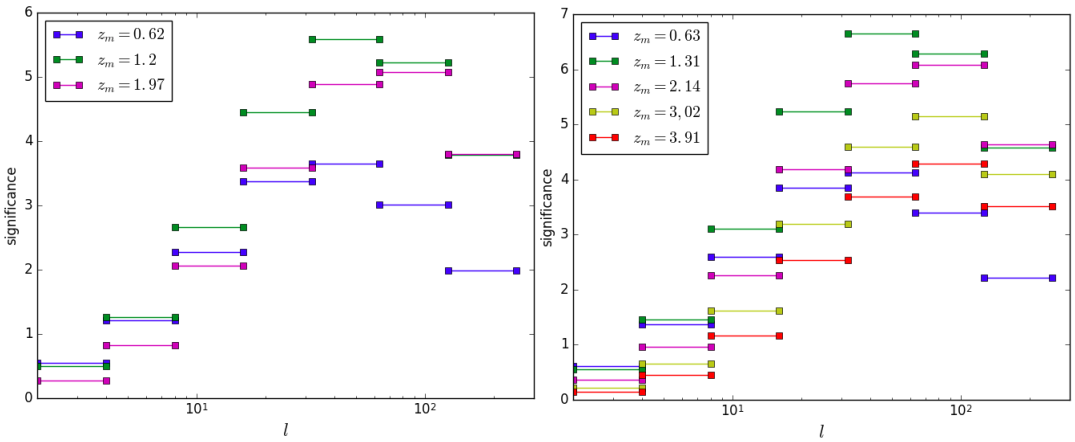

Figure 6.11: **Right panel:** The significance of the Model 2-ΛCDM deviation in the galaxy-CMB cross power for the LSST-like survey; i.e. difference between Model 2 of K-mouflage and ΛCDM divided by the expected error in each angular bin. **Left panel**: same quantity for the Euclide-like survey

To enhance the signal-to-noise ratio we binned the multipole range in 7 angular bins, following the same procedure of [78], then we computed the cumulative signal-to-noise ratio of the deviation between each K-mouflage model and the ΛCDM in each angular bin.
The results are shown in Fig. (6.10)-(6.12), note that the angular binning is chosen as the bins are equally spaced in a logarithmic scale, following [78].
In Figure (6.10) we see that the significance of the deviation from Model 1 and ΛCDM would reach $\sim 2.5\sigma$ for the LSST-like survey and ~ 1.7 using the Euclid-like survey. For Model 2 we obtain the higher significant, near to $\sim 7\sigma$ for the LSST-like survey and near to $\sim 6\sigma$ for the Euclid-like survey. This was expected from the peculiar behaviour of $C_l^{ISW-gal}$ in Model 2, that shows an anti-correlation. Model 3 also is expected to be distinguishable from the reference ΛCDM, with a significance of $\sim 5.5\sigma$ and $\sim 4.5\sigma$ for the LSST survey and for Euclid respectively.
It is interesting to note that for Model 2 and Model 3 we obtain the highest

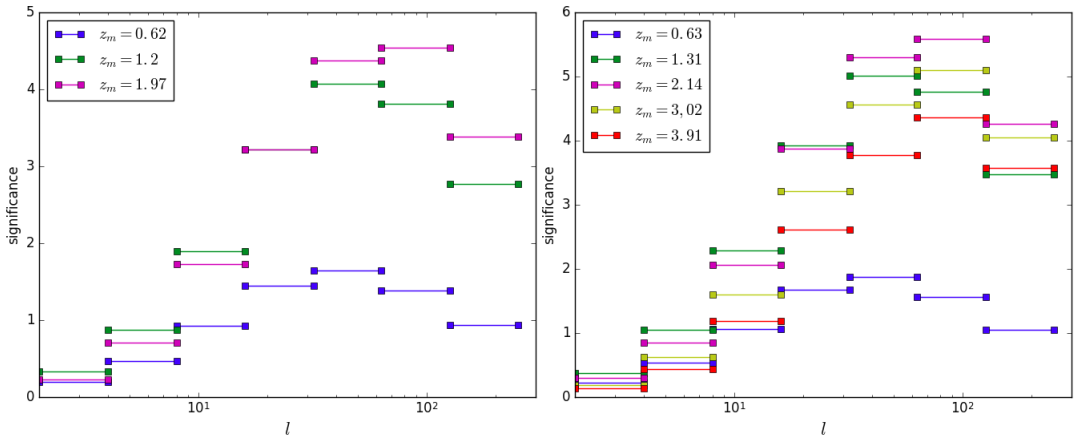

Figure 6.12: **Right panel:** The significance of the Model 3-ΛCDM deviation in the galaxy-CMB cross power for the LSST-like survey; i.e. difference between Model 3 of K-mouflage and ΛCDM divided by the expected error in each angular bin. **Left panel**: same quantity for the Euclide-like survey

significance when we correlate at moderate-high redshift ($z_m \sim 1.3$ and $z_m sim2$ respectively), that are reachable from LSST and from Euclid as well. Only in the case of Model 1, CMB-galaxy cross-correlation at $\gtrsim 3$ seems to enhance the detectability. In all cases the redshift bin with lowest z_m shows the worst result, this is expected from our considerations in the previous Chapter and especially from the result in the lowest panel of Fig. (5.9).
We note that the highest significance arises at $l \sim 10 - 100$; at low multipole orders the noise is dominated by the cosmic variance, this implies a small signal-to-noise ratio, while at large ℓ the cross-correlation signal-to-noise ratio decrease due to the decay of the ISW on small angular scales.
Finally, we observe that the results obtained using the Euclid-like and the LSST-like survey are quite similar after all. Despite the LSST-like survey is supposed (in our forecast) to cover a larger area of sky and to reduce the shot noise in Eq. (6.11) observing an higher number of galaxies with respect to Euclid (see Table 6.2), this differences do not sensibly improve the detectability of K-mouflage models. This is in agreement with what found in [34]. Doupis et al. in [34] find that the S/N plateaus once the source density n_g (reported in Table 6.2 for Euclid and LSST) reaches typically about 10 sources per $arcmin^2$. Above this limit for n_g, the S/N ratio is very sensitive to the sky coverage f_s and to the median redshift z_m. For a given z_m, the larger f_s the higher the detection level. Conversely, at a given f_s, increasing z_m significantly improves the ISW detection only up to $z_m \sim 1$. Thus a survey like Euclid is already nearly optimal for the detection of ISW via cross-correlation, considering the unavoidable limit imposed by cosmic variance.

Chapter 7

Conclusions

The accelerated expansion of the Universe is one of the great mysterious of modern cosmology.
Cosmologists are spending a considerable amount of effort in trying to discriminate between a plethora of possible theoretical explanations. The determination of the late-ISW signal through the cross-correlation between the CMB and the projected distribution of galaxies measured by wide cosmological surveys constitutes a promising method of investigation.
In this thesis we have derived the ISW effect from a full treatment of the coupled Boltzmann and Einstein equations perturbed to the first order. Within this theoretical framework we have shown that the ISW is a source of secondary anisotropies in the CMB temperature, as it is generated after the recombination of hydrogen, and its contribution has to be integrated along the photon's path. Since the ISW signal arises when the gravitational potential evolves with time, it receives contributions during two distinct phases of the cosmic history: immediately after the recombination of Hydrogen, due to the residual effect of radiation before the full matter domination epoch, and when the dark energy starts to influence the dynamics of the Universe at late times.
This late-ISW effect is seen mainly in the lowest $\ell-$ values range of the CMB temperature power spectrum, due to the random superimposition of opposite contributions at small scales.
Its importance stems from the fact that this effect is sensitive to the particular model of dark energy considered. Detection of such a signal is, however, limited by the noise arising from other sources of CMB-anisotropies on large angular scales and from the cosmic variance. This problem can be overcome by cross-correlating deep galaxy surveys with the CMB, since galaxies are tracers of the large scale structure and their distribution can probe gravitational potentials.
The ISW effect is detected through correlations, at the current state, mostly with weak significance from single catalogues of galaxies. Some authors have managed to combine data from different cosmological surveys in order to enhance the signal-to-noise ratio. However using this procedure one has to face the non-trivial task of estimating the covariance between the different catalogues used. Upcoming surveys are expected to considerably improve the signal-to-noise ratio, thanks to the large sky fraction covered, to the high number of sources detected and to the large range of redshift probed. Thus, we are still far from a true tomographic analysis. For our analysis we considered two upcoming surveys, optimized for the ISW detection: Euclid and LSST.

Our forecast was oriented in the possibility to detect K-mouflage cosmological models. K-mouflage is a suggestive theory that supposes the existence of an additional scalar degree of freedom which induces a modification of gravity due to a non-minimal coupling with matter. We have derived the equation of motion for the background dynamics for K-mouflage cosmology. Studying the evolution of linear perturbations in K-mouflage, we were able to write the growth factor equation in K-mouflage, which differs from that of ΛCDM due to the presence of two additional factors. We have also examined the screening mechanism provided by the K-mouflage theory to reproduce General Relativity on scales where the gravitational force is sufficiently high.
To compute the ISW-galaxy cross-correlation power spectrum, which is the fundamental quantity in our analysis, we needed the growth factor in K-mouflage. This was computed for three different models through the numerical solution of a set of coupled differential equation. This allowed us to obtain also the background evolution for this three models. We verified that our results for the background evolution and for the growth factor of perturbations are in perfect agreement with the theoretical predictions. Moreover, we verified that our results for the background evolution in K-mouflage agree with those obtained in [14], nevertheless our results for the growth factor show a substantial discrepancy with respect to what obtained by the same author in [15]. After having performed different tests and directly contacted the author of [15] we can conclude that our result for the growth-factor represents the correct solution.
Using our solution for D in K-mouflage, we computed the ISW-galaxies cross-correlation power spectrum as expected to be measured from Euclid and LSST in several redshift bins. We have assumed appropriate parametrizations for the redshift distribution of sources, characteristic of each survey. The exact calculation of the cross-correlation power spectrum is computationally expensive, therefore we employed the Limber approximation which allowed to significantly reduce the computational complexity of the problem. However, as we verified, this approximation introduces large errors at low multipoles, where the exact computation in needed. To check our results we also computed the exact value of the cross-correlation power-spectrum for a representative sample of multipoles and than we implemented a cubic spline interpolation, in order to obtain the complete power spectrum without using approximations.
The cross-correlation power spectrum shows a peculiar behaviour in the case of Model 2 of K-mouflage. In fact for this model, the correlation between the ISW and the galaxy counts appears to be negative. This is explained by the fact that for this model the derivative with respect to the redshift of the gravitational potential changes sign at a given redshift, as we have verified. This anti-correlation can therefore represent a smoking-gun signature for this kind of model.
In conclusion we performed an error analysis, binning the multipole range in 7 ℓ-bins, we forecasted the error and the level of significance for the deviation between each K-mouflage model and ΛCDM using CMB-galaxy cross-correlation with Euclid and LSST data. We obtain that two out of three K-m models would be clearly distinguishable from ΛCDM, up to a level of $\sim 7\sigma$ with LSST and $\sim 6\sigma$ with Euclid.
We than expect the upcoming Euclid and LSST survey to be optimally suited for ISW detection and will be useful tools fro distinguish between different cosmological models.
We underline that our work represents a preliminary to a full Fisher-matrix

analysis. In the next future we expect to extend our forecast in order to know exactly at what level the cross-correlation should put constraints the parameters describing K-mouflage models.
An other possible development is to extend our analysis in order to include relativistic correction, that should arise on very large scales, of order the cosmological horizon, in K-mouflage models as well as in the ΛCDM model. This effects can safely be neglected on scales well under the cosmological horizon, but can significantly modify the ISW signal, that originates on large scales.
Finally we expect to extend our analysis to different models of modified gravity and dark energy, this can be done in a smart way by using the so called Effective Field Theory of dark energy, which is capable to parametrize very broad classes of models.

Bibliography

[1] Afshordi, N. 2004, Physical Review D, 70, 083536, arXiv:astro-ph/0401166

[2] Afshordi, N., Loh, Y.-S., & Strauss, M. A. 2004, Physical Review D, 69, 083524, arXiv:astro-ph/0308260

[3] Amendola, L., Appleby, S., Avgoustidis, A., et al. 2016, arXiv:1606.00180

[4] Amendola Luca and Tsujikawa Shinji, *Dark Energy: Theory and Observations*, 2010, Cambridge University Press

[5] Ascher Uri M. and Petzold Linda R., *Computer Methods for Ordinary Differential Equation and Differential-Algebraic Equations*, 1997

[6] Baumann Daniel, *Cosmology, Part III Mathematical Tripos*

[7] Barreira Alexandre, *Structure Formation in Modified Gravity Cosmologies*, 2016, Springer

[8] Barreira, A., Brax, P., Clesse, S., Li, B., & Valageas, P. 2015, Physical Review D, 91, 123522, arXiv:1504.01493

[9] Bertacca, D., & Bartolo, N. 2007, JCAP, 11, 026, arXiv:0707.4247

[10] Bertacca, D., Raccanelli, A., Piattella, O. F., et al. 2011, JCAP, 3, 039, arXiv:1102.0284

[11] Bartolo, N., Matarrese, S., & Riotto, A. 2007, arXiv:astro-ph/0703496

[12] Bianchini, F., Bielewicz, P., Lapi, A., et al. 2015, ApJ, 802, 64, arXiv:1410.4502v5

[13] Boucaud, A. 2013, Ph.D. Thesis https://tel.archives-ouvertes.fr/tel-00983440

[14] Brax, P., & Valageas, P. 2014, Physical Review D, 90, 023508, arXiv:1403.5420

[15] Brax, P., & Valageas, P. 2014, Physical Review D, 90, 023507 arXiv:1403.5424

[16] Brax, P., & Valageas, P. 2014, Physical Review D, 90, 123521, arXiv:1408.0969v2

[17] Brax, P., Rizzo, L. A., & Valageas, P. 2016, Physical Review D, 92, 043519, arXiv:1505.05671

[18] Brax, P., & Davis, A.-C. 2015, JCAP, 10, 042, arXiv:1506.01519

[19] Brax, P., & Valageas, P. 2016, JCAP, 1, 020, arXiv:1509.00611

[20] Cheng Ta-Pei, *Relativity, Gravitation and Cosmology: A Basic Introduction*, 2010, Oxford University Press

[21] Caldwell, R. R., Dave, R., & Steinhardt, P. J. 1998, Physical Review Letters, 80, 1582, arXiv:astro-ph/9708069

[22] Clifton, T., Ferreira, P. G., Padilla, A., & Skordis, C. 2012, Physics Reports, 513, 1, arXiv:1106.2476v3

[23] Cooray, A. 2002, Physical Review D, 65, 083518, arXiv:astro-ph/0109162

[24] Copeland, E. J., Sami, M., & Tsujikawa, S. 2006, International Journal of Modern Physics D, 15, 1753, arXiv:hep-th/0603057

[25] Corasaniti, P.-S., Giannantonio, T., & Melchiorri, A. 2005, Physical Review D, 71, 123521, arXiv:astro-ph/0504115

[26] Corasaniti, P. S., Bassett, B. A., Ungarelli, C., & Copeland, E. J. 2003, Physical Review Letters, 90, 091303, arXiv:astro-ph/0210209

[27] Corasaniti, P. S. 2004, Ph.D. Thesis, arXiv:astro-ph/0401517

[28] Coles Peter and Lucchin Francesco, *Cosmology: The Origin and Evolution of Cosmic Structure*, 2002, John Wiley Sons Inc Print on

[29] Crittenden, R., Boughn, S., & Turok, N. 1996, Bulletin of the American Astronomical Society, 28, 51.04, arXiv:astro-ph/9510072

[30] Croton, D. J. 2013, Publications of the Astronomical Society of Australia, 30, e052, arXiv:1308.4150

[31] de Putter Roland, *Probing Dark Energy with Theory and Observations*, 2010, Thesis

[32] de Putter, R., Doré, O., & Das, S. 2014, ApJ, 780, 185, arXiv:1306.0534

[33] Dodelson, S., *Modern Cosmology*, 2003, Academic Press

[34] Douspis, M., Castro, P. G., Caprini, C., & Aghanim, N. 2008, Astronomy and Astrophysics, 485, 395, arXiv:0802.0983

[35] Eisenstein, D. J., & Hu, W. 1998, ApJ, 496, 605, arXiv:astro-ph/9709112

[36] Ferraro, S., Sherwin, B. D., & Spergel, D. N. 2015, Physical Review D, 91, 083533, arXiv:1401.1193v1

[37] Garriga, J., Pogosian, L., & Vachaspati, T. 2004, Physical Review D, 69, 063511, arXiv:astro-ph/0311412

[38] Gaztañaga, E., Manera, M., & Multamäki, T. 2006, MNRAS, 365, 171, arXiv:astro-ph/0407022

[39] Giannantonio, T., Scranton, R., Crittenden, R. G., et al. 2008, Physical Review D, 77, 123520, arXiv:0801.4380

[40] Giannantonio, T., Porciani, C., Carron, J., Amara, A., & Pillepich, A. 2012, MNRAS, 422, 2854, arXiv:1109.0958v3

[41] Giannantonio, T., Crittenden, R. G., Nichol, R. C., et al. 2006, Physical Review D, 74, 063520, arXiv:1209.2125

[42] Giannantonio, T., Fosalba, P., Cawthon, R., et al. 2016, MNRAS, 456, 3213, arXiv:1507.05551v2

[43] Giannantonio, T., Crittenden, R., Nichol, R., & Ross, A. J. 2012, MNRAS, 426, 2581

[44] Hairer, E., Norsett, S.P., & Wanner, G., Solving Ordinary Differential Equations i. Nonstiff Problems. 2nd edition. Springer Series in Computational Mathematics, 1993, Springer-Verlag

[45] Ho, S., Hirata, C., Padmanabhan, N., Seljak, U., & Bahcall, N. 2008, Physical Review D, 78, 043519, arXiv:0801.0642

[46] Hu, W. PhD thesis *Wandering in the background: A Cosmic microwave background explorer* 1995, arXiv:astro-ph/9508126v2

[47] Hu, W., & Dodelson, S. 2002, Annual Review of Astronomy and Astrophysics, 40, 171, arXiv:astro-ph/0110414

[48] Hu, W., & Scranton, R. 2004, Physical Review D, 70, 123002, arXiv:astro-ph/0408456

[49] Hu, W., & Sugiyama, N. 1994, Physical Review D, 50, 627, arXiv:astro-ph/9310046

[50] Hu, W., & Sugiyama, N. 1996, ApJ, 471, 542, arXiv:astro-ph/9510117

[51] Hubble, E., Proc.Nat.Ac.Sci. 15, (1929)

[52] Ilić, S. 2014, Journal of Physics Conference Series, 484, 012034, arXiv:1205.2537

[53] Ivezic, Z., Tyson, J. A., Abel, B., et al. 2008, arXiv:0805.2366

[54] Joyce, A., Jain, B., Khoury, J., & Trodden, M. 2015, Physics Reports, 568, 1, arXiv:1407.0059v2

[55] Khosravi, S., Mollazadeh, A., & Baghram, S. 2016, JCAP, 9, 003, arXiv:1510.01720

[56] Koyama, K. 2016, Reports on Progress in Physics, 79, 046902, arXiv:1504.04623v2

[57] Lahav, O., & Liddle, A. R 2014, arXiv:1401.1389

[58] Laureijs, R., Amiaux, J., Arduini, S., et al. 2011, arXiv:1110.3193

[59] Liddle Andrew R. and Lyth David H., *The Primordial Density Perturbation*, 2010, Cambridge University Press

[60] Loverde, M., Hui, L., & Gaztañaga, E. 2007, Physical Review D, 75, 043519, arXiv:astro-ph/0611539

[61] Loverde, M., & Afshordi, N. 2008, Physical Review D, 78, 123506, arXiv:0809.5112

[62] LSST Science Collaboration, Abell, P. A., Allison, J., et al. 2009, arXiv:0912.0201

[63] Mainini, R., & Mota, D. F. 2012, ApJ, 744, 3, arXiv:1011.0083

[64] Montanari, F., & Durrer, R. 2015, JCAP, 10, 070, arXiv:1506.01369v3

[65] Mukhanov Viatcheslav, *Physical Foundations of Cosmology*, 2005, Cambridge University Press

[66] Nolta, M. R., Wright, E. L., Page, L., et al. 2004, ApJ, 608, 10, arXiv:astro-ph/0305097

[67] Ofer Lahav and Yasushi Suto, *Measuring our Universe from Galaxy Redshift Surveys*,Living Rev. Relativity 7, (2004), 8. URL (accessed <date>):http://www.livingreviews.org/lrr-2004-8

[68] Planck Collaboration, Ade, P. A. R., Aghanim, N., et al. 2015, arXiv:1502.01589

[69] Planck Collaboration, Ade, P. A. R., Aghanim, N., et al. 2014, Astronomy Astrophysics, 571, A16, arXiv:1303.5076

[70] Pogosian, L. 2005, JCAP, 4, 015, arXiv:astro-ph/0409059

[71] Pogosian, L., Corasaniti, P. S., Stephan-Otto, C., Crittenden, R., & Nichol, R. 2005, Physical Review D, 72, 103519, arXiv:astro-ph/0506396

[72] Raccanelli, A., Bonaldi, A., Negrello, M., et al. 2008, MNRAS, 386, 2161, arXiv:0802.0084

[73] Réfrégier Alexandre and Adam Amara, Thomas Kitching, Anais Rassat, Roberto Scaramella, Jochen Weller, *Euclid Imaging Consortium, Imaging the dark Universe with Euclid*, 2010, Euclid Imaging Consortium arXiv:1001.0061v1

[74] Renk, J., Zumalacárregui, M., & Montanari, F. 2016, JCAP, 7, 040, arXiv:1604.03487v2

[75] Sachs, R. K., & Wolfe, A. M. 1967, ApJ, 147, 73

[76] Santos, M., Alonso, D., Bull, P., Silva, M. B., & Yahya, S. 2015, Advancing Astrophysics with the Square Kilometre Array (AASKA14), 21, arXiv:1501.03990

[77] Sawangwit, U., Shanks, T., Cannon, R. D., et al. 2010, MNRAS, 402, 2228, arXiv:0911.1352

[78] Schmidt, F., Liguori, M., & Dodelson, S. 2007, Physical Review D, 76, 083518, arXiv:0706.1775

[79] Schneider Peter, *Extragalactic Astronomy and Cosmology: An Introduction*, 2010, Springer

[80] Shoji, M., & Komatsu, E. 2010, Physical Review D, 82, 089901, arXiv:1003.0942

[81] Tsujikawa, S. 2010, Lecture Notes in Physics, Berlin Springer Verlag, 800, 99, arXiv:1101.0191

[82] White, M., & Hu, W. 1997, Astronomy and Astrophysics, 321, 8, arXiv:astro-ph/9609105

[83] White Martin on behalf of Planck collaboration, *Cosmological Results from Planck 2015*

[84] Wikipedia the free encyclopedia., *Bessel function*, https://en.wikipedia.org

[85] Xin, B., Claver, C., Liang, M., et al. 2015, Applied Optics, 54, 9045, arXiv:1506.04839

Ringraziamenti

Un sentito ringraziamento a Michele e Nicola per l'impeccabile guida scientifica, la grande disponibilità e, soprattutto, per avermi trasmesso l'interesse e la curiosità senza le quali non avrei potuto affrontare e portare a compimento questo lavoro di tesi.
Ringrazio la mia famiglia per l'appoggio incondizionato durante questi anni all'università e per avermi sostenuto in tutte le mie scelte.
Ringrazio gli amici e i compagni di Astronomia, per essere stati sempre al mio fianco sia per confronti e suggerimenti che durante le pause, le serate, i momenti di svago e goliardia.
Infine un ringraziamento particolare va alla mia Arianna, per essere stata un'indispensabile fonte di aiuto, utili consigli e interessanti confronti per questo lavoro, per avermi motivato, divertito e per avermi dedicato tanto affetto e attenzione.